Nadia Mattiucci

Università degli Studi di Roma “RomaTre”

Tesi di Dottorato

“Linear and Nonlinear Effects in One-Dimensional Photonic Crystals and Negative Index Materials.”

Tutore Interno	Tutore Esterno
Prof. Massimo Santarsiero	Dr. Michael Scalora

A Claudia e Giuseppe

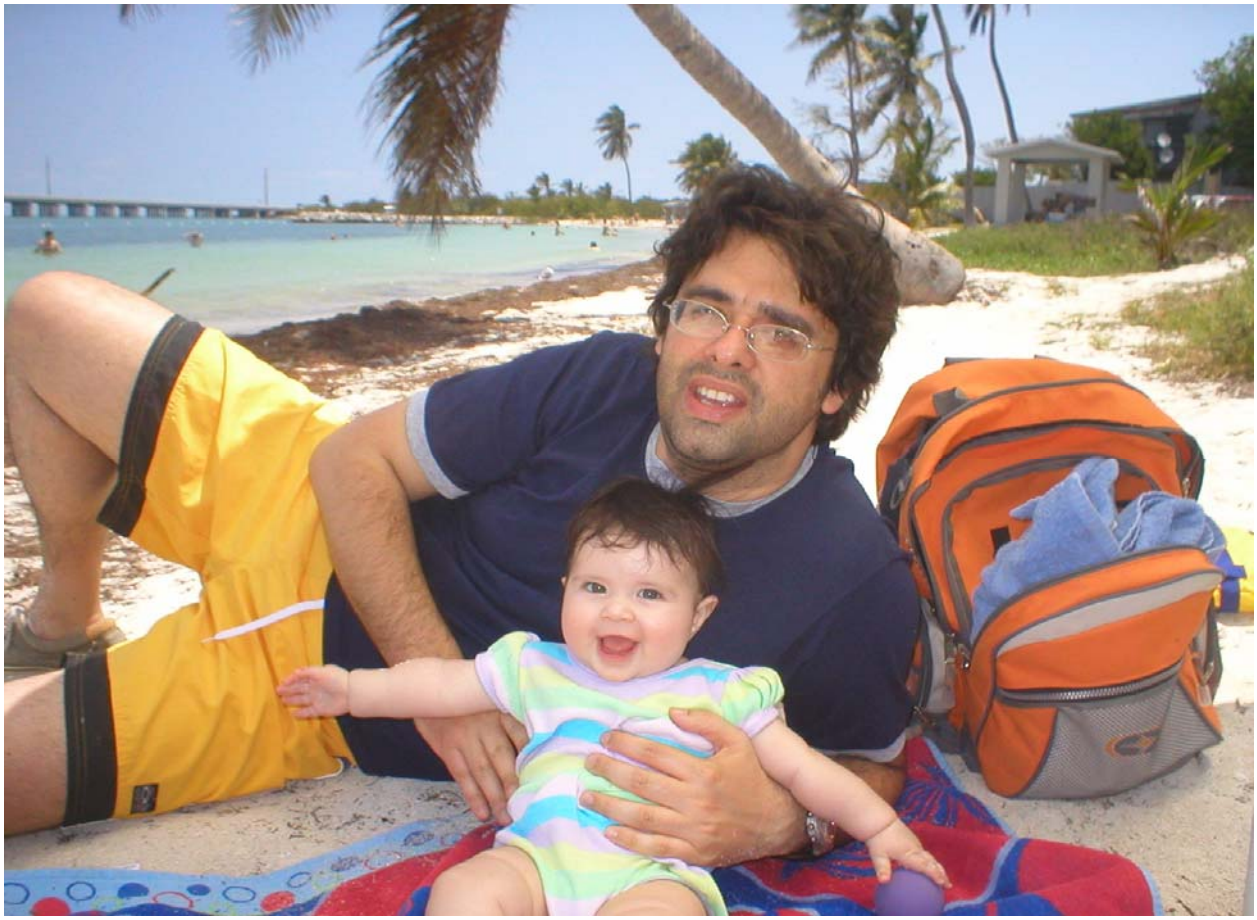

Index

Part II: "Negative index materials."

Introduction

Electromagnetic waves interact with atoms and molecules that compose naturally occurring materials. Materials can therefore be used to guide or manipulate electromagnetic waves–in the same way that a glass lens can focus light, for example. But the available electromagnetic response from naturally occurring materials is limited. Artificial constructed meta-materials, however, are not subject to the same limitations as real materials, and can be used to extend material response. For example, a metal film with arrays of small holes in it could be transparent to light; an array of nonmagnetic conductive elements could exhibit a strong, resonant magnetic response and materials that exhibit negative refraction could thus be engineered, beyond any intuitive expectations.

The notion of meta-materials originated in the microwave community but has been widely adopted in the domain of optical research, thanks to rapidly improving nanofabrication capabilities and the development of sub-wavelength scanning imaging techniques. In a meta-material, the properties largely derive from the structure rather than from the material itself. The structural units can be tailored in shape and size; their composition and morphology can be artificially tuned, and inclusions (defects) can be designed and placed at desired locations to achieve new functionality.

Among the wide class of meta-materials we will focus on two sub-classes: photonic crystals (PCs), in particular one-dimensional PCs, and negative index materials (NIMs). In a PC the dimension of the unit cell is of the order of the fraction of the incident wave-length, while in a NIM the dimension of the unit cell is much more smaller that the dimension of the incident wavelength. In the first case the exceptional properties arise due to scattering effects. In the second case they arise from bulk properties: the electric permittivity ε and the magnetic permeability μ of the engineered material that induce a negative refractive index at certain frequencies. From the electromagnetic point of view, the wavelength, L, determines whether a collection of atoms or other objects can be considered a material. Any collection of objects whose size and spacing are much smaller than L can be described by the electromagnetic parameters ε and μ. Although such an inhomogeneous collection may not satisfy our intuitive definition of a material, an electromagnetic wave passing through the structure cannot tell the difference. The most commonly known property of PCs is their ability to change the transmission properties of their constituent materials. With a PC it is possible to open

transmission peaks (T=1) at a desired frequencies, and whole regions (gaps) where the propagation of light is forbidden. That is why PCs are also known as photonic band gap structures. The most commonly known properties of negative index materials is perhaps their ability to refract light in the opposite direction with respect to naturally occurring materials, so that the k vector inside the structure points in the opposite direction with respect to a natural material, and the three vectors $\vec{E}$, $\vec{B}$ and $\vec{k}$ form a left-handed tern. That is why NIMs are also known as left handed materials.

This Thesis is organized in two sections: the first section is devoted to the study of linear and nonlinear properties of 1-D PCs, while the second section is devoted to the study of linear and nonlinear properties of NIM. As we will see in section two some of the properties of 1-D PCs can be found also in NIM.

Part I:

“Linear and non-linear effects in one-dimensional photonic crystals.”

“If only it were possible to make dielectric materials in which electromagnetic waves cannot propagate at certain frequencies, all kinds of almost-magical things would be possible.”

-John Maddox

Nature **348**, 481 (1990)

I-1 Introduction

I-1.1 Overview

Structures in which scattering or diffracting elements are arranged in such a way that their mutual distances are comparable with the wavelength of the incident wave are often referred to as photonic crystals (PCs), or photonic band gap structures, PBGs in short. Typically, photonic crystals are periodic or quasi-periodic arrays in one, two or three dimensions (see Fig I-1. 1), but more sophisticated geometries, like defect, fractal and chirped structures (to name a few), have

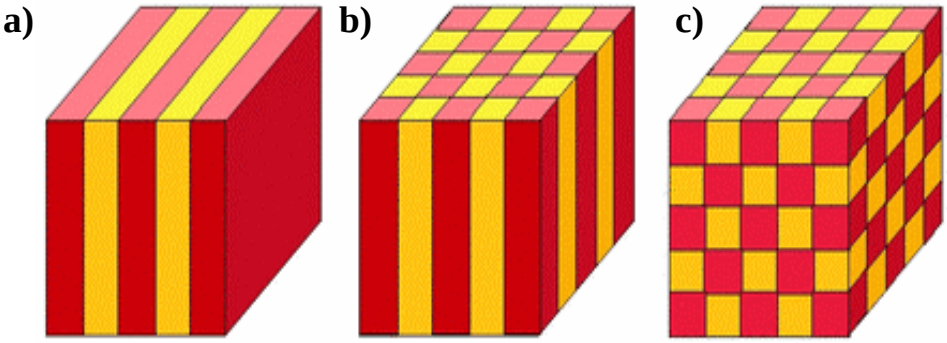

Fig. I-1. 1: Simple examples of photonic bandgap structures: a)Structure periodic in one direction, b) structure periodic in two directions, c) structure periodic in three directions.

been exploited as well. PBGs are able to selectively transmit or reflect light at various wavelengths, as they affect the properties of the light in almost the same way that semiconductor crystals affect the properties of electrons. A periodic arrangement of different dielectric materials results in allowed and forbidden frequency bands and gaps for the incident light, in analogy to energy bands and gaps of semiconductors [1]. PBGs are artificial structures, but wonderful examples of them can also be found in nature. For example, the surface of the wings of a butterfly is a periodic dielectric structure, and the colors are the result of a selective reflection of the spectral components of sunlight (see Fig. I-1. 2) [2]. Because a crystal array looks slightly

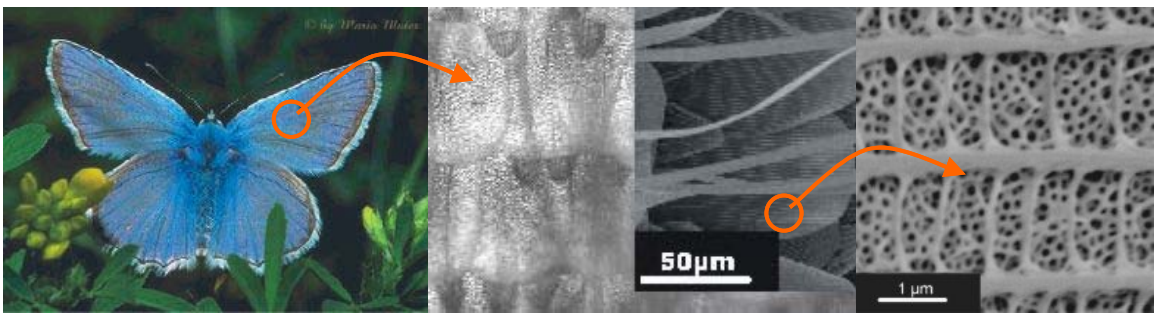

Fig. I-1. 2: Butterfly wing structure in different magnifications. Photo taken from Ref.[2]

different from different angles, (unlike pigments, which are the same from any angle) photonic crystals can lead to shifting shades of iridescent color.

The name “photonic crystal” and the exciting growth of photonic crystal research began with the works of Eli Yablonovitch [3] and Sajev John [4], in the late 1980s. They began with basic concepts and experiments in the microwave regime, where 3D structures could easily be fabricated (see Fig.I-1.3). At the present time, fabrication techniques allow spatial resolutions in the sub-micron regime, resulting in an explosion of new photonic bandgap structures in the

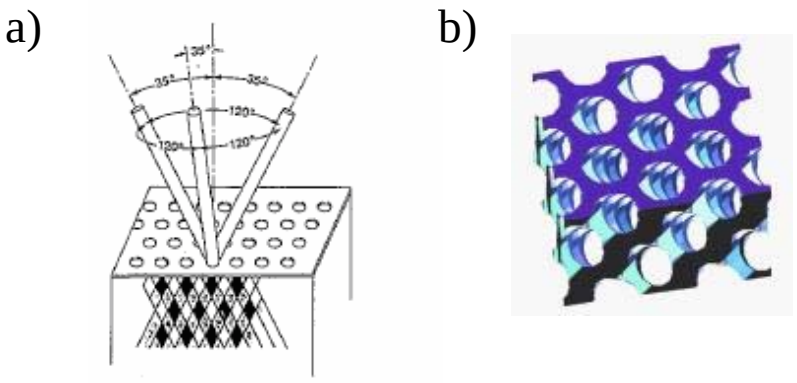

Fig. I-1. 3: First PBG material: yablonovite after Eli Yablonovitch. **a)**The method of constructing the yablonovite (FCC lattice): a slab of material is covered by a mask consisting of a triangular array of holes Each hole is drilled through three times, at an angle 35.26^0 away from normal, and spread out 120^0 on the azimuth. **b)**Three dimensional image of the yablonovite. Picture from Ref [3]

infrared and visible regime. Photonic crystals can be engineered in order to control the optical response of the materials. They can be designed in order to allow the propagation of light only in certain directions and for certain frequencies, to localize light in specific areas, to slow down its velocity at certain frequencies, to artificially introduce dispersion (geometrical dispersion).

A new research direction results from the growth, intersection and overlap of research in the fields of nonlinear optics and photonic crystals. Intense laser sources and confinement of light to small spatial regions in photonic crystals allows us to generate optical fields that make significant nonlinear changes in the dielectric constant. Since the slowing down depends strongly on the light wavelength, different colors propagate with much different velocities, i.e. there is strong dispersion at the photon band edge, near the photonic bandgap. This dispersion can be used in order to compensate the normal dispersion of the material and achieve phase matching condition for nonlinear phenomena. The new physical phenomena being discovered in linear and

nonlinear photonic crystals will lead to advances in optical devices and applications in optical systems. Examples of optical devices include pulse shaping, pulse compression, and pulse regeneration. Nonlinear photonic crystals may allow for significant advances in optical buffering devices by using resonantly stored light in dielectric array defects. All-optical switches based on nonlinear photonic crystal are now being explored for low-power, low-cost alternatives to the

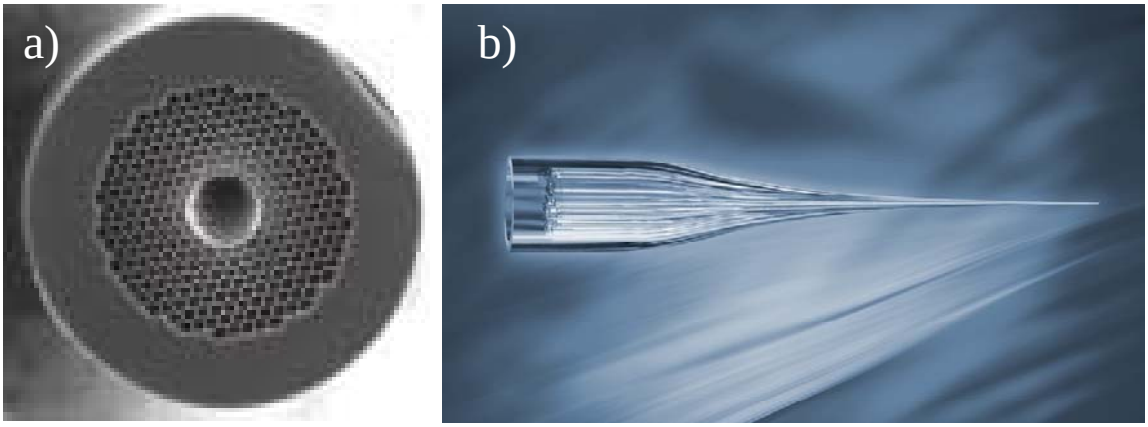

Fig. I-1. 4: Photonic Crystal fiber (PCF). a) A cross section of a PCF reveals microstructuring with air holes that run parallel to the fiber axis. b) A standard technique to construct PCFs consisting in arrange common fibers in the desired geometry and then they are stretched altogether. The PCF is able to guide in the air core due two the presence of a 2-D photonic crystal structure in the form of "honeycomb" lattice

optical-electronic-optical techniques. Optical parametric amplification enhanced by dielectric arrays is another important possible application. The reader interested in more details about those and other nonlinear optical applications of photonic crystals may consult the book "Nonlinear Photonic Crystals" cited in our Ref. [5]. Other applications that have been proposed over the

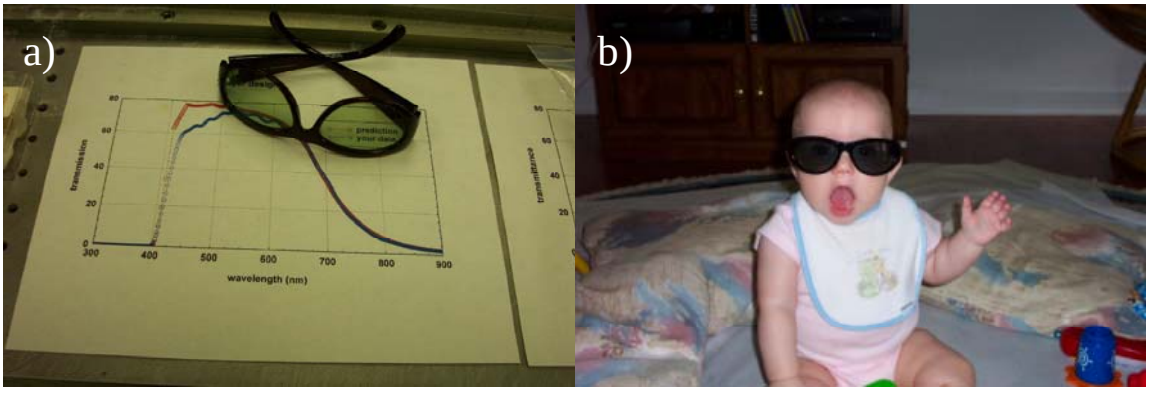

Fig. I-1. 5: Glasses made of a one-dimensional metal-dielectric photonic crystal (transparent metal). a) glasses and the transmission curve of the lenses. b)glasses.

years include photonic crystals fibers [6] (see Fig.I-1.4), photonic crystals circuits [7],

transparent metal-dielectric stacks (see Fig.I-1.5) [8], highly efficient micron-sized devices for nonlinear frequency conversion [9].

I-1.2 Finite, One-Dimensional, Photonic Crystals

One-dimensional photonic crystals, also known as one dimensional photonic band gap structures (1-PBGs), Bragg gratings, or simply multilayered structures, represent the simplest example of a photonic band gap structure. Despite their simplicity, they retain many of the characteristics that can be found in more complicated multidimensional structures. 1-D PBGs are made of alternating layers of dielectric materials, or alternating layers of metallic and dielectric materials. The basics properties of those structures can be found in many textbook, and we cite

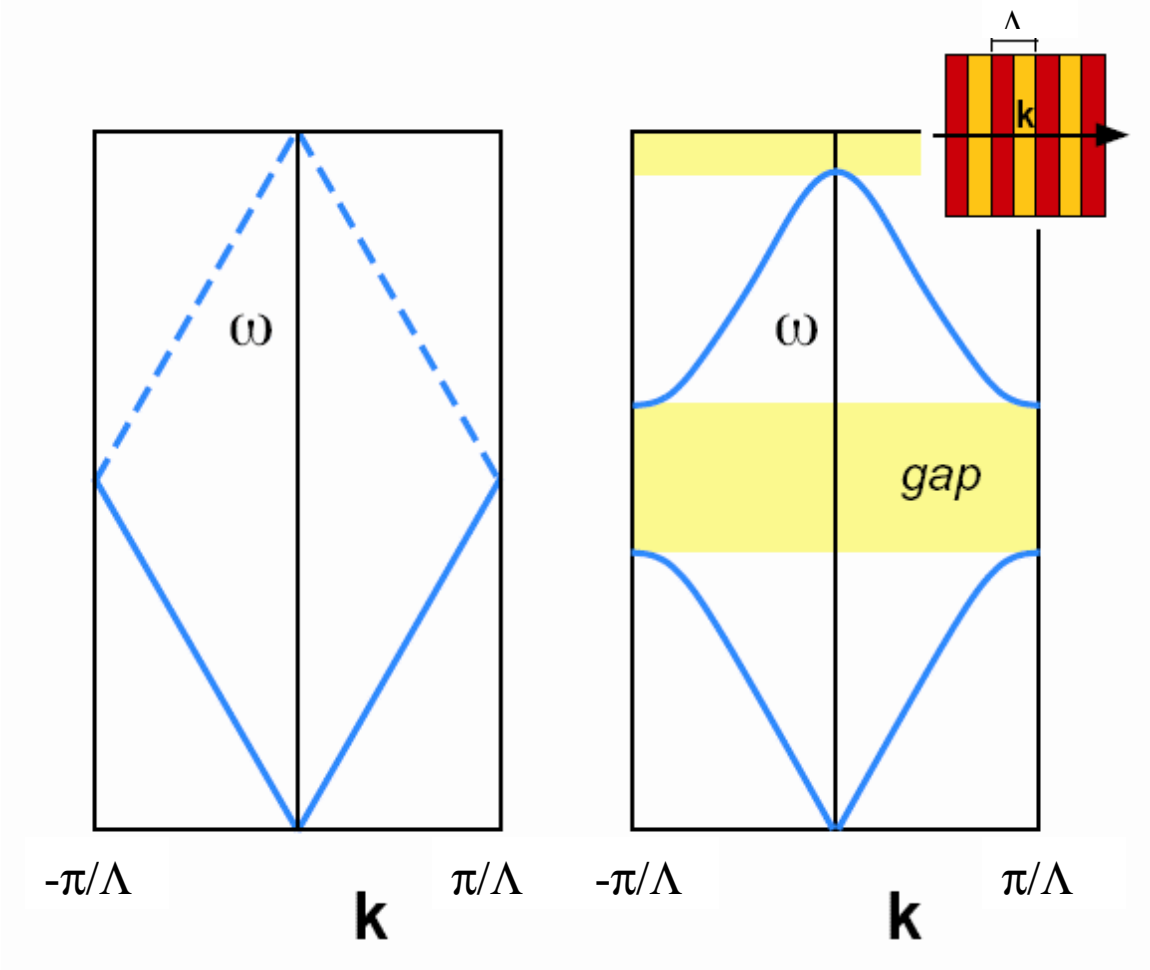

Fig. I-1. 6: How the energy band diagram changes with the introduction of 1D periodic dielectric constant variation.

for example the book by P. Yeh “Optical waves in layered media”[10]. Here we give just a brief overview of their most salient properties.

A first analysis when a space periodicity is present can be made using the same approach used in solid state physics, i.e. the Bloch theory [10]. In Fig. (I-1. 6) we show how the periodicity changes the energy band diagram by opening forbidden bands. It is worth noting that, unlike crystal lattices studied in solid state physics, 1-D PBGs are structures inherently *finite* in size, at

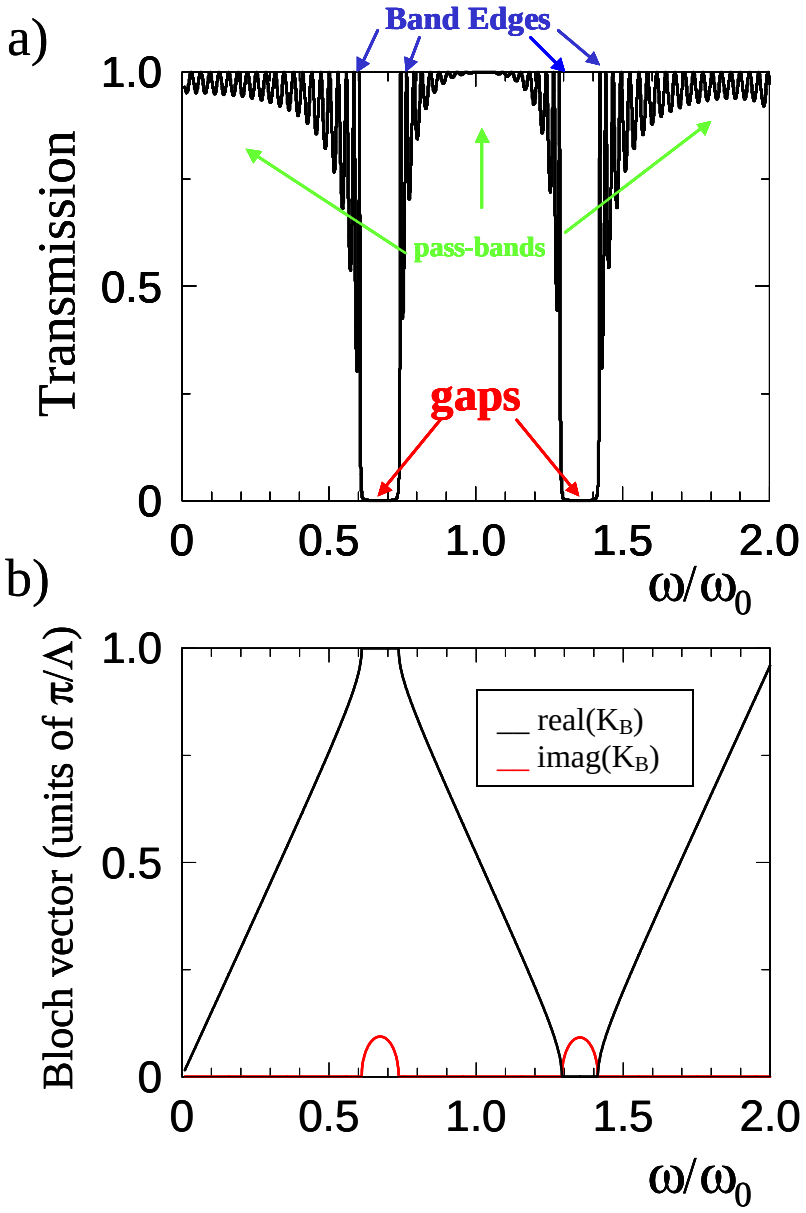

Fig. I-1. 7: a)Transmission spectrum of a 20-Periods, quarter/half-Wave Stack: λ/4-λ/2. The refractive indexes are respectively 1 and 1.4. b) Bloch vector, real part (black line) and imaginary part (red line) vs. ω/ω_0. ω_0 is a reference wavelength and Λ is the length of the elementary cell.

most 30-40 periods, for total lengths never exceeding 40-50μm. For all intents and purposes, these structures do not admit translational invariance and therefore the Bloch theory is no longer exhaustive, although it still remain a useful tools. In Fig I-1. 7a we show the typical transmission response of a multilayered structure. The transmission is characterized by pass bands where most of field is transmitted through the structure, and bang gaps with high reflectivity, as shown in the figure. In Fig I-1. 7b we show the Bloch vector (K_B) as a function of the frequency for the same elementary cell of the finite structure described in Fig. I-1. 7a. We note that the band gaps coincide with the forbidden bands of the Bloch theory for the corresponding infinite structure [10].

The transmission resonances near the band edges of the structure are of particular interest because a field tuned at those points reaches high values of local intensity, making possible the enhancement of nonlinear optical phenomena [9]. In Figs. I-1. 8 we show the typical localization properties of an electromagnetic field inside a 1-D PBG with its frequency tuned respectively in

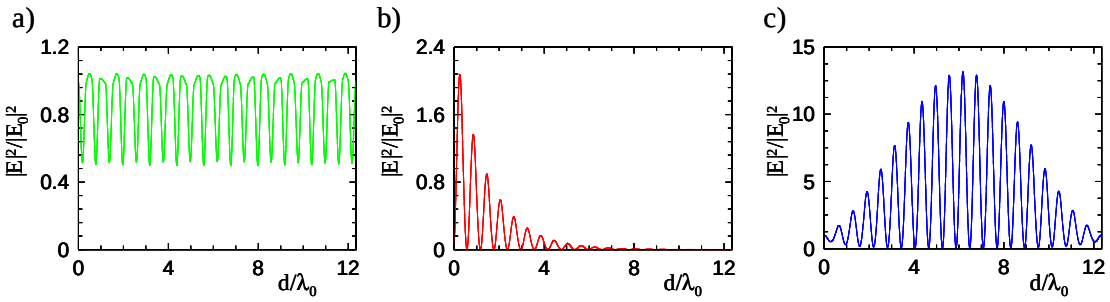

Fig. I-1. 8: Electric field distribution inside the structure defined in Fig. I-1. 7a for different tuning conditions. a) frequency tuned in the pass band, b) frequency tuned inside the gap, c) frequency tuned at the band edge transmission resonance. $\lambda_0=2\pi c/\omega_0$ is a reference wavelength.

the pass band(Fig I-1. 8a), in the band gap (Fig I-1. 8 b) and at the band edge (Fig I-1. 8 c). The fact that the structures we study are inherently finite in size leads to several important consequences. Looking again at the field localization described in Fig.(I-1. 8), we can see that even the band gaps are not strictly “forbidden” because a portion of incident field is able to penetrate the structure in the form of an evanescent wave, and therefore to “tunnel” through it. Moreover, the field localization properties at the band edges find their origin in the finiteness of the structure, i.e. in the coupling with the external modes. In other words, the fact the structure is finite prevents us from applying periodic boundary conditions, and therefore our electromagnetic

problem becomes non-hermitian. The consequences of this fact are that well established concepts such as group velocity, energy velocity, and density of modes need in our case a complete and profound reevaluation, as we will see in more details in the next chapter.

References

[1] J.D. Joannopoulos, R.D. Meade, J.N. Winn, “Photonic Crystals: Molding the Flow Light”, Princeton University Press, Princeton (1995)

[2] G. I. Márk, K. Kertész, Zs. Bálint, Z. Vértesy, Z. E. Horváth, J. Balázs, D. Méhn, I. Kiricsi, V. Lousse, J. -P. Vigneron, L. P. Biró, Phys. Rev. E **67**, 021907 (2003). and www.mfa.kfki.hu/int/nano/online/2002_butterfly

[3] E. Yablonovitch, *Phys. Rev. Lett.* **58**, 2059-2062 (1987) ; J. Phys.: Condens. Matter **5**, 2443-2460 (1993)

[4] S. John, *Phys. Rev. Lett.* **58**, 2486-2489 (1987)

[5] Richard Slusher and Benjamin Eggleton Eds., “Nonlinear Photonic Crystals”, Springer Series in Photonics, Vol. **10** (Springer, Berlin, 2003) and references therein

[6] J.C. Knight, T.A. Birks, P.St.J. Russel, D.M. Atkin , *Opt. Lett*. **21,** 1547-1549 (1996)

[7] J.D. Joannopoulos, P.R. Villeneuve, S.H. Fan, *Nature* **386**, 143-149 (1997)

[8] M.J. Bloemer and M. Scalora, *Appl. Phys. Lett.* **72**, 1676-1678 (1998)

[9] M. Scalora, M.J. Bloemer, C. M. Bowden, G. D'Aguanno, M. Centini, C. Sibilia, M. Bertolotti, Y.Dumeige, I. Sagnes, P.Vidakovic, A. Levenson, *Opt. & Photon. News* **12**, 36-40 (2001).

[10] Pochi Yeh, “Optical waves in layered media”, John Wiley & Sons, New York, 1988.

I-2 Green function, density of modes and tunneling times.

I-2.0 Introduction

Although the number of experimental and theoretical reports on 1-D PCs is already quite large, in our view the issue of the density of modes (DOM) –or density of states (DOS)- regarding what one means by it, and its true and otherwise implied connections to other physical or measurable quantities, such as emitted energy and group velocity to name just two, is still far from being considered closed. There are at least three different ways to calculate the DOM that are currently used in the literature. The first way consists of calculating the local density of modes (LDOM) as follows: $\rho_\omega(z) = (-2k_0/c)\mathrm{Im}[G_\omega(z,z)]$, where $G_\omega(z,z)$ is the electromagnetic Green function of a source located at ξ=z inside a 1-D structure, and which oscillates with a harmonic time dependence of the type exp(-iωt) [11-13]; c is the speed of light in vacuum, and $k_0=\omega/c$ is the vacuum wavevector. The DOM is then defined as the weighted average of the LDOM over the length L of the PC, i.e., $\rho_\omega^\varepsilon = (-2k_0/cL)\int_0^L \varepsilon_\omega^R(z)\mathrm{Im}[G_\omega(z,z)]dz$ [13], where $\varepsilon_\omega^R(z)$ is the spatially dependent, linear, real, relative dielectric function of the PC and plays the role of the weight function. The second way consists of calculating the LDOM (DOM) as the spatially averaged electromagnetic energy density stored inside the crystal. This approach has been discussed at length in Ref.[8], and we will return to it later. The third approach was first proposed in Ref.[14], where the DOM was defined as: $\rho_\omega^\varphi = (1/L)(d\varphi_t/d\omega)$, where $\phi_t(\omega)$ is the phase of the transmission function $\tilde{t}_\omega = |\tilde{t}_\omega|\exp[i\varphi_t(\omega)]$. In the literature $\tau_\omega^\varphi = (d\varphi_t/d\omega) = \rho_\omega^\varphi L$ is often referred to as the phase time [15-17], "group delay", and "Wigner time" [18], and it gives the time that the transmitted part of an incident, quasi-monochromatic, un-chirped pulse takes to traverse a 1-D barrier [19-20]. We will refer to the DOM calculated this way as the "DOM calculated via the Wigner time".

We exploit connection and differences between the approaches outlined above in order to give the DOM a firmer theoretical footing when it comes to 1-D crystals. We will show that the DOM can be directly linked to the energy emitted from the structure, which is clearly a measurable quantity, and we will clarify the links that have previously been established between the concept of DOM and the tunneling times of quasi-monochromatic incident pulses.

I-2.1 The DOM calculated through the Green's function: The true DOM.

Let us suppose that a dipole sheet, of surface S and harmonically oscillating dipole moment: $\vec{p}(t) = (1/2)[\vec{p}_0 \exp(-i\omega t) + c.c.]$ oriented along $\hat{x}$, is located in the plane $z=\xi$, and it is positioned parallel to the surfaces A of a PBG of length L. This situation is sketched in Fig. (I-2. 1), where the structure is shown to occupy the space between z=0 and z=L. Due to its planar symmetry, the problem reduces to a 1-D one. As a consequence, the electric field

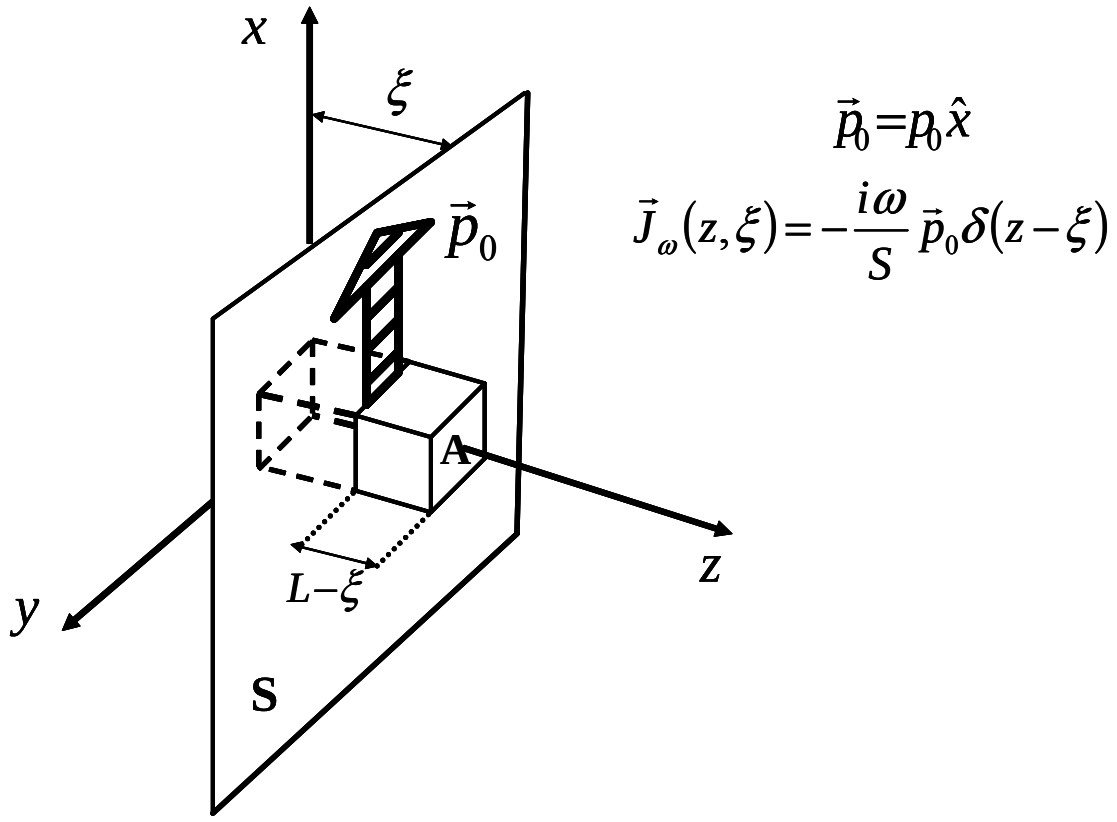

Fig. I-2. 1: Schematic representation of a dipole sheet of surface S and dipole moment $\vec{p}(t) = \vec{p}_0 \exp[-i\omega t]$ located along the plane $z=\xi$ and parallel to the surfaces A of a 1-D PC of length L located between $z=0$ and $z=L$.

$\vec{E}_\omega(z,\xi) = E_\omega(z,\xi)\hat{x}$ generated in the PC by the current density $\vec{J}_\omega(z,\xi) = J_\omega(z,\xi)\hat{x}$ that oscillates along the plane S can be calculated through the scalar Helmholtz equation as:

$$\frac{\partial^2 E_\omega(z,\xi)}{\partial z^2} + \frac{\omega^2 \varepsilon_\omega(z) E_\omega(z,\xi)}{c^2} = -\mu_0 \omega^2 \frac{p_0}{S}\delta(z-\xi), \qquad \text{(I-2. 1)}$$

where $\varepsilon_\omega(z)=1+\chi_\omega(z)=\varepsilon_\omega^R(z)+i\varepsilon_\omega^I(z)$ is the spatially dependent, complex dielectric function, $\chi_\omega(z)$ is the linear complex susceptibility of the medium, and δ(z-ξ) is the Dirac delta function. We seek solutions of Eq.(I-2. 1) that satisfy boundary conditions of outgoing waves, i.e., the radiated energy from the dipole sheet leaves the structure never to return, and no energy is incident from outside, namely:

$$E_\omega(z,\xi)=-\omega^2\mu_0\frac{p_0}{S}G_\omega(z,\xi)\,, \qquad \text{(I-2. 2)}$$

where $G_\omega(z,\xi)$ is the scalar Green's function that satisfies the following equation:

$$\frac{\partial^2 G_\omega(z,\xi)}{\partial z^2}+\frac{\omega^2\varepsilon_\omega(z)G_\omega(z,\xi)}{c^2}=\delta(z-\xi), \qquad \text{(I-2. 3)}$$

The way to construct the Green function for planar dielectric structures using the light-modes has been discussed at length in Refs.[21-23]. In 1-D, the Green function has the following form (see Appendix A):

$$G_\omega(z,\xi)=\begin{cases}\dfrac{\Phi_\omega^{(+)}(z)\Phi_\omega^{(-)}(\xi)}{2ik_0\tilde{t}_\omega} & L\ge z\ge\xi \\ \dfrac{\Phi_\omega^{(+)}(\xi)\Phi_\omega^{(-)}(z)}{2ik_0\tilde{t}_\omega} & 0\le z\le\xi\end{cases}, \qquad \text{(I-2. 4)}$$

where $\{\Phi_\omega^{(\pm)}\}$ are the left-to-right (LTR) and right-to-left (RTL) light-modes, $\tilde{t}_\omega=n_{0,1}t^{(-)}=n_{0,2}t^{(+)}$ is the transmission function, $n_{0,1\text{-}2}$ are the refractive indices of the materials surrounding the structure, $t_\omega^{(\pm)}$ are the LTR and RTL transmission functions (see Fig. (I-2. 2)), $k_0=\omega/c$ is the vacuum wavevector. LTR and RTL modes can be calculated using a standard linear matrix transfer technique, assuming a unitary electric field is incident on the structure from LTR for the $\Phi_\omega^{(+)}$ mode, and from RTL for the $\Phi_\omega^{(-)}$ mode, as shown in Fig. (I-2. 2), and as first reported in ref. [24]. For clarity, we report the details of the calculations that lead to Eq.(I-2. 4) in Appendix A [25]. Note that Eq.(I-2. 4) is valid for an arbitrary 1-D, finite structure, one that may also include material absorption and dispersion. Now, using Eq.(I-2. 2) and the expression for the current density, it can be shown that the mean electromagnetic power emitted by the dipole sheet embedded within the PC is given by:

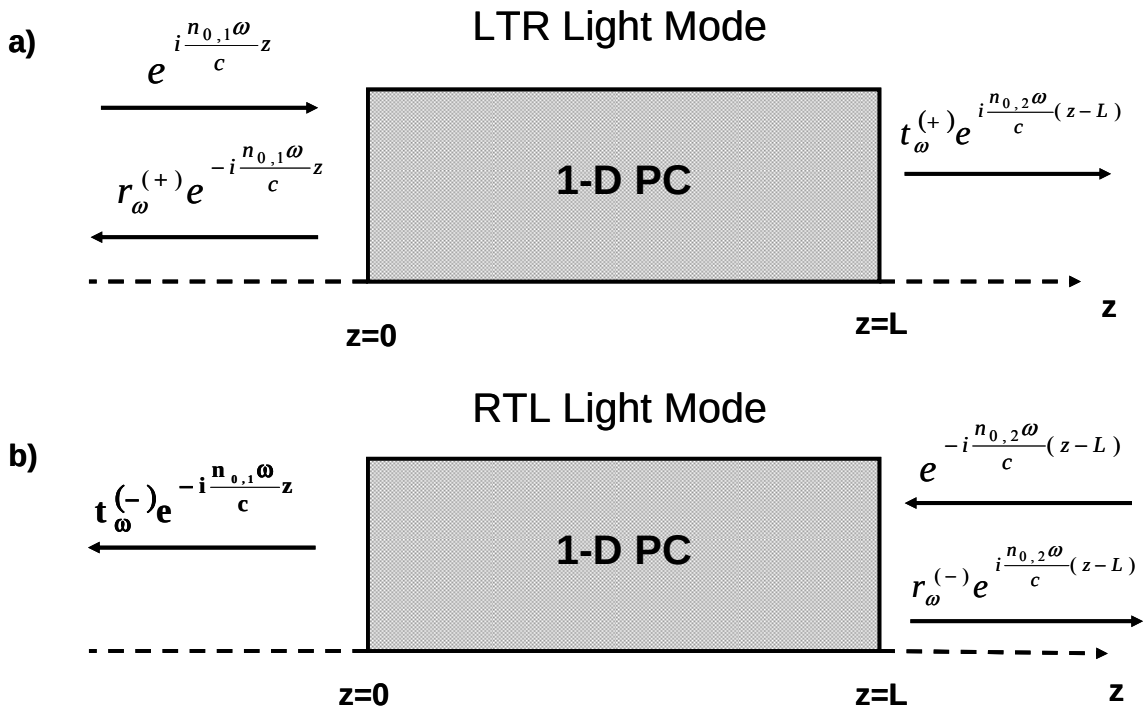

Fig. I-2. 2: Schematic representation of the boundary conditions imposed on: (a) LTR and (b) RTL light-modes. $r_\omega^{(\pm)}$ are the LTR and the RTL reflection coefficients, respectively, and $t_\omega^{(\pm)}$ are the corresponding transmission coefficients. $n_{0,1}$ and $n_{0,2}$ are the refractive indexes of the materials surrounding the PC. Note that $n_{0,2}t_\omega^{(+)} = n_{0,1}t_\omega^{(-)}$ as a consequence of time reversal symmetry.

$$\overline{W}^{(1D)}_{emitted\ in\ PC} \equiv -\frac{1}{2}\mathrm{Re}\int_V \vec{J}_\omega \cdot \vec{E}^*_\omega dV = -\frac{\omega^3\mu_0|p_0|^2 A}{2S^2}\mathrm{Im}[G_\omega(\xi,\xi)]. \qquad \text{(I-2. 5)}$$

Eq.(I-2. 5) tells us that the mean electromagnetic power emitted by a dipole sheet located at $z=\xi$ is proportional to the imaginary part of the scalar Green function calculated at $z=\xi$. We use the superscript "1D" to remark the fact that our approach is specific for electromagnetic problems that have planar symmetry, and can therefore be reduced to 1-D problems. The mean electromagnetic power emitted by the same dipole sheet located in free space in the same volume $V=AL$ occupied by the PC is:

$$\overline{W}^{(1D)}_{emitted\ in V,\ free\ space} = \frac{\omega^3\mu_0|p_0|^2 A}{4S^2k_0}. \qquad \text{(I-2. 6)}$$

From Eq.(I-2. 5) and Eq.(I-2. 6) we find :

$$\frac{\overline{W}^{(1D)}_{emitted\ in\ PC}(\xi)}{\overline{W}^{(1D)}_{emitted\ in\ V,\ free\ space}} = -2k_0\ \mathrm{Im}[G_\omega(\xi,\xi)]. \qquad \text{(I-2. 7)}$$

There are at least two physical conditions that our 1-D LDOM should meet, i.e., that: (i) it account for the modification of dipole sheet emission rates with respect to emission rates in vacuum; (ii) it give the correct limiting value for the DOM of free space when calculated for a 1-D empty cavity whose dimensions go to infinity. The simplest way to satisfy these two requirements is to write the LDOM as:

$$\rho_\omega(\xi) \equiv \rho^{(1D)}_{\omega,\,free\,space}\frac{\overline{W}^{(1D)}_{emitted\ in\ PC}(\xi)}{\overline{W}^{(1D)}_{emitted\ in\ V,\ free\ space}} = -\frac{2k_0}{c}\mathrm{Im}[G_\omega(\xi,\xi)], \qquad \text{(I-2. 8)}$$

where $\rho^{(1D)}_{\omega,\,free\,space} = 1/c$ is the 1-D DOM of the free space [26]. The DOM is then the average of the LDOM over the volume V:

$$\rho_\omega \equiv \rho^{(1D)}_{\omega,\,free\,space}\frac{\left\langle\overline{W}^{(1D)}_{emitted\ in\ PC}(z)\right\rangle}{\overline{W}^{(1D)}_{emitted\ in\ V,\ free\ space}} = -\frac{2k_0}{cL}\int_0^L \mathrm{Im}[G_\omega(z,z)]dz, \qquad \text{(I-2. 9)}$$

where the integration variable ξ has been relabeled z. From Eqs. (I-2. 8) and (I-2. 9), we note that the DOM is defined in an unambiguous way because it is related to the power emitted by a dipole sheet in a 1-D PC. In the case the PC is composed by non absorbing materials, the mean power emitted by the dipole sheet is also equal to the mean power that flows through the surfaces A of the PC : $\overline{W}^{(1D)}_{emitted\,in\,PC} = \overline{W}_{flowing\ through\ A}$. So, we have arrived at an operational definition of the DOM and LDOM that can be directly linked to an experimental quantity, i.e., the emitted energy.

It is worth noting that the DOM is calculated as the average of the LDOM over the volume V, and not as the weighted average where the weight function is the real part of the dielectric function, $\varepsilon^R_\omega(z)$. The latter is a somewhat arbitrary operation which rescales the DOM by an equally arbitrary factor given by the real part of the dielectric constant. Although apparently unjustified, we will see later that this is consistent with the other approach which utilizes energy conservation arguments. However, we look at the consequences of choosing the DOM as the weighted average over $\varepsilon^R_\omega(z)$: $\rho^\varepsilon_\omega = -\frac{2k_0}{cL}\int_0^L \varepsilon^R_\omega(z)\mathrm{Im}[G_\omega(z,z)]dz$. From Eq.(I-2. 9) we obtain:

$$\rho_\omega = \frac{\rho^\varepsilon_\omega}{\left\langle\varepsilon^R_\omega\right\rangle} + \frac{2k_0}{cL\left\langle\varepsilon^R_\omega\right\rangle}\int_0^L \delta\varepsilon^R_\omega(z)\mathrm{Im}[G_\omega(z,z)]dz \qquad \text{(I-2. 10)}$$

where $\delta\varepsilon_\omega^R(z) = \varepsilon_\omega^R(z) - \langle \varepsilon_\omega^R \rangle$ represents the variation of the real part of the dielectric function with respect to its average value. In the case of structures with low index contrast ($|\delta\varepsilon_\omega^R(z)| << 1$), comparing Eqs.(I-2. 9) and (I-2. 10) we note that the two definitions are proportional to each other through a constant factor: $(\rho_\omega^\varepsilon / \rho_\omega) \cong \langle \varepsilon_\omega^R \rangle$. We will discuss the physical meaning of ρ_ω^ε in the next Section. For the time being, it becomes clear that ρ_ω^ε overestimates the power emitted by the dipole sheet of a factor that depends on the real part of the weight factor. In Fig. (I-2. 3) we compare ρ_ω and ρ_ω^ε for a 1-D PC composed of alternating layers of air and a non-absorbing dielectric material. The details of the structure are given in the caption. The structure is characterized by a high index contrast between the layers, and so the arguments about proportionality between the two competing definitions no longer hold. For example the ratios of

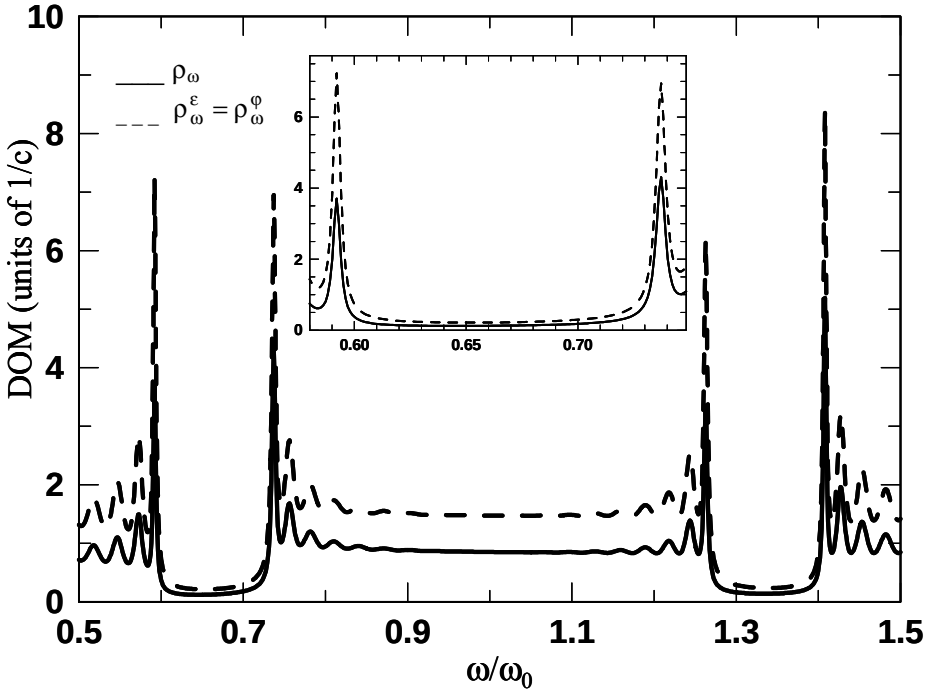

Fig. I-2. 3: ρ_ω (solid line) and $\rho_\omega^\varepsilon = \rho_\omega^\varphi$ (dashed line) vs. ω/ω_0 ($\omega_0=2\pi c/\lambda_0$ and $\lambda_0=1\mu m$) for a structure composed of 40 alternating layers of a dielectric material and air. The index of refraction of the dielectric material is 1.42857, and it is considered constant in the range of frequency examined. The layers have thicknesses a=350nm (dielectric material) and b=250nm (air) for a total length L=12μm. The structure is surrounded by air. Inset: Magnification of the DOM at the band edge resonances of the first gap. Note that ρ_ω and $\rho_\omega^\varepsilon = \rho_\omega^\varphi$ are not proportional each other through a constant factor: $\rho_\omega^\varepsilon / \rho_\omega \cong 1.94$ at $\omega/\omega_0=0.592$ (left-side band edge resonance) and $\rho_\omega^\varepsilon / \rho_\omega \cong 1.59$ at $\omega/\omega_0=0.737$ (right-side band edge resonance).

the DOMs at the band edge resonances of first band gap are respectively $\rho_\omega^\varepsilon / \rho_\omega \cong 1.94$ at ω/ω_0=0.592 (left-side band edge resonance) and $\rho_\omega^\varepsilon / \rho_\omega \cong 1.59$ at ω/ω_0=0.737 (right-side band edge resonance). The figure shows that in fact the two DOM are very different from each other, although the location of the relative maxima and minima remain approximately the same. We also note that for a non absorbing and non dispersive structure it can be demonstrated, as we will see in the next Section, that $\rho_\omega^\varepsilon = \rho_\omega^\varphi$, i.e., the DOM calculated by averaging the Green function over the grating profile is equal to the DOM calculated through the Wigner time. We will expand on the link between the DOM and the tunneling times in the next Section.

As defined in our Eq.(I-2. 9), the DOM maintains its generality when absorption and dispersion are present. In fact, the idea can be generalized to 2-D and 3-D structures of finite size. While in the 1-D case the source needs to have planar symmetry (infinite dipole sheet), in 2-D the source should have cylindrical symmetry (infinite wire), and in 3-D the source should have point symmetry (point source). In any case, the DOM can always be defined as the DOM of free space multiplied by the ratio between the spatial average of the mean power emitted by a source embedded within the PC and the mean power emitted by the source in the free space: $\rho_\omega \equiv \rho_{\omega,\,free\,space}^{(nD)} \dfrac{\left\langle \overline{W}_{emitted\,in\,PC}^{(nD)}(\vec{r}) \right\rangle}{\overline{W}_{emitted\,in\,V,\,free\,space}^{(nD)}}$, n=1,2,3, where $\rho_{\omega,\,free\,space}^{(1D)} = 1/c$, $\rho_{\omega,\,free\,space}^{(2D)} = \omega/c^2$, $\rho_{\omega,\,free\,space}^{(3D)} = \omega^2/(\pi c^3)$ are respectively the DOM of the free space in 1-D, 2-D and 3-D. The reader interested in the extension of Eq.(I-2. 9) to the case of finite size, 3-D structures can consult Ref. [27].

I-2.2 DOM calculated through the Wigner time and DOM calculated through the dwell time.

The DOM calculated using the Wigner time for 1-D, finite, structures is defined as follows [14]:

$$\rho_\omega^\varphi = \frac{1}{L}\frac{d\varphi_t}{d\omega} = \frac{\tau_\omega^\varphi}{L}, \qquad \text{(I-2. 11)}$$

where $\phi_t(\omega)$ is the phase of the transmission function. Defined in this fashion, $\tau_\omega^\varphi = \left(d\varphi_t / d\omega\right)$ is the Wigner[15-18], and it gives the time that the transmitted part of an incident, quasi-monochromatic, un-chirped pulse takes to traverse a 1-D, barrier [19-20]. Now, from Eq.(I-2.

A3), another way of writing the transmission for LTR propagation is $t_\omega^{(+)} = \Phi_\omega^{(+)}(L)$; taking the derivative with respect to the frequency, $dt_\omega^{(+)}/d\omega = \partial\Phi_\omega^{(+)}(L)/\partial\omega$, and rewriting the transmission in terms of a phase and an amplitude, i.e., $t_\omega^{(+)} = \left|t_\omega^{(+)}\right| \exp[i\varphi_t(\omega)]$ [28], we obtain:

$$\frac{d\left|t_\omega^{(+)}\right|}{d\omega}\exp(i\varphi_t) + i\frac{d\varphi_t}{d\omega}\left|t_\omega^{(+)}\right|\exp(i\varphi_t) = \frac{\partial\Phi_\omega^{(+)}(L)}{\partial\omega}. \qquad \text{(I-2. 12)}$$

Using Eqs.(I-2. 11)-(I-2. 12), the DOM can be recast as follows:

$$\rho_\omega^\varphi = \frac{1}{L}\mathrm{Im}\left[\frac{1}{t_\omega^{(+)}}\frac{\partial\Phi_\omega^{(+)}(L)}{\partial\omega}\right]. \qquad \text{(I-2. 13)}$$

The term $\partial\Phi_\omega^{(+)}(L)/\partial\omega$ can be calculated using the Green function of Eq.(I-2. 4) (see Appendix B):

$$\frac{\partial\Phi_\omega^{(+)}(L)}{\partial\omega} = -\frac{k_0}{c}\int_0^L\left[2\varepsilon_\omega(\xi) + \omega\frac{\partial\varepsilon_\omega(\xi)}{\partial\omega}\right]G_\omega(L,\xi)\Phi_\omega^{(+)}(\xi)d\xi. \qquad \text{(I-2. 14)}$$

From the expression for the Green function given in Eq.(I-2. 4), we have:

$$G_\omega(L,\xi) = \frac{\Phi_\omega^{(+)}(L)\Phi_\omega^{(-)}(\xi)}{2ik_0\tilde{t}_\omega} = \frac{\Phi_\omega^{(-)}(\xi)}{2ik_0 n_{0,2}}, \qquad \text{(I-2. 15)}$$

and from Eqs.(I-2. 12)-(I-2. 15) we obtain:

$$\rho_\omega^\varphi = -\frac{k_0}{cL}\mathrm{Im}\left[\frac{1}{2ik_0\tilde{t}_\omega}\int_0^L\left[2\varepsilon_\omega(z) + \omega\frac{\partial\varepsilon_\omega(z)}{\partial\omega}\right]\Phi_\omega^{(+)}(z)\Phi_\omega^{(-)}(z)dz\right], \qquad \text{(I-2. 16)}$$

where the integration variable ξ has been relabeled z. Eq.(I-2. 16) can be rewritten as follows:

$$\rho_\omega^\varphi = \rho_\omega^\varepsilon - \frac{2k_0}{cL}\int_0^L\varepsilon_\omega^I(z)\mathrm{Re}[G_\omega(z,z)]dz - \frac{k_0\omega}{cL}\int_0^L\left[\frac{\partial\varepsilon_\omega^R(z)}{\partial\omega}\mathrm{Im}[G_\omega(z,z)] + \frac{\partial\varepsilon_\omega^I(z)}{\partial\omega}\mathrm{Re}[G_\omega(z,z)]\right]dz, \qquad \text{(I-2. 17)}$$

where we have identified $\rho_\omega^\varepsilon = (-2k_0/cL)\int_0^L\varepsilon_\omega^R(z)\mathrm{Im}[G_\omega(z,z)]dz$ as the DOM calculated using the real part of the relative dielectric function as the weight function. Eq.(I-2. 17) provides an illuminating link between the different definitions of DOM. For the sake of clarity we analyze three cases: (a) No absorption and no dispersion; (b) Dispersion and negligible absorption; (c) Absorption and dispersion.

I-2.3 The case of no Absorption and no dispersion.

In this case from Eqs.(I-2. 17) and (I-2. 10) we obtain:

$$\rho_\omega^\varphi = \rho_\omega^\varepsilon = \left\langle \varepsilon_\omega^R \right\rangle \rho_\omega - \frac{2k_0}{cL}\int_0^L \delta\varepsilon_\omega^R(z)\,\mathrm{Im}[G_\omega(z,z)]dz\,. \qquad \text{(I-2. 18)}$$

Eq.(I-2. 18) tells us that in the absence of absorption and dispersion the DOM calculated through the Wigner time ρ_ω^φ is equal to the DOM calculated by averaging the Green function over the real part of the dielectric function. However, both ρ_ω^ε and ρ_ω overestimate the true DOM by a factor that is equal to the average value of the grating, $\left\langle \varepsilon_\omega^R \right\rangle$, with the addition of a term that depends on the index contrast. In the case of no absorption, ρ_ω^ε can also be expressed in a form involving the dwell time (see Appendix C) as:

$$\rho_\omega^\varepsilon = \frac{\tau_D^{(+)} + \tau_D^{(-)}}{2L} + \frac{1}{2ck_0L}\mathrm{Im}(r_\omega^{(+)} + r_\omega^{(-)}) \qquad \text{(I-2. 19)}$$

where $\tau_D^{(+)} = \left(2L\left\langle U_\omega^{(+)}\right\rangle\right)/cn_{01}$ and $\tau_D^{(-)} = \left(2L\left\langle U_\omega^{(-)}\right\rangle\right)/cn_{02}$, are the LTR and RTL dwell times respectively, and $U_\omega^{(\pm)} = \frac{1}{4}\left[\varepsilon_\omega^R(z)\left|\Phi_\omega^{(\pm)}(z)\right|^2 + \frac{c^2}{\omega^2}\left|\frac{d\Phi_\omega^{(\pm)}(z)}{dz}\right|^2\right]$ are the corresponding LTR and RTL time-averaged electromagnetic energy densities stored in the PC, for incident fields that have a harmonic time dependence of the type $e^{-i\omega t}$, and unitary amplitude (i.e. $\varepsilon_0\left|A_\omega^{(\pm)}\right|^2 = 1$, ε_0 is the vacuum dielectric constant, $A_\omega^{(\pm)}$ are the amplitudes of incident fields). The dwell time was first introduced for ballistic electrons, and was intended to measure the average time a quantum particle spends within a barrier, whether it is reflected and/or transmitted at the end of its stay [29-30]. In the case of electromagnetic radiation, the dwell time can be calculated by resorting to the electromagnetic energy density [31-32] as the ratio between the stored electromagnetic energy and the input power. Note that when $\left|r_\omega^{(\pm)}\right| = 0$ (i.e. at the peaks of transmission), $\rho_\omega^\varepsilon = \frac{\tau_D^{(+)} + \tau_D^{(-)}}{2L}$, that is to say, ρ_ω^ε is exactly the average of the LTR and RTL dwell times divided the length L of the PC. We point out that in most cases $k_0L>>1$ (equivalent to saying that the typical structure is much longer than the incident wavelength), and so the extra term

$\frac{1}{2ck_0L}\mathrm{Im}(r_\omega^{(+)}+r_\omega^{(-)})$ nearly always gives a maximum correction of the order of $10^{-2}L/c$ inside the gap[33]. As also noted in Ref.[31], this extra term comes from the fact that in a finite structure the energy density is not equally shared between the electric and magnetic components of the field. For symmetric or sufficiently long structures embedded in symmetric environments [34] it is straightforward to verify that $\langle U_\omega^{(+)}\rangle = \langle U_\omega^{(-)}\rangle = \langle U_\omega\rangle$, and consequently ρ_ω^ε takes the following simple form:

$$\rho_\omega^\varepsilon = \rho_\omega^U + \frac{|r_\omega|}{k_0\, c\, L}\sin\varphi_r\,, \qquad \text{(I-2. 20)}$$

where $\rho_\omega^U \equiv \frac{1}{2Lcn_0}\int_0^L\left[\varepsilon_\omega^R(z)|\Phi_\omega|^2 + \frac{c^2}{\omega^2}\left|\frac{d\Phi_\omega}{dz}\right|^2\right]dz = \frac{\tau_D}{L}$ is the DOM as it was first defined in

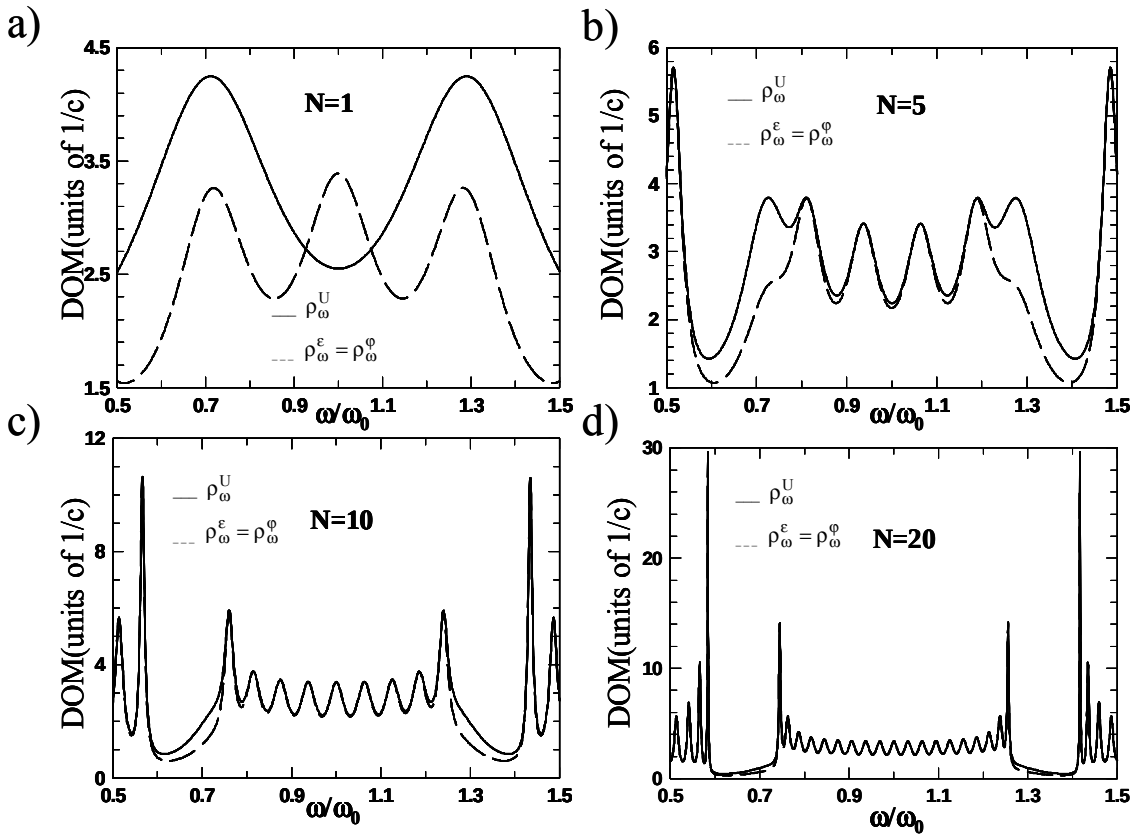

Fig. I-2. 4: ρ_ω^U (solid line) and $\rho_\omega^\varepsilon = \rho_\omega^\varphi$ (dashed line) vs. ω/ω_0 ($\omega_0=2\pi c/\lambda_0$ and $\lambda_0=1\mu m$) for PCs made by N=1, N=5, N=10, and N=20 periods, respectively. The elementary cell is composed of two layers of refractive index respectively $n_a=2$ and $n_b=3$. The thicknesses of the layers are a=125nm and b=166nm, respectively. The structure is surrounded by air.

Ref.[8] in terms of the electromagnetic energy density [3]. Eq.(I-2.20) provides new insight into the profound link that effectively binds the DOM calculated by averaging the Green's function over the grating, and the electromagnetic energy density, at least for non-absorbing structures. In addition, Eq.(I-2.20) provides a theoretical foundation for the numerical results reported in Ref. [8].

Some observations are now in order. We have shown that for a PC embedded in symmetric environments, $\rho_\omega^\varphi = \rho_\omega^\varepsilon$ is also approximately equal to ρ_ω^U. In Fig. (I-2. 4) we compare $\rho_\omega^\varphi = \rho_\omega^\varepsilon$ with ρ_ω^U for PC's made by the same elementary cell, repeated N=1, N=5, N=10, N=20 times, respectively. The details of the structures are given in the figure caption. We note that when N=20, the PC is practically equivalent to a symmetric structure, and $\rho_\omega^\varphi = \rho_\omega^\varepsilon \cong \rho_\omega^U$. The small discrepancy inside the gap is mostly due to the extra term $\frac{|r_\omega|}{k_0 c L}\sin\varphi_r$, and to a lesser degree to the small asymmetry built into the structure. In Fig. (I-2. 5) we compare $\rho_\omega^\varphi = \rho_\omega^\varepsilon$, ρ_ω^U and ρ_ω

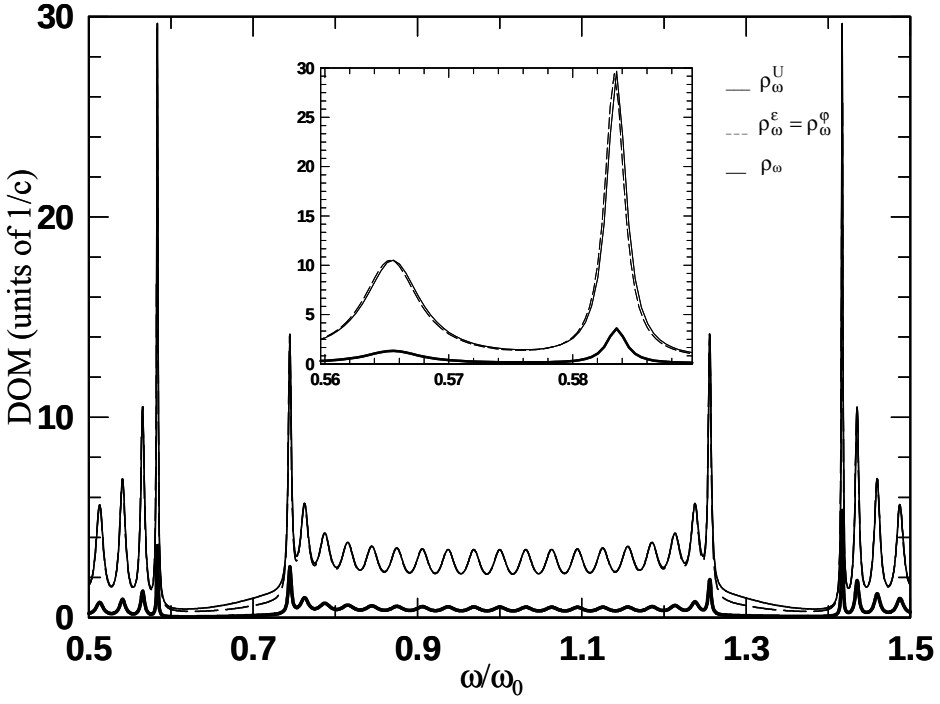

Fig. I-2. 5: ρ_ω^U (thin-solid line), $\rho_\omega^\varepsilon = \rho_\omega^\varphi$ (dashed line) and ρ_ω (thick-solid line) vs. ω/ω_0 ($\omega_0=2\pi c/\lambda_0$ and $\lambda_0=1\mu m$) for a PC made of N=20 periods. The elementary cell is the same described in the caption of figure 4. The structure is surrounded by air. Inset: Magnification of DOM at the two transmission resonance near the first band gap.

for 20-period structure. Again the figure reflects the fact that: $\rho_\omega^\varphi = \rho_\omega^\varepsilon \cong \rho_\omega^U$. However, all three DOMs consistently overestimate ρ_ω as already discussed (see Fig. (I-2. 3)).

The first non trivial implications of our results affect the relation between the tunneling times. From Eqs.(I-2. 11), (I-2. 18), and (I-2. 19) we obtain:

$$\tau_\omega^\varphi = \frac{\tau_D^{(+)} + \tau_D^{(-)}}{2} + \frac{1}{2\omega}\mathrm{Im}(r_\omega^{(+)} + r_\omega^{(-)}) . \qquad \text{(I-2. 21)}$$

Eq. (I-2. 21) tells us that for a non-absorbing, non-dispersive structure the Wigner time and the average (RTL and LTR) dwell time differ by an amount proportional to the average imaginary part of the RTL and LTR reflection coefficient. We note that this difference is zero at all transmission resonances, because there the energy density is equally shared by the electric and magnetic fields. Eq.(21) is a new result that clarifies the link between the Wigner time and the dwell time. In related work on tunneling times [32], a link between the Wigner time and the dwell time has also been pointed out. However, in Ref.[32] only the case of symmetric structures in symmetric environments was addressed, which is a particular case of our more general Eq.(I-2. 21). In fact, in the case of a symmetric structure located in a symmetric environment, $\tau_D^{(+)} = \tau_D^{(-)} = \tau_D$ and $r_\omega^{(+)} = r_\omega^{(-)} = r_\omega$, and from our Eq.(I-2. 21) we obtain:

$$\tau_\omega^\varphi = \tau_D + \frac{1}{\omega}\mathrm{Im}(r_\omega) \qquad \text{(I-2. 22)}$$

which is the result in ref.[32] There, the term $\tau_i = \frac{1}{\omega}\mathrm{Im}(r_\omega)$ is referred to as "self-interference delay". Again we stress that Eq.(I-2. 22) is not valid in general, because it was designed to handle symmetric structures located in symmetric environments. As a consequence, it does not predict the correct tunneling times for periodic structures having only a few periods.

To better clarify this point, in Fig. (I-2. 6) we compare the Wigner time and the dwell times, i.e., Eqs.(I-2. 21) and (I-2. 22), for a 5-period structure. In this case the LTR and RTL dwell times differ from each other, and only their average value converges to the Wigner time, as predicted by our Eq.(I-2. 21). As calculated by our Eq.(I-2. 21), the "self-interference delay" is of order 10^{-2}fs, a quantity that is hardly measurable in any experiment. Our results also suggest that the upper limit of the "self interference delay" available for any kind of structure can in fact be estimated from our Eq.(I-2. 21), namely, $|\tau_i|_{MAX} \le \frac{1}{\omega}$, which means $|\tau_i|_{MAX} \le 0.5\,fs$ for λ≅1μm,

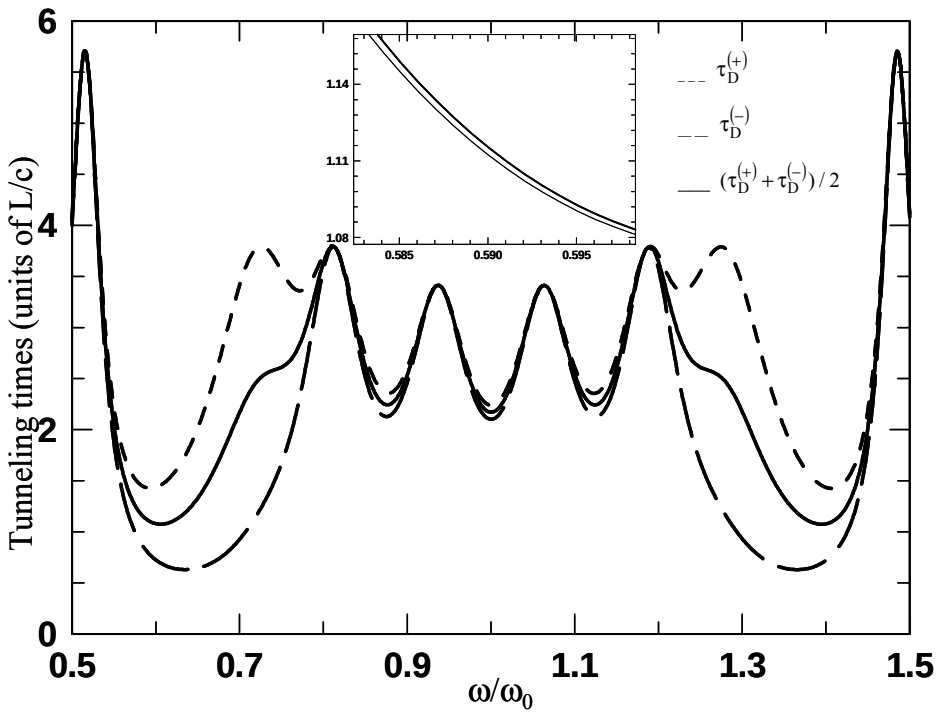

Fig. I-2. 6: LTR dwell time $\tau_D^{(+)}$ (short-dashed line), RTL dwell time $\tau_D^{(-)}$ (long-dashed line) and average dwell time $(\tau_D^{(+)} + \tau_D^{(-)})/2$ (thick solid line) vs. ω/ω_0 ($\omega_0=2\pi c/\lambda_0$ and $\lambda_0=1\mu m$) for a PC made of N=5 periods. L/c is in this case is 4.85fs. The elementary cell is the same described in the caption of figure 4. The figure contains also the Wigner time τ_ω^φ (thin solid line) but on this scale it is practically indistinguishable from the average dwell time. Inset: Magnification of the average dwell time (thick solid line) and the Wigner time (thin solid line). The difference between the two times is of the order of 10^{-2}fs.

and $|\tau_i|_{MAX} \le 0.1\,fs$ for λ=0.2μm. In units of (*L/c*), the upper limit of the available self interference delay is *1/(k0L)*. In the optical regime ($\lambda \cong 1 \div 0.2\mu m$) for PCs only a few micrometers in length, $k_0L \approx 10^{2}$, and the upper limit of the self interference delay available is of the order of $10^{-2}\,L/c$. In the structure considered in Fig. (I-2. 6), *L/c=4.85fs,* and the upper limit for the self interference delay in the range of frequency shown in the inset is approximately 0.8fs. This is compatible with the lower limit of 10^{-2}fs that is the difference between the average dwell time and the Wigner time. In summary, our results show that in most cases of interest, the correction due to the self interference delay is negligible in the optical regime, and that the Wigner time is for all intents and purposes approximately equal to the average of the LTR and RTL dwell times. In Ref.[31] it was demonstrated that beginning with the definition of energy velocity as the ratio between the spatially averaged Poynting vector and the spatially averaged energy density, $V_E^{(\pm)} = \langle S_\omega^{(\pm)} \rangle / \langle U_\omega^{(\pm)} \rangle$, it is then possible to arrive at a simple relation that links the energy

velocity to the dwell time, namely $V_E^{(\pm)} = \left|t_\omega^{(\pm)}\right|^2 (L/\tau_D^{(\pm)})$. Now, by using Eq.(I-2. 21) and the connection of the dwell time with the energy velocity, we arrive at the following equivalence:

$$\tau_\omega^\varphi = \frac{L}{2}\frac{\left|t_\omega^{(+)}\right|^2 V_E^{(-)} + \left|t_\omega^{(-)}\right|^2 V_E^{(+)}}{V_E^{(+)} V_E^{(-)}} + \frac{1}{2\omega}\mathrm{Im}(r_\omega^{(+)} + r_\omega^{(-)}) . \qquad \text{(I-2. 23)}$$

From Eq.(I-2. 23), once again for the case of a symmetric structure embedded in a symmetric environment, and neglecting the corrective term $\frac{1}{2\omega}\mathrm{Im}(r_\omega^{(+)} + r_\omega^{(-)})$ on the right hand side of Eq.(I-2. 23), we obtain: $V_E \cong \left|t\right|^2 V_g$, [31] where $V_g = L/\tau_\omega^\varphi$ is the group or tunneling velocity. Therefore, our Eq.(I-2. 23) confirms and extends the results first reported in Ref.[31]

I-2.4 The case of dispersion with negligible absorption.

In the case at hand, from Eq.(I-2. 17) we obtain:

$$\rho_\omega^\varphi = \rho_\omega^\varepsilon - \frac{k_0\omega}{cL}\int_0^L \left[\frac{\partial\varepsilon_\omega^R(z)}{\partial\omega}\mathrm{Im}[G_\omega(z,z)]\right]dz . \qquad \text{(I-2. 24)}$$

Using the explicit expression for ρ_ω^ε, Eq.(I-2. 24) can be recast in the following form:

$$\rho_\omega^\varphi = (-2k_0/cL)\int_0^L \left[\varepsilon_\omega^R(z) + \frac{\omega}{2}\frac{\partial\varepsilon_\omega^R(z)}{\partial\omega}\right]\mathrm{Im}[G_\omega(z,z)]dz \qquad \text{(I-2. 25)}$$

Eq.(I-2. 25) suggests that the DOM is calculated by averaging the imaginary part of the Green's function over the weight function: $\varepsilon_\omega^R(z) + \frac{\omega}{2}\frac{\partial\varepsilon_\omega^R(z)}{\partial\omega}$. In analogy with the definition of ρ_ω^ε, we can define $\rho_\omega^{\varepsilon+\frac{\omega}{2}\frac{\partial\varepsilon}{\partial\omega}} \equiv (-2k_0/cL)\int_0^L \left[\varepsilon_\omega^R(z) + \frac{\omega}{2}\frac{\partial\varepsilon_\omega^R(z)}{\partial\omega}\right]\mathrm{Im}[G_\omega(z,z)]dz$ and we can rewrite Eq.(I-2. 25) in a more concise form as:

$$\rho_\omega^\varphi = \rho_\omega^{\varepsilon+\frac{\omega}{2}\frac{\partial\varepsilon}{\partial\omega}} . \qquad \text{(I-2. 26)}$$

Now, using the explicit expression of the imaginary part of the Green's function in terms of the light modes (see Eq. I-2. C7 in Appendix C) and using the following relation: $\int_0^L \varepsilon_\omega^R(z)\left|\Phi_\omega^{(\pm)}\right|^2 dz = \left(c^2/\omega^2\right)\int_0^L \left|d\Phi^{(\pm)}/dz\right|^2 dz + \left(1/k_0\right)n_{01,2}\,\mathrm{Im}\left[r_\omega^{(\pm)}\right]$ we can write $\rho_\omega^{\varepsilon+\frac{\omega}{2}\frac{\partial\varepsilon}{\partial\omega}}$ in a form that involves again the dwell times:

$$\rho_{\omega}^{\varepsilon+\frac{\omega\,\partial\varepsilon}{2\,\partial\omega}} = \frac{\tau_D^{(+)} + \tau_D^{(-)}}{2L} + \frac{1}{2ck_0 L}\,\mathrm{Im}(r_{\omega}^{(+)} + r_{\omega}^{(-)}) \qquad \text{(I-2. 27)}$$

where $\tau_D^{(+)} = \left(2L\left\langle U_{\omega}^{(+)}\right\rangle\right)/cn_{01}$ and $\tau_D^{(-)} = \left(2L\left\langle U_{\omega}^{(-)}\right\rangle\right)/cn_{02}$, are the LTR and RTL dwell times, respectively, and $U_{\omega}^{(\pm)} = \frac{1}{4}\left[\frac{\partial}{\partial\omega}\left[\omega\varepsilon_{\omega}^{R}(z)\right]\left|\Phi_{\omega}^{(\pm)}(z)\right|^2 + \frac{c^2}{\omega^2}\left|\frac{d\Phi_{\omega}^{(\pm)}(z)}{dz}\right|^2\right]$ are the corresponding time-averaged electromagnetic energies calculated taking into account the dispersion of the medium [36]. Therefore all the connections between the Wigner time and the dwell time and their relationships with the DOM that were demonstrated for the case of no absorption and no dispersion are still valid in the case of dispersion and negligible absorption, provided the energy density is calculated taking into account the dispersion of the medium.

I-2.5 The case of absorption and dispersion

When the absorption of the material comes into play the DOM calculated using the Wigner time can become negative near the absorption line of the material. Therefore, it can no longer be interpreted as a DOM in the true sense of the word. On the other hand, the DOM defined through Eq.(I-2. 9) continues to be a positive quantity, and maintains the physical meaning of a quantity proportional to the mean power emitted by a source located inside the PC, as outlined at length in Section 2. In Fig.(I-2. 7a) we compare the DOM calculated using the Wigner time, (dashed line) and the DOM calculated using Eq.(I-2. 9) (solid line) for the same structure described in the caption of Fig. (I-2. 3), except that the high index layer is endowed with a Lorentzian absorption line centered around ω/ω_0=0.65, and a refractive index approximately of 1.42 in the visible range. The refraction index (n) and the extinction coefficient (β) of the high index layer are shown in Fig. (I-2. 7b). The figure shows that the DOM calculated via the Wigner time attains negative values near the center of the absorption line of the dielectric material ($\rho_{\omega}^{\varphi} \cong -2/c$ at $\omega/\omega_0 \cong$0.66), while Eq.(I-2. 9) always gives a positive DOM. While this shortcoming clearly implies that the Wigner time fails to adequately describe the DOM, it nevertheless continues to be a good indicator of the tunneling time imparted to the peak of the transmitted part of an input, quasi-monochromatic, un-chirped pulse as it traverses a 1-D barrier. In fact, it is well known that the transit time of pulses tuned near the absorption line of a dielectric material can become superluminal or even negative as in our case [37-39]. Of course, superluminal or negative transit times are not an indication that causality or relativity somehow break down, because the fact is

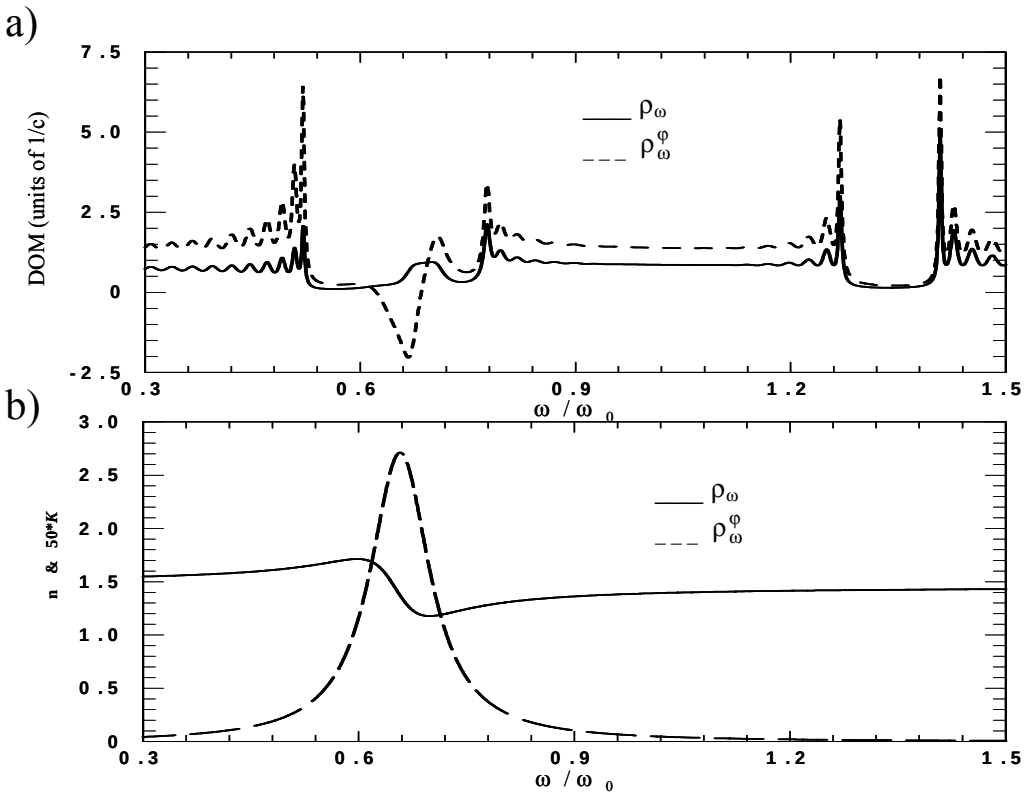

Fig. I-2. 7: (a) ρ_ω (solid line) and ρ_ω^φ (dashed line) vs. ω/ω_0 ($\omega_0=2\pi c/\lambda_0$ and $\lambda_0=1\mu m$) for the same structure described in Fig.(I-2. 3) except that the high index layer now includes a dielectric material with a Lorentzian absorption line centered around $\omega/\omega_0=0.65$ and an index of refraction of approximately 1.42 in the visible range. **(b)** Refractive index (*n*) (solid line) and extinction coefficient (β) (dashed line) of the dielectric material vs. ω/ω_0. By definition the refractive index and the extinction coefficient are related to the dielectric function by: $\sqrt{\varepsilon} = n + i\beta$. The extinction coefficient is magnified 50 times.

that signal velocity always remains subluminal [40], and the peak of the transmitted pulse can always be found under the envelope of a similar input pulse propagating for the same length of free space [20]. In Fig. (I-2. 8a) we compare the Wigner time and the transit time of a Gaussian pulse of unitary amplitude that traverses the structure. Input pulses at z=0 (z=0 is the location of the input surface of the PC) have the following form: $A(z=0,t)=\exp\left[-\left(t^2/2\tau_0^{\,2}\right)-i\omega t\right]$ where $\tau_0 = 0.5\,ps$ and ω is the carrier frequency. The transit time has been numerically calculated as the time the peak of the transmitted part of the input pulse needs to exit the structure, and the reference time (t=0) is the time at which the peak of the input pulse reaches the input surface of the PC. The figure shows that the transit time is well described by the Wigner time, even when

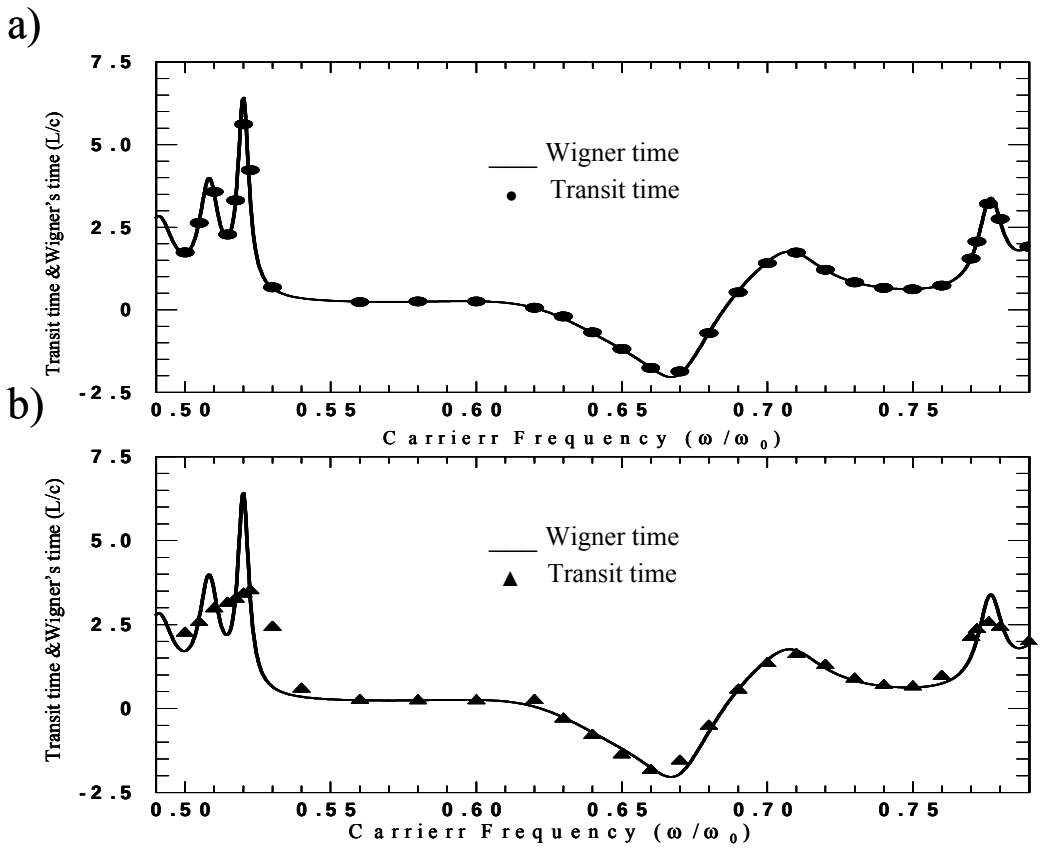

Fig. I-2. 8: (a) Transit time (solid circles) and Wigner time (solid line) vs. ω/ω_0 ($\omega_0=2\pi c/\lambda_0$ and $\lambda_0=1\mu m$) where ω is the carrier frequency of the input pulse. The structure is the same as that described in Fig. (I-2. 7). Input pulses at z=0 (z=0 is the location of the input surface of the PC) have the following form: $A(z=0,t)=\exp\left[-\left(t^2/2\tau_0{}^2\right)-i\omega t\right]$ where $\tau_0=0.5ps$. The transit time has been calculated as the time the peak of the transmitted part of the input pulse needs to exit the structure, and the reference time (t=0) is the time when the peak of the input pulse reaches the input surface of the PC. **(b)** Tansit time (solid triangles) and Wigner time (solid line) in the case of a Gaussian pulse with $\tau_0=0.1ps$

strong absorption and dispersion come into play. In this case the spectral bandwidth of the input pulse is ~ 6 THz, which corresponds to ~ 0.83 ps FWHM of the pulse intensity, and the quasi-monochromatic limit is approached (this limit is quickly reached because the spatial extension of a typical pulse is always much larger than the typical structure, which is only a few microns in length). The transmitted pulses come out only slightly distorted with respect to the input pulses, and attenuated by a factor that depends on the transmission properties of the PC. In general, in the presence of absorption, the Wigner time correctly estimates the transit time for any quasi-monochromatic Fourier-limited pulse. In the case of a quasi-monochromatic linearly chirped

pulse, the transit time is related to the Wigner time through the relation: $t_{transit}=t_{Wigner}+\delta\gamma\Delta t^2$, where $\delta=[(dT/d\omega)/T]_{\omega=\omega 0}$ and γ is the magnitude of the linear chirp [20].

If shorter pulses were used, as in Fig. (I-2. 8b), where the pulses have a duration in time of approximately 0.16 ps FWHM of the pulse intensity, the transit time then begins to differ significantly from the Wigner time. In this case higher order terms of the geometrical dispersion of the structure that are not accounted by the Wigner time come into play, and as a consequence pulses that tunnel through the structure undergo appreciable distortion.

Conclusions

In conclusion, we have highlighted the connections that exist between the DOM and tunneling times for 1-D barriers. In the absence of absorption, the DOM calculated using the Wigner time is approximately equal to the average of the LTR and RTL dwell times, divided the length L of the structure. We have shown that the self-interference delay is generally negligible (Eqs.(I-2. 19) and (I-2. 20), and Fig. (I-2. 6). Both the Wigner and dwell-time DOMs *overestimate* the true DOM defined in our Eq.(I-2. 9) by a factor roughly proportional to the average index of the barrier (Eq.(I-2. 18), and Figs.(I-2. 3) and (I-2. 5)). Structures embedded in symmetric environments composed of a sufficient number of periods acquire the properties of symmetric structures, and the DOM calculated through the Wigner time is then approximately equal to the DOM calculated using the energy density (Eq.(I-2. 20) and Fig.(I-2. 4)), as first proposed in Ref.[8] using heuristic arguments. In the case the absorption, the Wigner DOM can become negative (see Fig. (I-2. 7)), while the true DOM remains always positive. In that case, the Wigner DOM ceases to be a valid representation of DOM, but can still be interpreted and is still a good measure of group velocity of un-chirped, quasi-monochromatic pulses. We conclude that the DOM in 1-D barriers should always be calculated using our Eq.(I-2. 9), and plenty of caution should be exercised when one makes connections between the DOM and tunneling times. Such a connection sometimes yields useful information about the system, such as group velocity, for example, but if the true DOM is sought the approach suggested by our Eq.(I-2. 9) should always be preferred.

Finally, we point out that while the DOM defined through Eq.(I-2. 9) can be straightforwardly generalized to multidimensional cases, the other definitions based on the tunneling times find a direct link with the DOM only in one dimension, and then only when there is no absorption.

I-2.A Appendix A

We begin with Eq.(I-2. 3):

$$\frac{\partial^2 G_\omega(z,\xi)}{\partial z^2}+\frac{\omega^2\varepsilon_\omega(z)G_\omega(z,\xi)}{c^2}=\delta(z-\xi) \qquad \text{(I-2. A1)}$$

when $G_\omega(z,\xi)$ exists, it follows that $G_\omega(z,\xi)$ satisfies the homogeneous equation:

$$\frac{\partial^2 G_\omega(z,\xi)}{\partial z^2}+\frac{\omega^2\varepsilon_\omega(z)G_\omega(z,\xi)}{c^2}=0\,, \qquad \text{(I-2. A2)}$$

at all points of the interval 0≤z≤L except at the point z=ξ. As discussed at length in Ref. [24], the light-modes $\left\{\Phi_\omega^{(\pm)}\right\}$ are a fundamental (you mean complete?) set of solutions of Eq.(I-2. A2) and they are subject to the following boundary conditions (see Fig. (I-2. 2)):

$$\begin{cases} \Phi_\omega^{(+)}(0)=1+r_\omega^{(+)} \\ \Phi_\omega^{(+)}(L)=t_\omega^{(+)} \\ [d\Phi_\omega^{(+)}/dz]_{z=0}=ik_0n_{0,1}(1-r_\omega^{(+)}) \\ [d\Phi_\omega^{(+)}/dz]_{z=L}=ik_0n_{0,2}t_\omega \end{cases}, \quad \begin{cases} \Phi_\omega^{(-)}(0)=t_\omega^{(-)} \\ \Phi_\omega^{(-)}(L)=1+r_\omega^{(-)} \\ [d\Phi_\omega^{(-)}/dz]_{z=0}=-ik_0n_{0,1}t_\omega \\ [d\Phi_\omega^{(-)}/dz]_{z=L}=ik_0n_{0,2}(r_\omega^{(-)}-1) \end{cases}. \qquad \text{(I-2. A3)}$$

Consequently, we can express the most general solution of Eq.(I-2. A1) as:

$$G_\omega(z,\xi)=\begin{cases} C_1(\xi)\Phi_\omega^{(+)}(z)+D_1(\xi)\Phi_\omega^{(-)}(z) & L\ge z>\xi \\ \\ D_2(\xi)\Phi_\omega^{(+)}(z)+C_2(\xi)\Phi_\omega^{(-)}(z) & 0\le z<\xi \end{cases} \qquad \text{(I-2. A4)}$$

The four constants must now be determined. First we impose the condition of *"outgoing waves"*. This condition requires that the radiated energy from the point source located at z=ξ leaves the structure, and no energy is incoming into the structure. This means that the coefficients D_1 of the incoming RTL wave and the coefficient D_2 of the incoming LTR wave must be zero. The constant C_1 and C_2 must be determined by imposing the continuity of $G_\omega(z,\xi)$ at z=ξ, while iits derivative has a jump of magnitude one [25]. Following the above procedure we find:

$$\begin{cases} C_1(\xi)=\dfrac{\Phi_\omega^{(-)}(\xi)}{\left[W\left(\Phi_\omega^{(-)},\Phi_\omega^{(+)}\right)\right]_{z=\xi}}\,,\ D_1=0 \\ C_2(\xi)=\dfrac{\Phi_\omega^{(+)}(\xi)}{\left[W\left(\Phi_\omega^{(-)},\Phi_\omega^{(+)}\right)\right]_{z=\xi}}\,,\ D_2=0 \end{cases}, \qquad \text{(I-2. A5)}$$

where $W\left(\Phi_{\omega}^{(-)},\Phi_{\omega}^{(+)}\right)\equiv\begin{vmatrix}\Phi_{\omega}^{(-)} & \Phi_{\omega}^{(+)}\\ d\Phi_{\omega}^{(-)}/dz & d\Phi_{\omega}^{(+)}/dz\end{vmatrix}$ is the Wronskian of the fundamental set of solutions. In our case the Wronskian is a conserved quantity, i.e. $dW\left(\Phi_{\omega}^{(-)},\Phi_{\omega}^{(+)}\right)/dz=0$. This can be shown by resorting to the boundary conditions in Eq.(I-2. A3). The result is: $\left[W\left(\Phi_{\omega}^{(-)},\Phi_{\omega}^{(+)}\right)\right]_{z=\xi}=\left[W\left(\Phi_{\omega}^{(-)},\Phi_{\omega}^{(+)}\right)\right]_{z=0}=2ik_0n_{0,1}t_{\omega}^{(-)}=\left[W\left(\Phi_{\omega}^{(-)},\Phi_{\omega}^{(+)}\right)\right]_{z=L}=2ik_0n_{0,2}t_{\omega}^{(+)}$, from which one also derives that $n_{0,1}t_{\omega}^{(-)}=n_{0,2}t_{\omega}^{(+)}=\tilde{t}_{\omega}$. The Wronskian calculated at the point z=ξ can be consequently expressed as:

$$W\left(\Phi_{\omega}^{(-)},\Phi_{\omega}^{(+)}\right)=\left[W\left(\Phi_{\omega}^{(-)},\Phi_{\omega}^{(+)}\right)\right]_{z=\xi}=2ik_0\tilde{t}_{\omega}\ . \qquad \text{(I-2. A6)}$$

Eq.(I-2. 4) in the main text follows from Eqs.(I-2. A4),(I-2. A5),(I-2. A6).

I-2.B Appendix B

We start by writing the Helmholtz equation for the field $\Phi^{(+)}_{\omega+\delta\omega}(z)$:

$$\frac{\partial^2 \Phi^{(+)}_{\omega+\delta\omega}(z)}{\partial z^2} + \frac{(\omega+\delta\omega)^2 \varepsilon_{\omega+\delta\omega}(z) \Phi^{(+)}_{\omega+\delta\omega}(z)}{c^2} = 0 . \qquad \text{(I-2. B1)}$$

Let us write $\delta\omega = \lambda\omega$ where λ<<1 is a perturbation parameter, and let us expand the functions in Taylor series:

$$\Phi^{(+)}_{\omega+\delta\omega}(z) = \Phi^{(+)}_{\omega}(z) + \lambda \Gamma_{\omega}(z) + \ldots , \qquad \text{(I-2. B2.1)}$$

$$(\omega+\delta\omega)^2 \varepsilon_{\omega+\delta\omega}(z) = \omega^2 \varepsilon_{\omega}(z) + \lambda \left[2\omega^2 \varepsilon_{\omega}(z) + \omega^3 \frac{\partial \varepsilon_{\omega}(z)}{\partial \omega} \right] + ... , \qquad \text{(I-2. B2.2)}$$

where $\Gamma_{\omega}(z) = \omega\left(\partial \Phi^{(+)}_{\omega}(z) / \partial \omega\right)$. By substituting Eqs.(I-2. B2.1) and (I-2. B2.2) in Eq.(I-2. B1) and equating the terms of order λ, we obtain the following equation for $\Gamma_{\omega}(z)$:

$$\frac{\partial^2 \Gamma_{\omega}(z)}{\partial z^2} + \frac{\omega^2 \varepsilon_{\omega}(z)}{c^2} \Gamma_{\omega}(z) = -\frac{\omega^2}{c^2} \Phi^{(+)}_{\omega}(z) \left[2\varepsilon_{\omega}(z) + \frac{\partial \varepsilon_{\omega}(z)}{\partial \omega} \omega \right]. \qquad \text{(I-2. B3)}$$

The solution of second order linear differential equations of the same type as that in Eq.(I-2. B3) can be written using the method of the Green's function [25]. In our case, the solution of Eq.(I-2. B3) with the boundary conditions corresponding to "outgoing waves" can be expressed in terms of the Green function calculated in Appendix A as follows:

$$\Gamma_{\omega}(z) = -\frac{\omega^2}{c^2} \int_0^L G_{\omega}(z,\xi) \Phi^{(+)}_{\omega}(\xi) \left[2\varepsilon_{\omega}(\xi) + \frac{\partial \varepsilon_{\omega}(\xi)}{\partial \omega} \omega \right] d\xi , \qquad \text{(I-2. B4)}$$

by calculating Eq.(I-2. B4) for $z=L$ we obtain Eq.(I-2. 14) in the main text.

I-2.C Appendix C

Let us start from the definition of ρ_ω^ε:

$$\rho_\omega^\varepsilon = (-2k_0 / cL)\int_0^L \varepsilon_\omega^R(z)\,\mathrm{Im}[G_\omega(z,z)]dz\,. \qquad \text{(I-2. C1)}$$

Eq.(I-2. C1) can be rewritten in the following form :

$$\rho_\omega^\varepsilon = \frac{1}{cL|\tilde{t}_\omega|}\int_0^L \varepsilon_\omega^R(z)\left|\Phi_\omega^{(+)}\right|\left|\Phi_\omega^{(-)}\right|\cos\left[\varphi_\omega^{(+)} + \varphi_\omega^{(-)} - \varphi_t\right]dz\,, \qquad \text{(I-2. C2)}$$

where we have used the expression of the Green's function given by Eq.(I-2. 4) in the main text, we have written the LTR and RTL modes as: $\Phi_\omega^{(\pm)}(z) = \left|\Phi_\omega^{(\pm)}(z)\right|\exp\left(i\varphi_\omega^{(\pm)}\right)$, and the transmission function of the PC as: $\tilde{t}_\omega = |\tilde{t}_\omega|\exp[i\varphi_t(\omega)]$. Now, equating the real and imaginary parts of Eq.(I-2. A6), we obtain:

$$\left|\Phi_\omega^{(-)}\right|\frac{d\left|\Phi_\omega^{(+)}\right|}{dz} - \left|\Phi_\omega^{(+)}\right|\frac{d\left|\Phi_\omega^{(-)}\right|}{dz} = 2k_0|\tilde{t}_\omega|\sin\left[\varphi_\omega^{(+)} + \varphi_\omega^{(-)} - \varphi_t\right], \qquad \text{(I-2. C3.1)}$$

$$\left|\Phi_\omega^{(+)}\right|\left|\Phi_\omega^{(-)}\right|\left[\frac{d\varphi_\omega^{(+)}}{dz} - \frac{d\varphi_\omega^{(-)}}{dz}\right] = 2k_0|\tilde{t}_\omega|\cos\left[\varphi_\omega^{(+)} + \varphi_\omega^{(-)} - \varphi_t\right]. \qquad \text{(I-2. C3.2)}$$

Using Eq.(I-2. C3.2), we can recast Eq.(I-2. C2) in the following form:

$$\rho_\omega^\varepsilon = \frac{1}{2k_0 cL|\tilde{t}_\omega|^2}\int_0^L \varepsilon_\omega^R(z)\left|\Phi_\omega^{(+)}\right|^2\left|\Phi_\omega^{(-)}\right|^2\left[\frac{d\varphi_\omega^{(+)}}{dz} - \frac{d\varphi_\omega^{(-)}}{dz}\right]dz\,. \qquad \text{(I-2. C4)}$$

For a non-absorbing PC, i.e. $\varepsilon_\omega^I(z) = 0$, it can be shown that $\left|\Phi_\omega^{(\pm)}(z)\right|^2(d\varphi_\omega^{(\pm)}/dz)$ is a conserved quantity [31] and it can be calculated by resorting to the boundary conditions imposed on the LTR and RTL modes, i.e. Eqs.(I-2. A3), giving the following results:

$$\left|\Phi_\omega^{(+)}\right|^2\frac{d\varphi_\omega^{(+)}}{dz} = +\frac{k_0}{n_{02}}|\tilde{t}_\omega|^2, \qquad \text{(I-2. C5.1)}$$

$$\left|\Phi_\omega^{(-)}\right|^2\frac{d\varphi_\omega^{(-)}}{dz} = -\frac{k_0}{n_{01}}|\tilde{t}_\omega|^2\,. \qquad \text{(I-2. C5.2)}$$

From Eqs.(I-2. C5) and (I-2. C4) we obtain:

$$\rho_\omega^\varepsilon = \frac{1}{2cLn_{0,1}n_{0,2}}\int_0^L \varepsilon_\omega^R(z)\left[n_{0,2}\left|\Phi_\omega^{(+)}\right|^2 + n_{0,1}\left|\Phi_\omega^{(-)}\right|^2\right]dz\,, \qquad \text{(I-2. C6)}$$

and we also arrive to an useful expression of the imaginary part of the Green's function in terms of the LTR and RTL light modes:

$$\mathrm{Im}[G_\omega(z,z)] = -\frac{1}{4k_0}\left[\frac{n_{0,2}\left|\Phi_\omega^{(+)}\right|^2 + n_{0,1}\left|\Phi_\omega^{(-)}\right|^2}{n_{0,1}n_{0,2}}^2\right]. \qquad \text{(I-2. C7)}$$

Now, using the relation: $\int_0^L \varepsilon_\omega^R(z)\left|\Phi_\omega^{(\pm)}\right|^2 dz = \left(c^2/\omega^2\right)\int_0^L \left|d\Phi^{(\pm)}/dz\right|^2 dz + \left(1/k_0\right)n_{01,2}\,\mathrm{Im}\left[r_\omega^{(\pm)}\right]$ [8],[31], Eq.(I-2. C6) can be recast in the following form:

$$\rho_\omega^\varepsilon = \frac{1}{4cL}\left\{\frac{1}{n_{0,1}}\int_0^L\left[\varepsilon_\omega^R\left|\Phi_\omega^{(+)}\right|^2 + \frac{c^2}{\omega^2}\left|\frac{d\Phi^{(+)}}{dz}\right|^2\right]dz + \frac{1}{n_{0,2}}\int_0^L\left[\varepsilon_\omega^R\left|\Phi_\omega^{(-)}\right|^2 + \frac{c^2}{\omega^2}\left|\frac{d\Phi^{(-)}}{dz}\right|^2\right]dz + \frac{2}{k_0}\mathrm{Im}(r_\omega^{(+)} + r_\omega^{(-)})\right\} \qquad \text{(I-2. C8)}$$

The dwell time is defined as the average electromagnetic energy density stored in the structure divided by the input power [31-32]. In our case the expression for the dwell times for a LTR and RTL input are respectively:

$$\tau_D^{(\pm)} = \frac{1}{2cn^{(\pm)}}\int_0^L\left[\varepsilon_\omega^R\left|\Phi_\omega^{(\pm)}\right|^2 + \frac{c^2}{\omega^2}\left|\frac{d\Phi^{(\pm)}}{dz}\right|^2\right]dz\,, \qquad \text{(I-2. C9)}$$

where $n^{(+)} = n_{0,1}$ and $n^{(-)} = n_{0,2}$. Eq.(I-2. 19) in the main text comes from Eq.(I-2. C8) and (I-2. C9).

References and Notes

[1] E. Yablonovitch, *Phys. Rev. Lett.* **58**, 2059-2062 (1987)

[2] S. John, *Phys. Rev. Lett.* **58**, 2486-2489 (1987)

[3] J.C. Knight, T.A. Birks, P.St.J. Russel, D.M. Atkin, *Opt. Lett*. **21,** 1547-1549 (1996)

[4] J.D. Joannopoulos, P.R. Villeneuve, S.H. Fan, *Nature* **386**, 143-149 (1997)

[5] M.J. Bloemer and M. Scalora, *Appl. Phys. Lett.* **72**, 1676-1678 (1998)

[6] M. Scalora, M.J. Bloemer, C.M. Bowden, G. D'Aguanno, M. Centini, C. Sibilia, M. Bertolotti, Y. Dumeige, I. Sagnes, P. Vidakovic, A. Levenson, *Opt. & Photon. News* **12**, 36-40 (2001).

[7] Y. Dumeige, P. Vidakovic, S. Sauvage, I. Sagnes, J.A. Levenson, C.Sibilia, M.Centini, G.D'Aguanno, M.Scalora, *Appl. Phys. Lett.* **78**, 3021-3023 (2001).

[8] G. D'Aguanno, M. Centini, M. Scalora, C. Sibilia, Y. Dumeige, P. Vidakovic, J.A. Levenson, M.J. Bloemer, C.M. Bowden, J.W. Haus, M. Bertolotti, *Phys. Rev. E* **64,** 16609-1-9 (2001).(and references therein)

[9] M. Bertolotti, C..M. Bowden, C. Sibilia Editors "Nanoscale linear and nonlinear optics", AIP Conference Proceedings, Volume 560, New York 2001

[10] C.M. Bowden and A. Zheltikov eds., Special issue on "Nonlinear Optics of Photonic Crystals", *JOSA B* , **19** (2002).

[11] E.N. Economou "Green's Functions in Quantum Physics" , Springer-Verlag, Berlin (1983).

[12] P. Sheng, "Introduction to Wave Scattering, Localization, and Mesoscopic Phenomena" Academic Press, San Diego, 1995.

[13] A.A. Asatryan, K. Busch, R.C. McPhedran, L.C. Botten, C.Martijn de Sterke, N.A. Nicorovici, *Phys. Rev. E* **63,** 046612-1-4 (2001).

[14] J. M. Bendickson, J.P Dowling, M. Scalora, *Phys. Rev E* **53**, 4107-4121 (1996).

[15] E.H. Hauge and J.A. StØvneng, Rev. Mod. Phys. **61**, 917-936 (1989).

[16] A.M. Steinberg, P.G. Kwiat, and R.T. Chiao, *Phys. Rev. Lett*. **71,** 708 (1993).

[17] R.T. Chiao and A.M. Steinberg, in *Progress in Optics,* edited by E. Wolf (Elsevier Science, North-Holland, Amsterdam, 1997), Vol.XXXVII, p.345

[18] E.P. Wigner, *Phys. Rev* **98**, 145 (1955).

[19] M. Scalora, R. J. Flynn, S. B. Reinhardt, R. L. Fork, M. D. Tocci, M. J. Bloemer, C. M. Bowden, H. S. Ledbetter, J. M. Bendickson, J. P. Dowling, and R. P. Leavitt, *Phys. Rev. E* **54,** 1078-1082 (1996).

[20] G. D'Aguanno, M. Centini, M.J. Bloemer, K. Myneni, M. Scalora, C.M. Bowden, C. Sibilia, M. Bertolotti, *Opt. Lett.* **27**, 176-178 (2002).

[21] D.L. Mills and A.A. Maradudin, *Phys. Rev. B* **12,** 2943-2958 (1975).

[22] M.S. Tomas, "Green function for multilayers: Light scattering in planar cavities," *Phys. Rev. A* **51,** 2545-2559 (1995).

[23] O. Di Stefano, S. Savasta, R. Girlanda, *J. of Mod. Opt.* **48,** 67-84 (2001).

[24] G. D'Aguanno, M. Centini, M.Scalora, C. Sibilia, M. Bertolotti, M.J. Bloemer, C.M. Bowden, *JOSA B* , **19** 2111-2121 (2002)

[25] The reader interested in the basic theory of Green's function may consult: P. Dennery and A. Krzywicki, "Mathematics For Physicist", Dover Publications,Inc. New York (1967). In particular see Chp.IV pp.257-291. More extensive analysis can be found in: F.N. Byron, Jr., R.W. Fuller, "Mathematics of Classical and Quantum Physics, Vol. II , Addison-Wesley, Reading, Mass. (1969) or in : P.M. Morse, H. Feshbach , " Methods of Theoretical Physics, Vols. I and II, McGraw-Hill, New York (1953).

[26] C.Kittel, "Introduction to Solid State Physics", John Wiley&Sons, NY (1976)

[27] G.D'Aguanno, N.Mattiucci, M.Centini, M. Scalora, and M. J. Bloemer, Phys. Rev. E **69**, 057601 (2004)

[28] Note that the phases of $\tilde{t}$, $t^{(+)}$ and $t^{(-)}$ are equals.

[29] F. T. Smith, *Phys. Rev.* **118,** 349-356 (1960)

[30] M. Buttiker, Phys. Rev.B **27,** 6178 (1983)

[31] G. D'Aguanno, M. Centini, M. Scalora, C. Sibilia, M.J. Bloemer, C.M. Bowden, J.W. Haus, and M. Bertolotti, *Phys. Rev. E* **63,** 36610-1-5 (2001).(and references therein)

[32] H.G. Winful , *Phys. Rev. E* **68,** 016615-1-9 (2003). (and references therein)

[33] In the optical regime ($\lambda \cong 1 \div 0.2\mu m$) for PC's of few micrometers in length $k_0 L \approx 10^2$ and the term $\frac{1}{2ck_0 L}\mathrm{Im}(r_\omega^{(+)} + r_\omega^{(-)})$ gives a correction that reaches the maximum value of the

order of *10 $^{-2}$/c* in the gap where $|r_\omega| \cong 1$. Note that the DOM of the free space (1-D) is *1/c* and the corrective term can be in most of the cases neglected.

[34] By symmetric environment we mean that the materials surrounding the structure are the same, i.e $n_{0,1}=n_{0,2}=n_0$.

[35] In Ref. [8] the DOM was defined for a structure surrounded by air ($n_0=1$) as: $\rho_\omega^U \equiv \frac{1}{2Lc}\int_0^L \left[\varepsilon_\omega^R(z)|\Phi_\omega|^2 + \frac{c^2}{\omega^2}\left|\frac{d\Phi_\omega}{dz}\right|^2 \right] dz$. ρ_ω^U was also numerically compared with ρ_ω^φ for a symmetric PC. It was found that the two definitions gave very similar results.

[36] Y.R. Shen, *The Principles of Nonlinear Optics*, (John Wiley&Sons, NY,1984).

[37] L.Brillouin, "Wave propagation and Group Velocity", Academic Press NY, 1960

[38] C.G.B. Garret and D.E. McCumber, "Propagation of a Gaussian Light Pulse through an Anomalous Dispersion Medium", *Phys Rev. A* **1,** 305 (1970)

[39] S. Chu and S. Wong, *Phys. Rev. Lett*. **48,** 738 (1982).

[40] M. Centini, M.J. Bloemer, K. Myneni, M. Scalora, C. Sibilia, M. Bertolotti, and G. D'Aguanno, *Phys. Rev. E* **68**, 016602 (2003).

I-3 THz Generation via Difference Frequency Generation in a $\chi^{(2)}$ Photonic Crystal

I-3.0 Introduction

Recently, a great deal of attention has been devoted to the problem of the generation of coherent THz radiation because of the many possible applications that have been identified: from spectroscopic imaging to radar systems, and from security and medical to biological as well as pure research purpose. Unfortunately, the number and types of THz sources available are not always adequate for all possible applications mentioned. This has led to a great deal of activity to come up with new designs and sources with different characteristics. Free-electron lasers and synchrotron radiation are powerful THz sources, but their physical size limits their application. More compact sources are based on photoconductivity (electro-optic devices) and optical rectification (all optical devices). In the first case a femtosecond laser operating in the visible or near infrared regime is used in order to create electron-hole pairs that accelerate through an appropriate electric field. The resulting changing dipole leads the generation of THz generation [1,2]. These kinds of devices are usually referred to as photoconductive antennas. In the second case, a femtosecond pulse interacts with a nonlinear crystal with a second order nonlinear susceptibility, generating a THz pulse through optical rectification [3]. Organic and inorganic electro-optic crystals like DAST, ZnTe, GaAs, $LiNbO_3$ [4,5], as well as polymers [6] have also been exploited. A wide range of techniques are currently under investigation including: quantum cascading [7], optical parametric oscillations [8], femtosecond pulse shaping [9]. Most of these sources produce THz pulses. Continuous THz sources can be obtained through difference frequency generation in second order nonlinear crystals. In this case two c.w. optical pumps interact in the crystal and generate coherent THz radiation at frequency $\Delta\omega=\omega_1-\omega_2$, where ω_1 and ω_2 are the frequencies of the pumps. For this purpose inorganic crystals like GaP [10] and GaSe [11], for example, have been used. Most recently, organic crystals (DAST) [12, 13] and EO polymer composites [14, 15] (CFAPC, DAPC, …) with large nonlinearity have been explored with promising results. Some limitations of those techniques include low tunability range, and/or low efficiency. The latter is usually due to material absorption at THz wavelengths. Typical conversion efficiencies experimentally achieved are of the order $\eta\sim10^{-6}$ [11].

We study THz emission from a $\chi^{(2)}$ –doped, one-dimensional photonic crystal (1-D PC), based on a rigorous Green function approach, and a three-dimensional vector model. THz radiation is generated via a difference-frequency generation (DFG) process, where two nearly-

degenerate optical pumps of frequencies ω_1 and ω_2 generate a frequency $\omega_3=\omega_1-\omega_2$ found in the THz range. The pumps are assumed to work in a collinear configuration. The 1-D PC structures that we study are known to exhibit some peculiar properties, such as field localization, superluminal pulse propagation in the band gap, and high density of modes, to name a few , but the structure is flexible enough that it can be optimized for various and quite different purposes, including nonlinear frequency conversion [16]. Previously, the dispersive properties of photonic band gap structures had been used to solve the phase matching problem using the optical rectification effect [17]. The use of 1-D layered structures, in order to generate submillimeter wavelengths through difference frequency generation, was already anticipated by Bloembergen and Sievers [18] in 1970. In their seminal paper, the authors discussed the properties of nonlinear optics, in particular of second order phenomena, namely second harmonic and sum/difference frequency generation in such structures. Although, Bloembergen and Sievers considered infinite structures, the results they obtained have general validity: they showed that the periodicity of the layered structure can be used to compensate the normal dispersion of materials in order to obtain high conversion efficiency through phase-matched second order interactions. On the other hand, as we will see later, in the case of finite structures the efficiency of second order interaction is not directly linked to a phase-matching term, but rather to overlap integrals of the interacting fields, as also discussed in Refs [19-20]. A first study of THz emission in 1-D PCs that used a coupled mode analysis to describe multiple field confinement, enhancement, and overlap near the photonic band edge of one-dimensional photonic band gap structures was described in reference [21]. That study, which analyzed THz emission from a defect layer, showed that it was possible, at least in principle, to obtain continuous and tunable sources from the sub-THz regime up to 12 THz. The advantages of using finite 1-D PCs in order to generate THz radiation can be found in the flexibility of those structures that allow achieving high conversion efficiency either in collinear and non collinear configuration due to high field localizations.

I-3.1 General considerations

We are studying THz generation via a second order process, which means we have two pumps and four second-order processes involved, and four generated fields. Three of those fields are generated at optical frequencies ($2\omega_1$, $2\omega_2$, $\omega_1+\omega_2$), while the fourth is generated in the THz region ($\omega_1-\omega_2$). The efficiency of optical processes is in general much greater than THz generation, and so those processes cannot be ignored. The first challenge is to inhibit any

undesired process. The transmission spectrum of a 1-D photonic crystal is characterized by wide band gaps and relatively narrow transmission peaks. Frequencies that fall inside the gap correspond to modes that are not supported by the cavity, have poor localization properties, [22], so that if a generated frequency falls inside the gap the related process is practically inhibited. The key to efficient THz generation is then to find a structure in which all the generated frequencies, except the THz, are tuned inside a transmission gap. The two optical pumps (ω_1 and

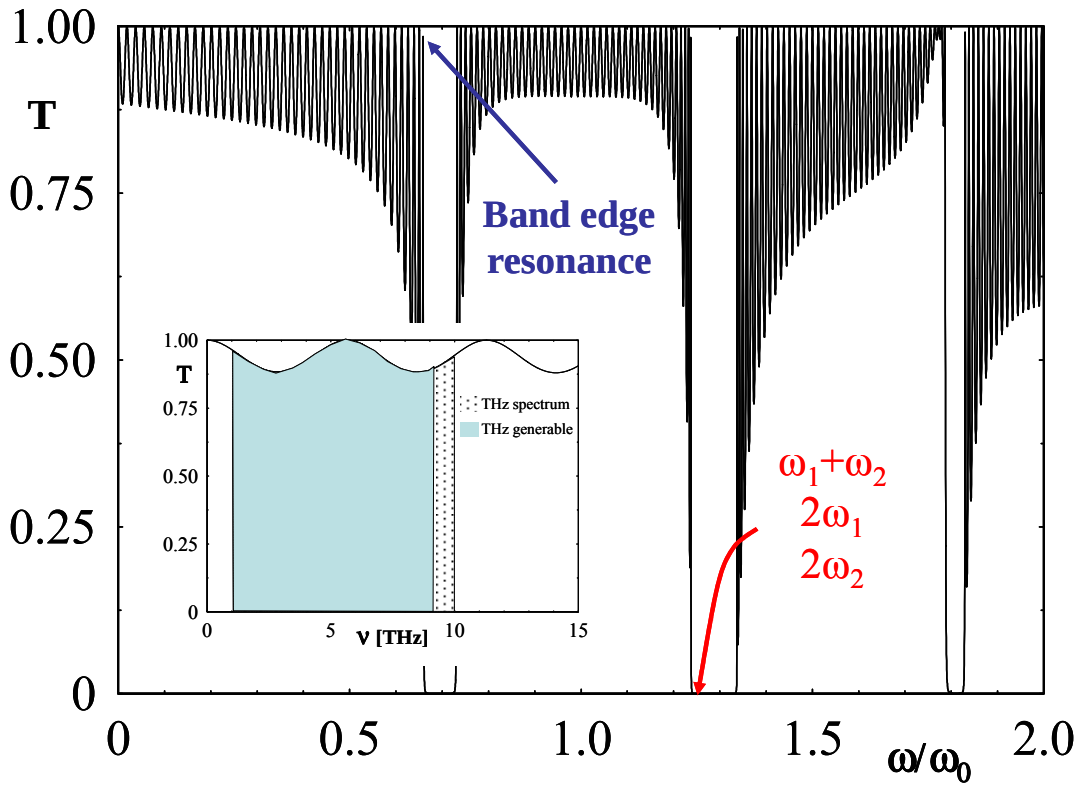

Fig. I-3. 1: Transmission spectrum of a one-dimensional periodic structure. The elementary cell is made by two layers of refractive index n_1=1.8 and n_2=1.4 at the frequency λ_0=1 μm. The lower index layer exhibits a normal dispersion. The thickness of the two layers are respectively $d_1= \lambda_0/2n_1$, $d_2= \lambda_0/4n_2$. The structure is surrounded by air (n_0=1). The transmission is a function of the normalized frequency ω/ω_0, where $\omega_0=2\pi c/\lambda_0$. In the inset is reported the spectrum of THz frequencies as a function of THz. The colored region in the inset is the part of THz spectrum for which all the undesired second order processes fall in the gap.

ω_2) are nearly degenerate ($\omega_1 \sim \omega_2 \sim \omega$); therefore, one important condition is to design a 1-D structure such that the frequency 2ω happens to fall inside a gap.

As an example, in the Fig. (I-3. 1) we show the transmittance of a 1-D structure composed of 40 periods of alternating layers (n_1~1.8, n_2~1.4) whose thicknesses are chosen to be $a=\lambda/2n_1$ and

$b=\lambda/4n_2$, respectively where λ is the reference wavelength $\lambda=1\mu m$. The high index layers are assumed to possess normal dispersion, while for simplicity the low index material is assumed to be dispersionless. Fig. (I-3. 1) thus suggests that if the pumps ω_1 and ω_2 are chosen near the first order band edge, as indicated, then the frequencies $2\omega_1$, $2\omega_2$, and $\omega_1+\omega_2$ are to be found somewhere inside the second order band gap, and their generation will be suppressed. On the other hand, the wave at the difference frequency $\omega_1-\omega_2$ (THz) will be tuned within the first pass band, away from any gap, and so it will not be inhibited.

I-3.2 Plane wave approach

In this section we follow a plane-wave approach to describe the multi-wave interaction. We deal with a six-field problem: two pumps (ω_1 and ω_2), the second harmonics (SHs) ($2\omega_1$ and $2\omega_2$), the up-converted or sum frequency (SF) ($\omega_1+\omega_2$), and the down-converted or difference frequency (DF) ($\omega_1-\omega_2$). We have to solve a system of six coupled, second order differential equations:

$$
\begin{cases}
\dfrac{d^2}{dz^2}E_{\omega_1}+\dfrac{\omega_1^{\,2}\varepsilon_{\omega_1}E_{\omega_1}}{c^2}=-2\dfrac{\omega_1^{\,2}}{c^2}\left(d^{(2)}E^*_{\omega_1}E_{2\omega_1}+d^{(2)}E^*_{\omega_2}E_{\omega_1+\omega_2}+d^{(2)}E_{\omega_2}E_{\omega_1-\omega_2}\right)\\
\dfrac{d^2}{dz^2}E_{\omega_2}+\dfrac{\omega_2^{\,2}\varepsilon_{\omega_2}E_{\omega_2}}{c^2}=-2\dfrac{\omega_2^{\,2}}{c^2}\left(d^{(2)}E^*_{\omega_2}E_{2\omega_2}+d^{(2)}E^*_{\omega_1}E_{\omega_1+\omega_2}+d^{(2)}E_{\omega_1}E^*_{\omega_1-\omega_2}\right)\\
\dfrac{d^2}{dz^2}E_{2\omega_1}+\dfrac{4\omega_1^{\,2}\varepsilon_{2\omega_1}E_{2\omega_1}}{c^2}=-4\dfrac{\omega_1^{\,2}}{c^2}\left(d^{(2)}E^2_{\omega_1}+d^{(2)}E_{\omega_1+\omega_2}E_{\omega_1-\omega_2}\right)\\
\dfrac{d^2}{dz^2}E_{2\omega_2}+\dfrac{4\omega_2^{\,2}\varepsilon_{2\omega_2}E_{2\omega_2}}{c^2}=-4\dfrac{\omega_2^{\,2}}{c^2}\left(d^{(2)}E^2_{\omega_2}+d^{(2)}E_{\omega_1+\omega_2}E^*_{\omega_1-\omega_2}\right)\\
\dfrac{d^2}{dz^2}E_{\omega_1+\omega_2}+\dfrac{(\omega_1+\omega_2)^2\varepsilon_{\omega_1+\omega_2}E_{\omega_1+\omega_2}}{c^2}=-2\dfrac{(\omega_1+\omega_2)^2}{c^2}\left(d^{(2)}E_{\omega_1}E_{\omega_2}+d^{(2)}E_{\omega_1-\omega_2}E_{2\omega_2}+d^{(2)}E^*_{\omega_1-\omega_2}E_{2\omega_1}\right)\\
\dfrac{d^2}{dz^2}E_{\omega_1-\omega_2}+\dfrac{(\omega_1+\omega_2)^2\varepsilon_{\omega_1-\omega_2}E_{\omega_1-\omega_2}}{c^2}=-2\dfrac{(\omega_1-\omega_2)^2}{c^2}\left(d^{(2)}E_{\omega_1}E^*_{\omega_2}+d^{(2)}E_{\omega_1+\omega_2}E^*_{2\omega_2}+d^{(2)}E^*_{\omega_1+\omega_2}E_{2\omega_1}\right)
\end{cases}
\qquad \text{(I-3. 1)}
$$

In the system of Eqs.(I-3. 1), $d^{(2)}$ is the nonlinear optical coefficient. It is assumed to be 100 pm/V for all processes, a practical but sensible value for many semiconductor materials.

In the un-depleted pump regime all the recombination processes can be neglected and the formal solution of system (I-3. 1) is:

$$\begin{cases} E_{\omega_1} = A_1\Phi^{+}_{\omega_1} + B_1\Phi^{-}_{\omega_1} \\ E_{\omega_2} = A_2\Phi^{+}_{\omega_2} + B_2\Phi^{-}_{\omega_2} \\ E_{2\omega_1} = -4\dfrac{\omega_1^{\,2}}{c^2}\int G_{2\omega_1}(\xi,z)d^{(2)}(\xi)E^2_{\omega_1}(\xi)d\xi \\ E_{2\omega_2} = -4\dfrac{\omega_2^{\,2}}{c^2}\int G_{2\omega_2}(\xi,z)d^{(2)}(\xi)E^2_{\omega_2}(\xi)d\xi \\ E_{\omega_1+\omega_2} = -2\dfrac{(\omega_1+\omega_2)^2}{c^2}\int G_{\omega_1+\omega_2}(\xi,z)d^{(2)}(\xi)E_{\omega_1}(\xi)E_{\omega_2}(\xi)d\xi \\ E_{\omega_1+\omega_2} = -2\dfrac{(\omega_1-\omega_2)^2}{c^2}\int G_{\omega_1-\omega_2}(\xi,z)d^{(2)}(\xi)E_{\omega_1}(\xi)E^{*}_{\omega_2}(\xi)d\xi \end{cases}, \qquad \text{(I-3. 2)}$$

where Φ_ω^+ and Φ_ω^- are the Right-to-Left (RTL) and Left-to-Right (LTR) linear propagating modes of the structure [23-24], respectively, at frequency ω, with ω=2ω$_1$, 2ω$_2$, ω$_1$+ω$_2$, ω$_1$-ω$_2$. The propagation modes are steady state waves, and in each layer they have the form of a superposition of forward and backward propagating plane waves, (the general solution of the Helmoltz equation) with suitable coefficients that can be calculated through a standard matrix transfer method [25]. Moreover, the LTR mode satisfies the boundary conditions: $1+\mathrm{r}^{\mathrm{LTR}}=\phi^{\mathrm{LTR}}(0)$, $\mathrm{i}\left(\frac{\omega}{\mathrm{c}}\right)\left(1-\mathrm{r}^{\mathrm{LTR}}\right)=\frac{\mathrm{d}}{\mathrm{dz}}\phi^{\mathrm{LTR}}(\mathrm{z})\Big|_{\mathrm{z}=0}$ and $\mathrm{t}^{\mathrm{LTR}}=\phi^{\mathrm{LTR}}(\mathrm{L})$, $\mathrm{i}\left(\frac{\omega}{\mathrm{c}}\right)\mathrm{t}^{\mathrm{LTR}}=\frac{\mathrm{d}}{\mathrm{dz}}\phi^{\mathrm{LTR}}(\mathrm{z})\Big|_{\mathrm{z}=\mathrm{L}}$, compatible with a plane wave that propagates from left to right. The RTL mode satisfies the boundary conditions: $\mathrm{t}^{\mathrm{RTL}}=\phi^{\mathrm{RTL}}(0)$, $-\mathrm{i}\left(\frac{\omega}{\mathrm{c}}\right)\mathrm{t}^{\mathrm{RTL}}=\frac{\mathrm{d}}{\mathrm{dz}}\phi^{\mathrm{RTL}}(\mathrm{z})\Big|_{\mathrm{z}=0}$ and $1+\mathrm{r}^{\mathrm{RTL}}=\phi^{\mathrm{RTL}}(\mathrm{L})$, $\mathrm{i}\left(\frac{\omega}{\mathrm{c}}\right)\left(-1+\mathrm{r}^{\mathrm{RTL}}\right)=\frac{\mathrm{d}}{\mathrm{dz}}\phi^{\mathrm{RTL}}(\mathrm{z})\Big|_{\mathrm{z}=\mathrm{L}}$ $\mathrm{i}\left(\frac{\omega}{\mathrm{c}}\right)\mathrm{t}^{\mathrm{LTR}}=\frac{\mathrm{d}}{\mathrm{dz}}\phi^{\mathrm{LTR}}(\mathrm{z})\Big|_{\mathrm{z}=\mathrm{L}}$ compatible with a plane wave that propagates from right to left. In Eq. (I-3. 2), A_1, A_2, B_1, B_2 are complex coefficients that have the dimensions of an electric field. These coefficients are uniquely determined by the boundary conditions. In the special case of LTR incidence, B_1 and B_2 are zero, while A_1 and A_2 are the magnitude of the pumps' electric fields at the first interface. On the other hand, in the case of RTL incidence, A_1 and A_2 are zero, while B_1 and B_2 are the magnitudes of the pumps' electric fields at the last interface. In this section we will study only the case of LTR incidence, so B_1 and B_2 are set to zero. In Eqs. (I-3. 2), G_ω is the Green function at frequency ω, ω=2ω$_1$, 2ω$_2$, ω$_1$+ω$_2$, ω$_1$-ω$_2$ [23-24]:

$$G_\omega(z,\xi)=\frac{1}{2ik_0 t(\omega)}\begin{cases}\Phi_\omega^-(z)\Phi_\omega^+(\xi) & 0\le z<\xi\\ \Phi_\omega^+(z)\Phi_\omega^-(\xi) & \xi<z\le L\end{cases}, \qquad \text{(I-3. 3)}$$

where $t(\omega)$ is the transmission of the structure at frequency ω.

In the plane wave regime, the conversion efficiency η of a process is defined by the ratio of the intensity of the generated wave I_g and the sum of the input pump intensities I_{pump}: $\eta=\frac{I_g}{\sum I_{pump}}$.

In this case, forward η^+ and backward η^- conversion efficiencies can be defined without ambiguity as follows: $\eta^\pm=\frac{I_g^\pm}{\sum I_{pump}}$ where $I_g^\pm$ are the intensities of the generated electromagnetic field in the forward (+) and backward (-) directions. Taking into account the relation between the intensity and the electric field for the plane waves (in complex notation) $I=\varepsilon_0 c|E|^2$ we have for the conversion efficiencies of the four generated waves:

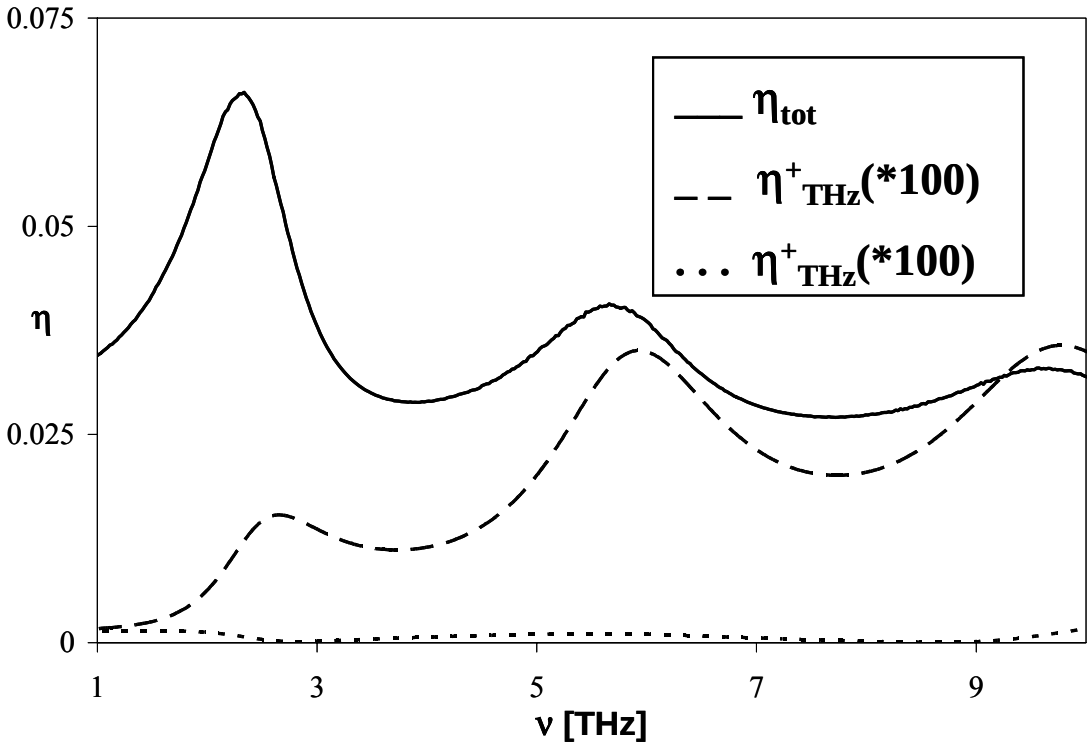

Fig. I-3. 2: Conversion efficiency vs. generated THz frequency. The full trace is the total conversion efficiency, defined as $\eta_{tot}=\eta_{2\omega1}+\eta_{2\omega2}+\eta_{\omega1+\omega2}+\eta_{\omega1-\omega2}$. The dashed trace is the forward THz conversion efficiency η^+_{THz} multiplied by 100. The small dashed line is the backward THz conversion efficiency η^-_{THz} multiplied by 100. The two pumps are arranged as shown in Fig. I-3. 3. The intensity is assumed to be 10 GW/cm^2 for both pumps.

$$
\begin{cases}
\eta^{\pm}_{2\omega_1} = \dfrac{\pi^2}{\varepsilon_0 c} d^{(2)\,2} \left(\dfrac{Q}{1+Q}\right)^2 I_{tot} \left(\dfrac{L}{\lambda_{2\omega_1}}\right)^2 \left|\dfrac{1}{L}\int_0^L \text{grating}(z)\left[\Phi^{+}_{\omega_1}(z)\right]^2 \Phi^{\mp}_{2\omega_1}(z)dz\right|^2 \\
\eta^{\pm}_{2\omega_2} = \dfrac{\pi^2}{\varepsilon_0 c} d^{(2)\,2} \left(\dfrac{1}{1+Q}\right)^2 I_{tot} \left(\dfrac{L}{\lambda_{2\omega_2}}\right)^2 \left|\dfrac{1}{L}\int_0^L \text{grating}(z)\left[\Phi^{+}_{\omega_2}(z)\right]^2 \Phi^{\mp}_{2\omega_2}(z)dz\right|^2 \\
\eta^{\pm}_{\omega_1+\omega_2} = \dfrac{4\pi^2}{\varepsilon_0 c} d^{(2)\,2} \dfrac{Q}{(1+Q)^2} I_{tot} \left(\dfrac{L}{\lambda_{\omega_1+\omega_2}}\right)^2 \left|\dfrac{1}{L}\int_0^L \text{grating}(z)\Phi^{+}_{\omega_1}(z)\Phi^{+}_{\omega_2}(z)\Phi^{\mp}_{\omega_1+\omega_2}(z)dz\right|^2 \\
\eta^{\pm}_{\omega_1-\omega_2} = \dfrac{4\pi^2}{\varepsilon_0 c} d^{(2)\,2} \dfrac{Q}{(1+Q)^2} I_{tot} \left(\dfrac{L}{\lambda_{\omega_1-\omega_2}}\right)^2 \left|\dfrac{1}{L}\int_0^L \text{grating}(z)\Phi^{+}_{\omega_1}(z)\left[\Phi^{+}_{\omega_2}(z)\right]^{*} \Phi^{\mp}_{\omega_1-\omega_2}(z)dz\right|^2
\end{cases}
$$

(I-3. 4)

Where *grating (z)* is the grating of the second order nonlinearity. I_1 is the intensity of the pump at frequency ω_1 and I_2 the intensity of the second pump, Q is the ratio I_1/I_2 and I_{tot} is the total intensity I_1+I_2.From Eq. (I-3. 4) it follows that we have the higher conversion efficiency for the

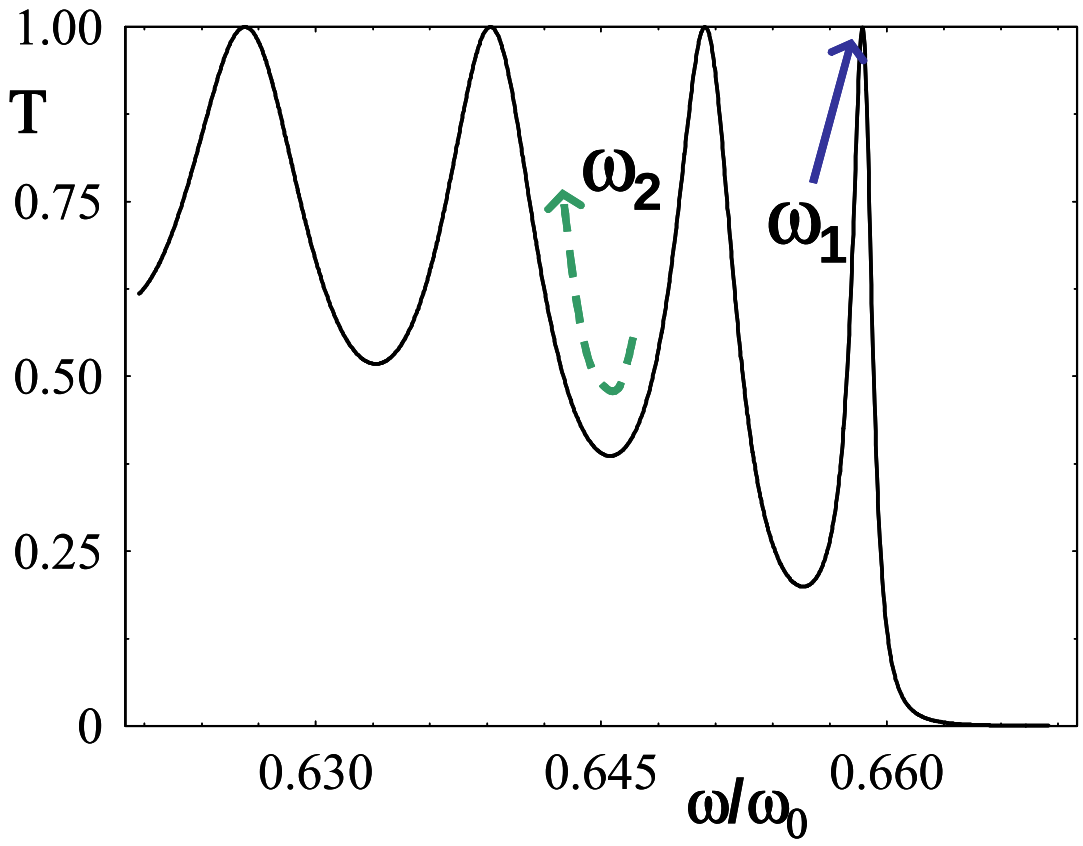

Fig. I-3. 3: Transmission spectrum as a function of the normalized frequency near the band edge. ω_1 is fixed on the band edge resonance, while ω_2 is moved back in frequency.

DF (and the SF) when the two pumps are balanced ($I_1=I_2$). So we will consider only the case $I_1=I_2$.The total conversion efficiency η_{tot} is defined as the sum of all the conversions efficiencies: $\eta_{tot}=\Sigma\eta_i$. In Fig. (I-3. 2) we report η_{tot} as a function of the generated THz radiation. The total intensity is fixed to a value of 20 GW/cm^2 (10 GW/ cm^2 for each pump). ω_1 is tuned at the band edge while ω_2 is chosen such that ($\omega_2-\omega_1$) ranges from 1 to approximately 10 THz (see Fig. (I-3. 3)) and in such a way that the second harmonic always falls inside the second order gap to

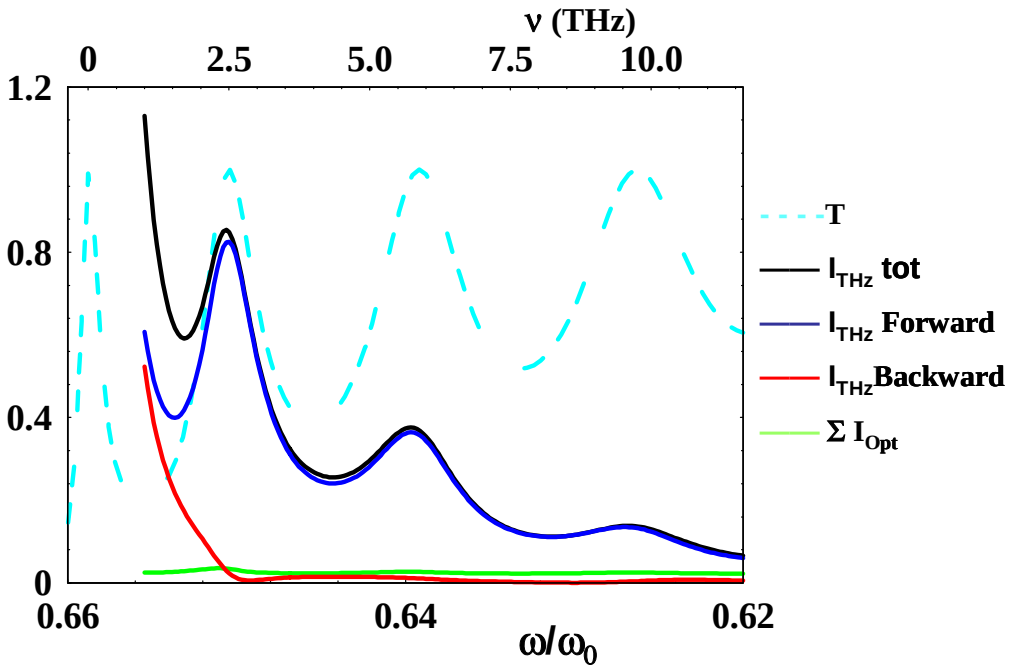

Fig. I-3. 4: Transmission and square modulus of the overlap integrals as a function of the second pump normalized frequency (lower scale) and vs. the THz generated frequency (upper scale)
The dark line is the Transmission (T), the dark dashed line is the sum of all the THz overlap integrals (I_{THz} tot), the gray line is the THz forward overlap integral (I_{THz} for), the gray dashed line is the backward overlap integral (I_{THz} back), and the gray small dashed line is the sum of the overlap integrals of all the other generated frequencies, the optical ones (ΣI_{opt}).

suppress its conversion efficiency. As shown in Fig. (I-3. 2) the un-depleted pump approximation is well verified also for the relatively intense, incident fields we are considering. The conversion efficiencies of Eq. (I-3. 4) is proportional to the product of the square of the frequency $(L/\lambda)^2$, and a term that represents the structure's properties via an overlap integral which we focus on below:

$$I^{\pm}=\left|\frac{1}{L}\int_0^L \text{grating}(z)\Phi^{+}_{\omega_1}(z)\left[\Phi^{+}_{\omega_2}(z)\right]^{*}\Phi^{\mp}_{\omega_1-\omega_2}(z)dz\right|^2 \qquad \text{(I-3. 5)}$$

In Fig. (I-3. 4) we report the behavior of the integral overlap as a function of ω_2 (lower scale) and the generated THz frequency (upper scale). We have greater total efficiency at 1 THz, when the two pumps are both tuned to the band edge resonance, and the largest forward efficiency at 2.5 THz, when the ω_2 is tuned to the second transmission resonance. This suggests that if one wishes to generate a low THz frequency (~1THz), better results can be obtained with a structure having broader resonances, such that both pumps can be tuned within the same resonance. For example, with a similar structure (25 periods instead of 40) the overlap integrals at 1 THz (and so the conversion efficiency) are nearly double. Moreover, the structure (at least for LTR incidence) will generate efficiently up to 3-4 THz, as the overlap integral becomes progressively smaller at higher frequencies.

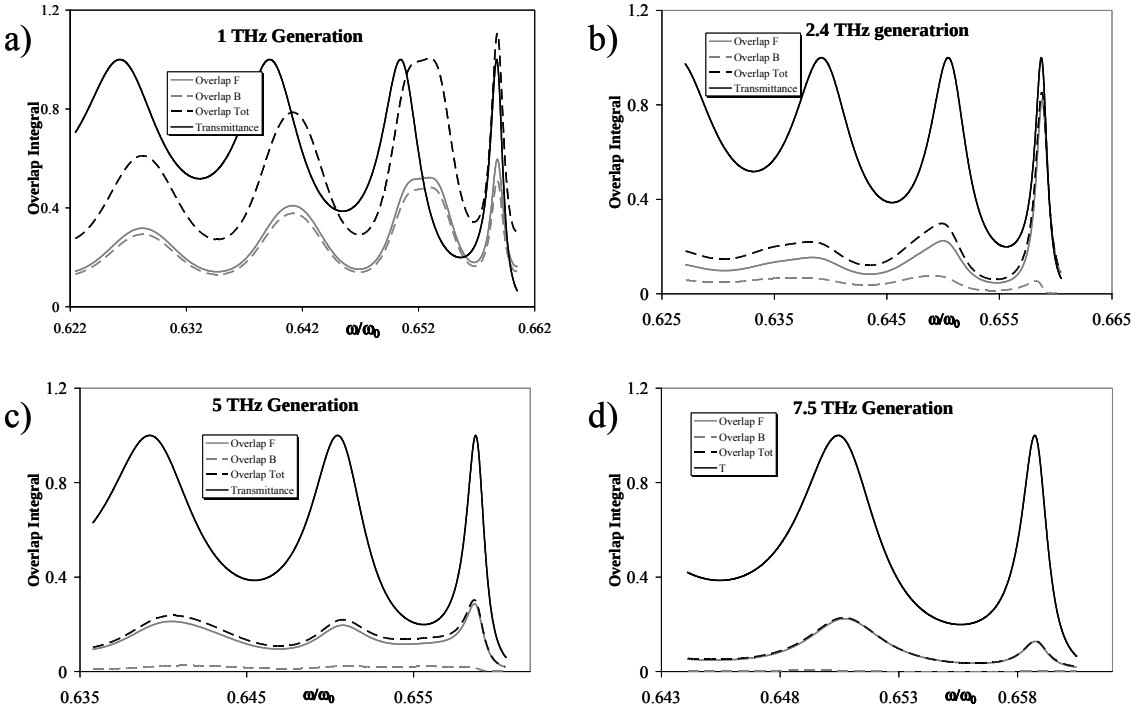

Fig. I-3. 5: Overlap integrals as functions of the normalized first pump frequency ω_1/ω_0, for four generated frequency: a) ω_1-ω_2=1THz b) ω_1-ω_2=2.4THz c) ω_1-ω_2=5THz d) ω_1-ω_2=7.5THz. The black line is the Transmission, the black dashed line is the sum of the THz overlap integrals (Overlap Tot), the gray line is the forward THz overlap integral (Overlap F), and the gray dashed line is the backward overlap integral (Overlap B).

Up to now we have used a fixed value of ω_1 to maximize its localization properties, while tuning ω_2 to lower frequencies. This may not be the best choice, but it provides a good

qualitative picture of what one may expect for structures similar to our own. If the desired outcome is a tunable device with only one tunable pump, the situation we have described is suitable. In Fig. (I-3. 5) we show what happens to the overlap integrals if we tune ω_1 away from the band edge, for the generation of 1, 2.4, 5 and 7 THz. The result is that only for the highest frequency (7.5 THz) the chosen configuration is not ideal. The plane waves approach offers a complete description for all the optical frequencies because it allows the calculation of the conversion efficiency as long as the spatial properties of the emitted fields are those of plane waves. In fact, this model offers only partial information on THz emission in that while it allows a correct estimation of the conversion efficiency, diffraction of the generated THz waves is not taken into account, and we have little or no information on the spatial distribution of the radiation. This aspect of THz generation will be discussed in the next section with the help of a three dimensional model.

I-3.3 Three dimensional approach

In this section we develop a three dimensional model to simulate the spatial characteristic of THz generation. The THz signal is generated from the interaction of two optical pumps in a volume that can be approximated with a cylinder of radius R (equal to the pumps spot size) and length equal to the length of the 1-D PC structure (See Fig. (I-3. 6)). As explained in the previous

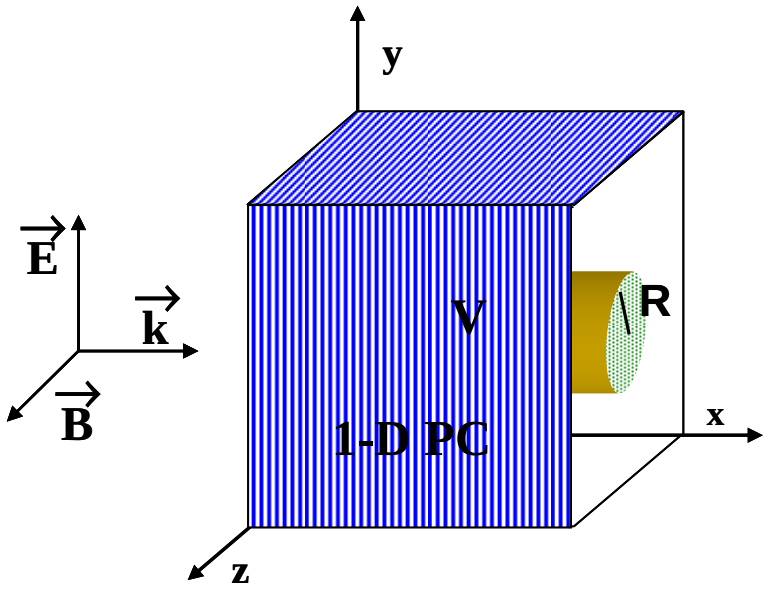

Fig. I-3. 6: Configuration of the three-dimensional simulations. The pumps enter the structure at normal incidence; the interactive area is a cylinder of radius R equal to the spot size and length L equal to the PC length.

section, we can neglect all the recombination terms. The THz field, according to Maxwell's equations, satisfies the vectorial equation:

$$\nabla x\nabla xE - \omega^2\mu_0\hat{\varepsilon}E = 2\varepsilon_0 \overset{=(2)}{d} : E_1E_2^* \qquad \text{(I-3. 6)}$$

Equation (I-3. 6) has the formal solution:

$$E = \mu_0\omega^2 \int_V dV'\hat{G}(r,r')2\varepsilon_0 \overset{=(2)}{d} : E_1E_2^* \qquad \text{(I-3. 7)}$$

where $\hat{G}(r,r')$ is the dyadic Green function of the problem; $\overset{=(2)}{d}$ is the nonlinear tensor; E_1 and E_2 are the pump fields. Without lack of generality we will study the configuration $E_1//E_2//P^{NL}$. As the THz wave-length is much greater compared to the length of the structure, the structure itself may be considered a point source of THz radiation. In Eq. (I-3. 7) we can use the free space dyadic Green function [26].In the far field approximation, the dyadic Green function reduces to the simple form [27]:

$$G_{ij}(r,r') = (\delta_{ij} - x_i x_j)\frac{1}{4\pi r^3}\exp(ik_0 r)\exp\left(-ik_0\frac{r\cdot r'}{r}\right), \qquad \text{(I-3. 8)}$$

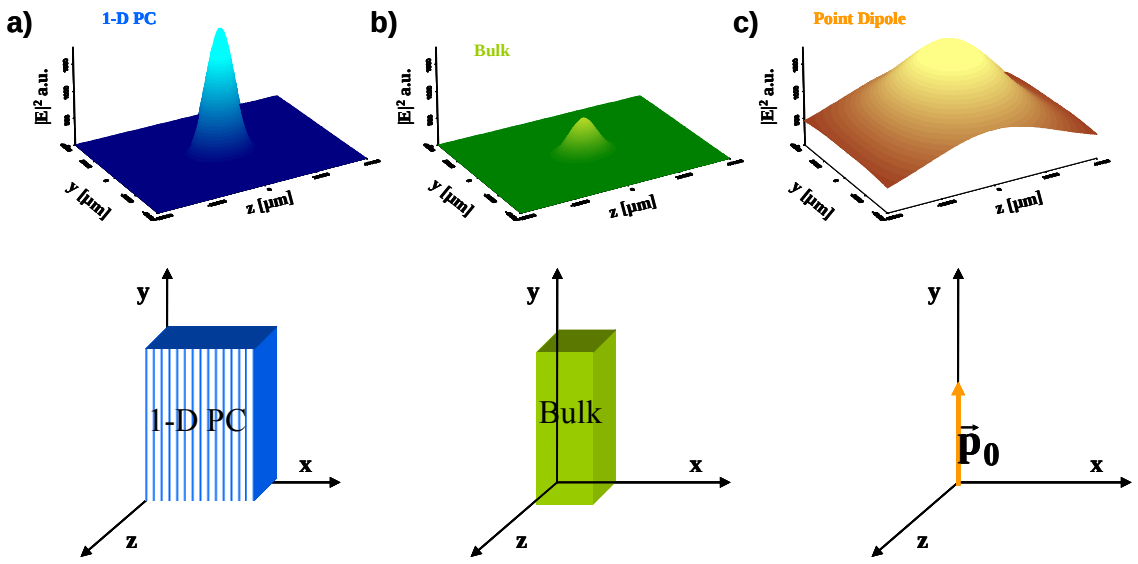

Fig I-3. 7: Spatial distribution of THz emission a) from a 1-D PC, b) from an equivalent bulk, c) from a point dipole.

Assuming a plane wave form for the pump fields from Eqs.(I-3. 6&7), we arrive at the following expression for the electric field:

$$\mathbf{E} = \mu_0 \varepsilon_0 \omega^2 d^{(2)} A_1 A_2^* \exp(ik_0 r)\exp(i\omega t)\frac{R}{k_0 \rho} J_1\left(\frac{k_0 \rho R}{r}\right) I_x \begin{pmatrix} -\frac{xy}{r^2} \\ 1-\frac{y^2}{r^2} \\ -\frac{yz}{r^2} \end{pmatrix} \qquad \text{(I-3. 9)}$$

where $I_x = \int_0^L dx' \exp\left(-ik_0 \frac{x\,x'}{r}\right) \Phi_1^+(x') \Phi_2^+(x')^* \text{grating}(x')$; J_1 is the Bessel function of order 1; $\rho^2 = y^2 + z^2$; A_1 and A_2 are the amplitude of the pump fields $\mathbf{E_1}$ and $\mathbf{E_2}$.

From Eq. (I-3. 9) the square modulus of the electric field and the Poynting vector (**S**) can easily be calculated. The intensity of the electromagnetic field is given by the modulus of the Poynting vector. It comes out that the emission is directional, namely: the intensity of the electromagnetic field is largest near the x axis and the direction of the Poynting vector is nearly along the x axis.

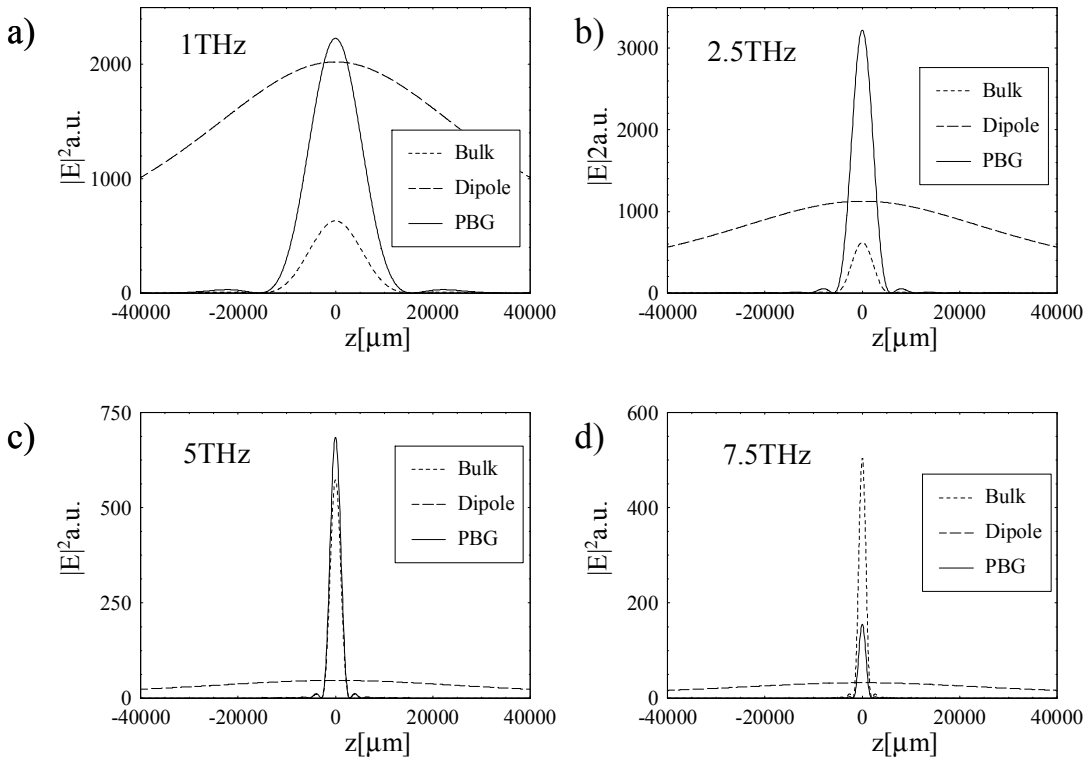

Fig. I-3. 8: Square modulus of the electric field, at a plane parallel to the yz plane, distant 4 cm from the source, in the forward direction as a function of the z coordinate. The full line is the photonic crystal emission, the dashed line is the equivalent dipole emission and the small dashed line is the equivalent bulk emission. In the case of: a) ω_1-ω_2=1 THz b) ω_1-ω_2=2.5 THz c) ω_1-ω_2=5 THz d) ω_1-ω_2=7.5 THz.

Moreover, even if the emission is not in the form of a plane wave we have that $|\mathbf{S}| \propto \mathbf{E}\cdot\mathbf{E}'$.

The THz emission obtained pumping the 1-D PC structure may be compared with the emission obtained from an equivalent bulk and that of an equivalent dipole. In Fig (I-3. 7) we show the spatial emission for both: 1-D PC, bulk and equivalent dipole emissions at 1THz. Moreover in Fig (I-3. 8) we plot the emission for the generation of 1, 2.5, 5 and 7.5 THz.

The equivalent bulk is composed of a non-linear material of length L1 equal to the sum of all the non-linear layers in the 1-D PC structure. The emission from that structure is found following the model developed by Shen [27].

The equivalent dipole is a point dipole of intensity given by the sum of all the dipole distributed in the 1-D PC structure. Although the point dipole is an idealization, comparing this case with the 1-D PC and the bulk shows that the 1-D PC and the bulk have a much more directional emission. That directionality is due to the fact that in both cases the dipoles are excited by highly directional optical pumps. As predicted by the plane wave approach, the emission from the 1-D PC structure can be much higher than the emission from the bulk. In particular, at 1 and 2.5THz, Figs. (I-3. 8a) and (I-3. 8b), we have an enhancement of nearly 6 with respect to the bulk. At 5 THz (Fig. (I-3. 8c)) the emission from the 1-D PC and from the bulk are nearly equal. At 7.5 THz (Fig. (I-3. 8d)) there is no advantage in using the 1-D PC.

To evaluate the conversion efficiency we calculate the flux of the Poynting vector through a close surface and divide it by the flux of the pumps through the input surface S (a circle of radius R). For example, we can enclose the source in a cylinder of radius a, and length 2d, where d>>L (far field approximation). In that case we have:

$$\eta = \frac{\int_0^a d\rho\,\rho \int_0^{2\pi} d\varphi S_x(d,\rho,\varphi) - \int_0^a d\rho\,\rho \int_0^{2\pi} d\varphi S_x(-d,\rho,\varphi) + a\int_{-d}^{d} dx' \int_0^{2\pi} d\varphi\left[S_y(x',a,\varphi)\cos\varphi + S_z(x',a,\varphi)\sin\varphi\right]}{\pi R^2 \varepsilon_0 c\left(A_1^2 + A_2^2\right)}. \qquad \text{(I-3. 10)}$$

Note that the Poynting vector goes to zero far from the x axis. So if in Eq. (I-3. 10) the radius a is taken large enough to contain the peak of the emission, we identify three contributions to the conversion efficiency: forward (η^+), backward (η^-) and lateral (η^{lat}) conversion efficiency, as follows:

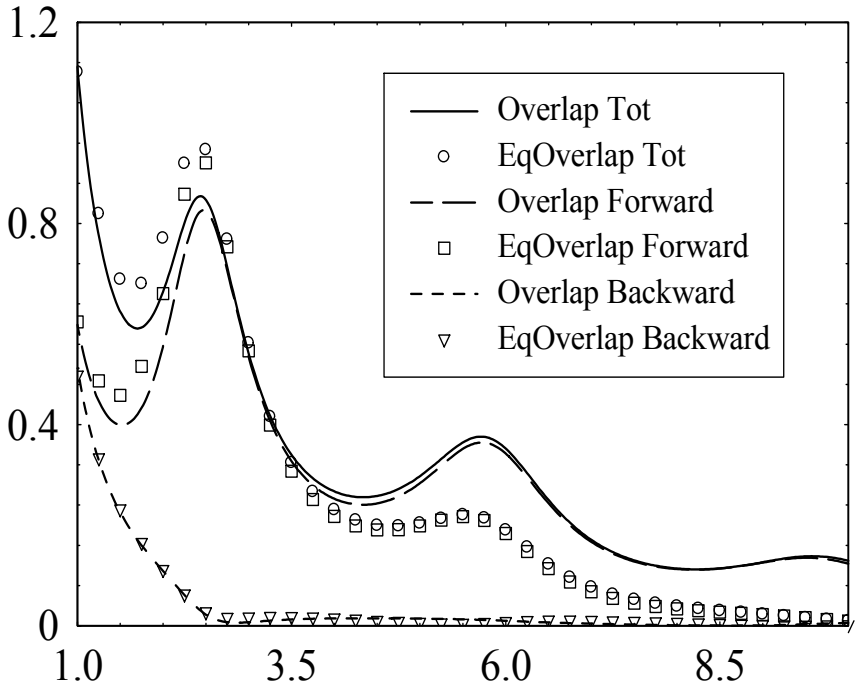

Fig. I-3. 9: Overlap integrals (lines) and their equivalent for the 3-D model (points) as functions of the generated THz frequency. The full line and the circles are for the total (sum of the forward and backward) overlaps (Overlap Tot and EqOverlap Tot), the dashed line and square are for the forward overlaps (Overlap forward and EqOverlap forward), while the small dashed line and the triangle are for the backward overlaps (Overlap backward and EqOverlap backward).

$$\begin{cases} \eta^{+} = \dfrac{\int_0^a d\rho\,\rho \int_0^{2\pi} d\varphi S_x(d,\rho,\varphi)}{\pi R^2 \varepsilon_0 c\left(A_1^2 + A_2^2\right)} \\ \eta^{-} = \dfrac{-\int_0^a d\rho\,\rho \int_0^{2\pi} d\varphi S_x(-d,\rho,\varphi)}{\pi R^2 \varepsilon_0 c\left(A_1^2 + A_2^2\right)} \\ \eta^{lat} = \dfrac{a\int_{-d}^{d} dx' \int_0^{2\pi} d\varphi\left[S_y(x',a,\varphi)\cos\varphi + S_z(x',a,\varphi)\sin\varphi\right]}{\pi R^2 \varepsilon_0 c\left(A_1^2 + A_2^2\right)} \end{cases} . \qquad \text{(I-3. 11)}$$

The forward and the backward conversion efficiency are proportional to the flux of the Poynting vector through the basis of the cylinder. The lateral conversion efficiency is proportional to the flux of the Poynting vector through the lateral surface of the cylinder.

It turns out that the emission through the lateral surface is negligible with respect to the emission through the basis of the cylinder. Expression (11) can be recast in the following form:

$$\begin{cases} \eta^{+} = \dfrac{4\pi^2}{\varepsilon_0 c} d^{(2)2} \dfrac{Q}{(1+Q)^2} I_{tot} \left(\dfrac{L}{\lambda}\right)^2 I_{eq}^{+} \\ \eta^{-} = \dfrac{4\pi^2}{\varepsilon_0 c} d^{(2)2} \dfrac{Q}{(1+Q)^2} I_{tot} \left(\dfrac{L}{\lambda}\right)^2 I_{eq}^{-} \end{cases} . \qquad \text{(I-3. 12)}$$

with:

$$\begin{cases} I_{eq}^{+} = \dfrac{1}{\pi L^2} \int_S \dfrac{1}{y^2+z^2} \dfrac{1}{r^4} (J_1)^2 \left[ra(a^2+z^2) |I_x|^2 + z^2 r \, \mathrm{Re}\left(I_x L_x^{*}\right) \right] ds \\ I_{eq}^{-} = \dfrac{-1}{\pi L^2} \int_S \dfrac{1}{y^2+z^2} \dfrac{1}{r^4} (J_1)^2 \left[-ra(a^2+z^2) |I_x|^2 + z^2 r \, \mathrm{Re}\left(I_x L_x^{*}\right) \right] ds \end{cases} \qquad \text{(I-3. 13)}$$

In Eq. (I-3. 13) $L_x = \int_0^L dx' x' \exp\left(-i k_0 \dfrac{x\,x'}{r}\right) \Phi_1^{+}(x') \Phi_2^{+}(x')^{*} \, \mathrm{grating}(x')$. The a-dimensional quantities I_{eq}^{+} and I_{eq}^{-} play in the conversion efficiency of the three dimensional model the same role as the overlap integrals defined in Eq. (I-3. 5).

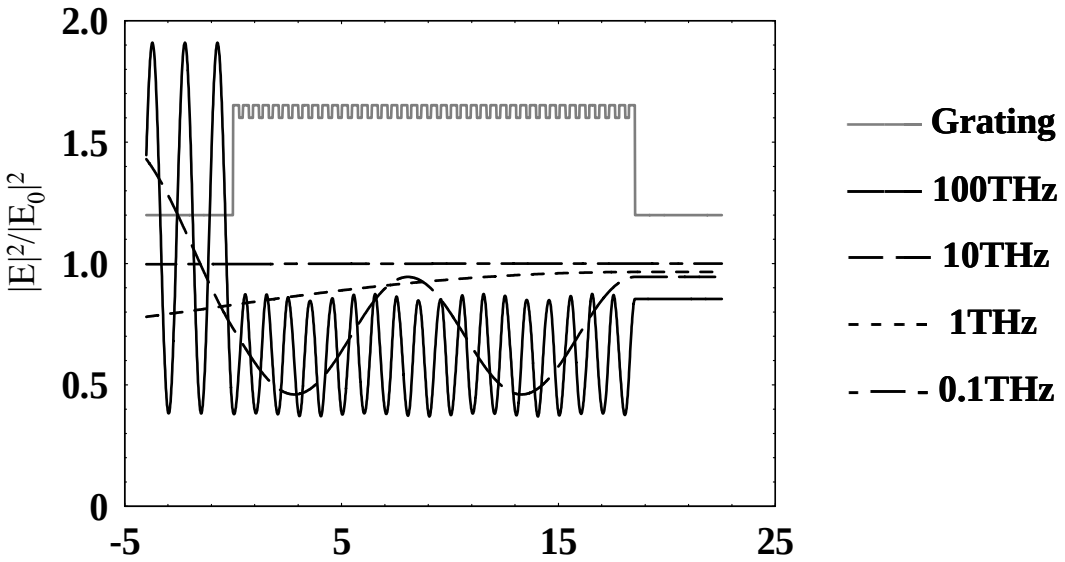

Fig. I-3. 10: Field localization as a function of the propagation coordinate x, for several incidence frequencies ν, in the plane wave approximation. Full line ν=100THz, dashed line ν=10THz, small dashed line ν=1THz, dashed-point line ν=0.1THz. The gray line is the refractive index grating of the structure.

In Fig. (I-3. 9) we compare the behavior of the overlap integrals in the two models. While the two models have the same qualitative behavior, there are some quantitative differences due to

the fact that on one hand the 3-D model neglects the internal details of the structure for the THz frequency, while on the other hand, the 1-D model neglects the 3-D aspect of the emission. The localization of the field grows with frequency, while the emission spread goes in the other direction. So moving to higher frequencies the field localization becomes dominant and the 1-D model makes more accurate predictions, while moving to lower frequencies it is the 3-D model that becomes more accurate. THz frequencies lie in the transition region between those two regimes. In Fig. (I-3. 10) we plot the field localization (the square modulus of the 1-D PC modes) moving from the microwaves to the far infrared. If there is no localization we will have a constant value 1, otherwise we will see oscillations end maybe high localization zones. It is clear that from this point of view THz frequencies represent a transition region. Even if we do not have strong field localization, one cannot assume that THz radiation does not feel the structure.

I-3.4 Four gate system

As shown by Centini et al [28] the use of the 1-D PC structure as a four gate system, namely pumping the structure from both sides, modifies the field distribution of the pumps inside the structure. This effect allows us to change the conversion efficiency [28] and the ratio of the forward and backward emission by changing the phase difference between the RTL and LTR input fields. The overlap integrals (Eqs. (I-3. 5) and (I-3. 13)) become functions of the phase differences $\Delta\varphi 1$ and $\Delta\varphi 2$ between the RTL and LTR incident fields at frequencies $\omega 1$ and $\omega 2$, respectively. In particular pumping from both sides makes it possible to control: (a) field localization in the active layers; and (b) the amount of relative forward and backward THz emission. In order to take advantage of effect (a) we need the pumps to be tuned at the transmission peaks near the band edge, where the field is most intense. In order to take advantage of effect (b) we need the LTR and RTL modes of the generated frequency to have different localization properties.

In Fig. (I-3. 11) we report field localization of the structure's modes (LTR and RTL) for 1, 2.5, 5, and 7.5 THz. At 1THz the field does not feel the structure: there is no field localization and the LTR and RTL are practically the same and flat. In this case we may not change the balance of the forward and backward emission. Moreover, the two pumps are tuned at the band edge, and we expect to have higher conversion efficiency. At 2.5THz LTR and RTL mode localization is sensibly different. We expect to be able to change the balance of the forward and backward emission in an equally sensible way. As only one pump is tuned at the band edge, we

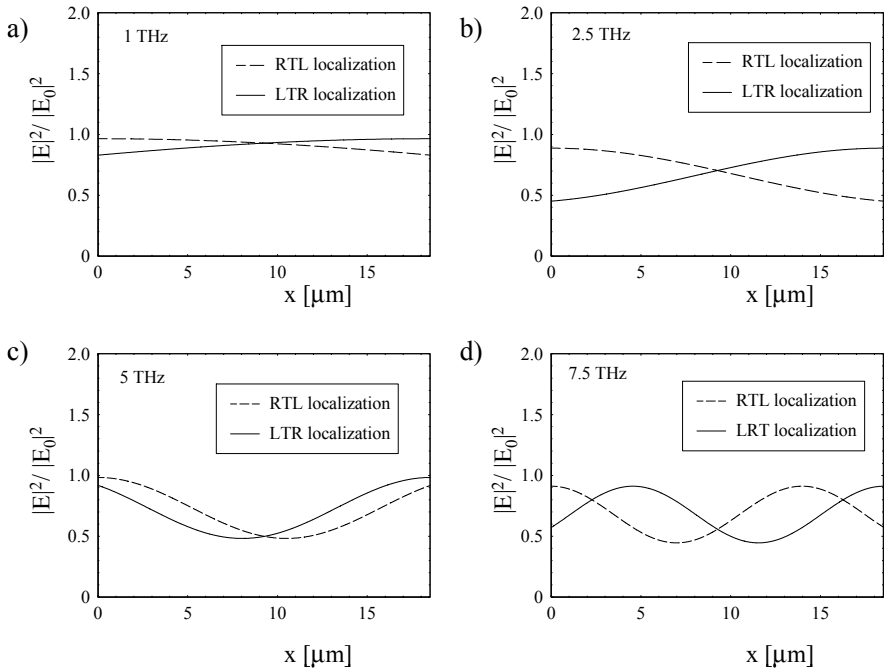

Fig. I-3. 11: Field localization as a function of the propagation coordinate x, in the case of LTR incidence (full line) and RTL incidence (dashed line). The frequency ν is a) 1THz b) 2.5THz c) 5THz d) 7.5 THz.

do not expect to fully exploit field localization effects. At 5 and 7.5 THz we still have that the LTR and RTL modes localized differently and so we can partially control the directionality of the emission. But the efficiency of the process will not be as high as also having the second pump tuned far from the band edge.

In the conversion efficiencies formulas, in the case of LTR+RTL incidence, the only factors that change are the overlap integrals, Eq. (I-3. 5), and the corresponding quantity in the 3D model, Eq. (I-3. 13). In Eqs (I-3. 5) and (I-3. 13) $\Phi^{+}_{\omega_1}(z)$ must be replaced by $\Phi^{+}_{\omega_1}(z)+\Phi^{-}_{\omega_1}(z)\exp(i\Delta\varphi_1)$ while, $\Phi^{+}_{-\omega_2}(z)$ must be changed to $\Phi^{+}_{-\omega_2}(z)+\Phi^{-}_{-\omega_2}(z)\exp(i\Delta\varphi_2)$. Because in case of symmetric or nearly symmetric structures, we have that $\phi^{+}_{\omega}(z)\approx\phi^{-}_{\omega}(L-z)$, the following condition is satisfied: $I^{-}(-\Delta\varphi_1,-\Delta\varphi_2)=I^{+}(\Delta\varphi_1,\Delta\varphi_2)$

This means that if the behavior of the forward overlap integral is known, then the backward overlap integral is also known. The phase differences Δφ1 and Δφ2 can be chosen (at each frequency) in order to maximize the total conversion efficiency (η^{+}+η^{-}), namely the sum of the forward and backward overlap integrals, as well as the forward or the backward conversion efficiency.

In Fig. (I-3. 12) we show what happens when $\Delta\varphi 1$ and $\Delta\varphi 2$ are chosen in order to maximize the total conversion efficiency. Note $\Delta\varphi 1$ and $\Delta\varphi 2$ have a different value for each frequency. The forward and the backward overlap integrals, as well as the sum of the two, are plotted as functions of the generated THz frequency. Comparing the behavior of the total overlap integral with the case of LTR incidence (Fig. (I-3. 9)), we find an enhancement factor of nearly 4 at 1 THz, which translates to an enhancement factor of nearly 20 with respect to the bulk. Moreover, the four gate system is always more efficient than the one sided incidence, but any significant advantage quickly goes away as the second pump moves away from the band edge, and the generated frequency increases. The maximum efficiency is reached almost always when the forward and the backward emissions are nearly equal. The 3-D and the 1-D models show some quantitative differences for reasons that were discussed earlier. In Fig. (I-3. 13) we show what happens when $\Delta\varphi 1$ and $\Delta\varphi 2$ are chosen in order to maximize the forward conversion efficiency. According to Fig. (I-3. 11), near 1 THz, we cannot control the direction of the emission. In that case forward and backward emissions are similar. As one moves to higher frequencies, control of the directionality of the emission increases, and the efficiency drops.

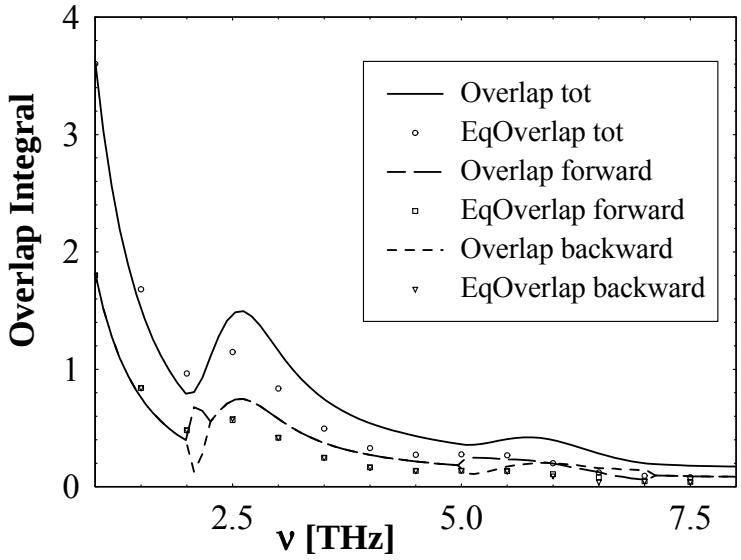

Fig. I-3. 12: Overlap integral (lines) and its equivalent for the 3-D model (points) in the case of both sides incidence. For both pumps, the phase difference between the LTR and RTL beam is chosen in order to maximize the total conversion efficiency. The full line and the circles are for the total overlaps; the dashed line and the squares are for the forward overlaps; the small dashed line and the triangles are for the backward overlaps.

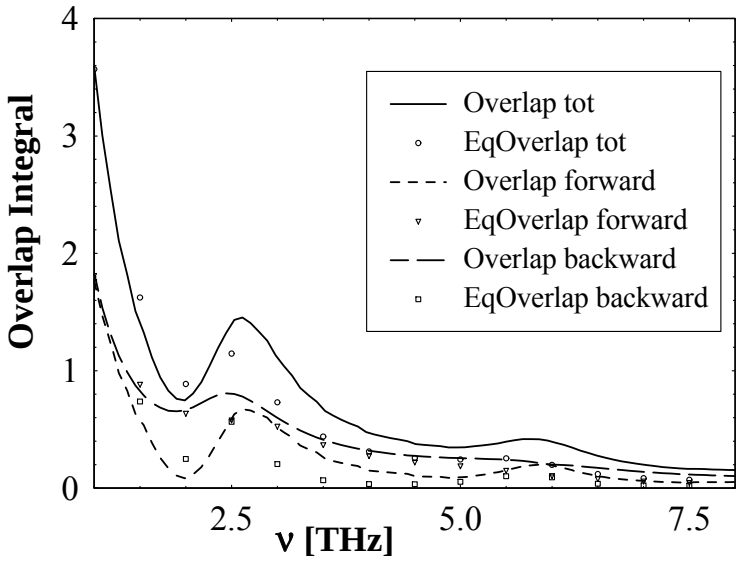

Fig. I-3. 13: Overlap integral (lines) and its equivalent for the 3-D model (points) in the case of both sides incidence. For both pumps, the phase difference between the LTR and RTL beam is chosen in order to maximize the forward conversion efficiency. The full line and the circles are for the total overlaps; the dashed line and the squares are for the forward overlaps; the small dashed line and the triangles are for the backward overlaps.

Conclusions

We have developed a 3-D model able to simulate THz emission from a PC structure via difference frequency generation. The model allows the calculation of the conversion efficiency as well as the spatial properties of the emission. This model also shows that 1-D PC structures are versatile and powerful devices, able to efficiently generate THz frequencies. The general analysis on THz emission in PC structure carried out in this work is a useful overview that will allow us to properly design structures for specific purposes.

In this paper we have not referred to any particular material, and so our results have general validity, thanks in part to the fact that 1-D PCs with similar characteristics can be obtained adjusting the number of periods and/or the index contrast. A structure with low index contrast and large number of periods behaves like a structure with a high index contrast and fewer periods. Moreover, we stress that not all materials suitable for stratification have been characterized in the THz regime, and at the present time, the best candidate for nonlinear material appears to be GaAs, which has already been used to generate THz pulses via optical rectification [5].

References:

[1] N.M. Froberg, B.B. Hu, Xi-Cheng Zhang, and D.H. Auston, IEEE J. of Quantum Elec. **28**, 2291 (1992).

[2] Y.C. Shen, P.C. Upadhya, E.H. Linfield, H.E. Beere, Phys. Rev. E **69**, 235325-1 (2004).

[3] L. Xu, X.-C. Zhang, and D.H. Auston, Appl. Phys Lett. **61**, 1784 (1992).

[4] K. H. Yang, P. L. Richards, and Y. R. Shen, Appl. Phys. Lett. **19**, 320 (1971).

[5] A.S. Nikoghosyan, E.M. Laziev, R. M. Martirosyan, and A.A. Hakhoumian**,** Proc. SPIE Int. Soc. Opt. Eng. **4752**, 40 (2002).

[6] A. Nahata, D. H. Auston, C. Wu, J.T. Yardley, Appl. Phys. Lett. **67**, 1358 (1995).

[7] Tredicucci, F. Capasso, G. Gmachi, D. L. Sivco, A.L. Hutchinson, A.Y. Chao, Appl. Phys. Lett. **73**, 2101 (1998).

[8] M.A. Piestrup, R.N. Fleming, Appl. Phys. Lett. **26**, 418 (1975).

[9] A.M. Weiner and D.E. Leaird, Opt. Lett. **15**, 51 (1990).

[10] T.Taniuchi, H. Nakanishi, Elect. Lett. **40**, 327 (2004).

[11] W. Shi, Y.J. Ding, Appl. Phys. Lett. **84**, 1635 (2004).

[12] Taniuchi, H. Adachi, S. Okda, T. Sasaki, and H. Nakanishi, Elect. Lett. **40**, 549 (2004).

[13] P.E. Powers, R.A. Alkuwari, J.W. Haus, K. Suizu, H.Ito, Opt. Lett. **30**, 640 (2005).

[14] A.M. Sinyukov, M.R. Leahy, L.M. Hayden, M. Haller, J. Luo, A. K-Y. Jen, L.R. Dalton, Appl. Phys. Lett. **85**, 5827 (2004)

[15] X.Zheng, A.M. Sinyukov, L.M. Hayden, Appl. Phys. Lett **87**, 081115

[16] . M.Bertolotti, C.M. Bowden, C. Sibilia Eds. "Nanoscale Linear and nonlinear optics", AIP Conference Procedings vol. 560, New York, (2001).

[17] Yan-quing Lu, Min Xiao, Gregory J. Salamo, J. of Quantum Electronics 38, 481-485 (2002).

[18] N. Bloembergen and A.J. Siever, Appl. Phys. Lett. **17**, 483 (1970).

[19] G. D'Aguanno, M. Centini, M. Scalora,C. Sibilia, M. Bertolotti, M. J. Bloemer, C. M. Bowden, J. Opt. Soc. Am. B **19**, 2111 (2002).

[20] M. Centini, G. D'Aguanno, C. Sibilia, L. Sciscione, M. Bertolotti, M. Scalora, M. J, Bloemer, Opt. Lett. **29**, 1924 (2004).

[21] J.W. Haus, P.Powers, M. Torres-Cisneros, M. Scalora, M.J. Bloemer, N. Akozbek, and M.A. Meneses-Nava, Las. Phys. **14**, 635-642 (2004).

[22] G. D'Aguanno, M. Centini, M. Scalora, C. Sibilia, M. J. Bloemer, C. M. Bowden, J. W. Haus, and M. Bertolotti," Phys. Rev. E **63**, 036610 (2001).

[23] O.Di Stefano, S. Savasta, and R. Girlanda, J.Mod.Opt **48**, 67-84 (2001).

[24] G. D'Aguanno, N. Mattiucci, M. Scalora, M. J. Bloemer, and A. M. Zheltikov, Phys. Rev. E **70**, 016612 (2004).

[25] J. Lekner, "Theory of reflection", Martin Nijhoff Publishers Dordrecht (1987), Chapter 12.

[26] W.C. Chew, Van Nostrand Reinhold "Waves and fields in inhomogeneous media," New York 1990, pp. 375-378.

[27] Y.R. Shen, "The principle of nonlinear optics" John Wiley & Sons New York 1984, pp. 110-113.

[28] M. Centini, G. D'Aguanno, M. Scalora, M. J. Bloemer, C. M. Bowden, C. Sibilia, N. Mattiucci, and M. Bertolotti, Phys Rev E **67**, 036617 (2003)

I-4 Cross phase modulation effects in a $\chi^{(3)}$ photonic crystals: applications to all-optical switching devices

I-4.0 Introduction

We present a numerical study of a finite photonic band gap structure with a $\chi^{(3)}$ nonlinearity that couples two input pump beams at frequencies ω_1 and ω_2. We show that in this configuration a variety of all-optical devices can be obtained: an optical transistor, a double switch, and a dynamical switch. The seminal work of Chen and Mills [1] on the appearance of gap solitons in one-dimensional photonic crystals (1-D PCs) with a $\chi^{(3)}$ nonlinearity can be characterized as the beginning of a period of intense experimental and theoretical investigations whose focus was to study the possibility of using these structures as all optical devices: as switching and limiting devices, and as diodes [2-8]. Although a large number of papers have already been published on the subject, the vast majority of them generally consider configurations with only one input pump beam, limiting the flexibility of the proposed devices. In reference [8] a more flexible configuration was studied, but the proposed device is an electro-optic rather than an all-optical device. Here we study an all-optical device based on a two-pump scheme, where the two pumps are coupled by the cross phase modulation terms of the cubic nonlinearity. In particular, we will discuss an optical transistor, a double switch, and a dynamical switch.

I-4.1 The model.

Our study is based on the plane monochromatic wave approach. Two input beams, of frequencies ω_1 and ω_2 respectively, propagate in the z direction and arrive at normal incidence at the input surface of a 1-D PC composed of alternating layers of a linear dielectric material juxtaposed to a non linear dielectric material with a cubic nonlinearity. The two waves are assumed to be linearly polarized in the same direction. The problem can be described by the following system of nonlinear coupled differential equations:

$$\begin{cases} \dfrac{d^2E_1}{dz^2} + \dfrac{\omega_1^2}{c^2}\left[n_1(z) + 3\sigma_{11}(z)\left|E_1\right|^2 + 6\sigma_{21}(z)\left|E_2\right|^2\right]E_1 = 0 \\ \dfrac{d^2E_2}{dz^2} + \dfrac{\omega_2^2}{c^2}\left[n_2(z) + 3\sigma_{22}(z)\left|E_2\right|^2 + 6\sigma_{12}(z)\left|E_1\right|^2\right]E_2 = 0 \end{cases}, \qquad \text{(I-4. 1)}$$

where, E_1 and E_2 are the amplitudes of the electric fields, normalized with respect to the input amplitudes, at frequency ω_1 and ω_2 respectively. The dimension-less coefficients σs are the elements of the $\chi^{(3)}$ tensor multiplied the square modulus of the related input amplitudes (i.e.

$\sigma_{ij}=\chi^{(3)}(\omega_j;\omega_j,\omega_i,-\omega_i)|E_i^{(0)}|^2)$. For simplicity, we assume that the $\chi^{(3)}$ tensor is not dispersive, so that $\sigma_{11}=\sigma_{12}=\sigma_1$ and $\sigma_{21}=\sigma_{22}=\sigma_2$. n_1 and n_2 are the z-dependent, linear refractive indexes, at frequencies ω_1 and ω_2 respectively. We consider a 1-D PC composed of *N=40* periods, and we assume that the elementary cell is made of two layers of non-dispersive and non-absorbing dielectric materials of low refractive index $n_L=1.7$ $\lambda/4n_L$ thick, and high refractive index $n_H=3.5$ $\lambda/2n_H$ thick, respectively. The reference wavelength is $\lambda=1\mu m$. The low index layer exhibits the $\chi^{(3)}$ nonlinearity.

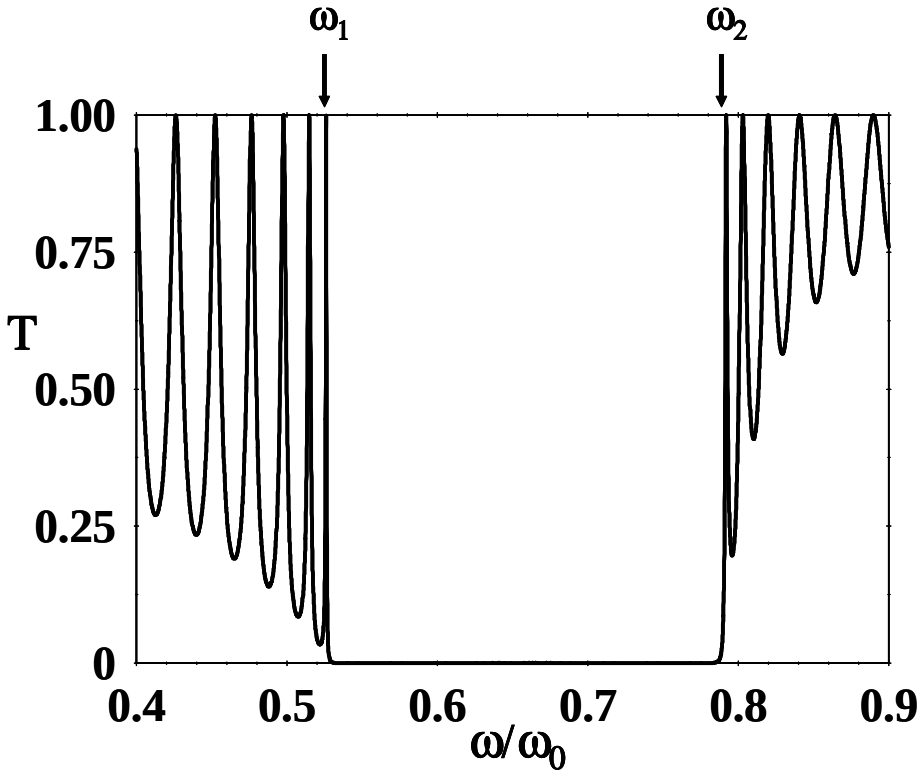

Fig. I-4 1: Linear transmission vs. ω/ω_0 where $\lambda_0=1\mu m$ is the reference wavelength and $\omega_0=2\pi c/\lambda_0$. The structure is composed of N=40 periods. The elementary cell consists of two layers of refractive index $n_H=3.5$ and $n_L=1.7$, respectively. The thickness of the two layers are respectively $d_H=\lambda_0/2n_H$, $d_L=\lambda_0/4n_L$. The structure is surrounded by air ($n_0=1$). The arrows indicate the position of the two pumps (ω_1 and ω_2) on the transmission spectrum.

In Fig. (I-4.1) we show the linear transmission of the structure (T). The arrows indicate the tuning of the two incident pumps. The ω_1 pump is tuned at the low frequency band edge transmission resonance, while the ω_2 pump is tuned at high frequency band edge transmission resonance. In both cases T~1. We note that this structure was not optimized for the devices that will be studied in the next Sections. And so we seek proof-of-principle results and an

understanding of the qualitative aspects of the dynamics that ensues when two pumps are coupled as in Eq.(I-4. 1) above. Moreover, although in our calculations we use a λ/4-λ/2 structure; similar results can be expected for different types of structures. We numerically integrate Eq.(I-4. 1) using a shooting procedure, as described in references [9-10], for example.

I-4.2 Optical Transistor and double switch.

In electronics, a transistor is made of three layers of a doped semiconductor material. The three-layer structure consists of an N-type (P-type) semiconductor layer sandwiched between two P-type (N-type) layers. In such a device a small change in the current or voltage at the inner semiconductor layer, which acts as control, produces a large change in the current passing through the entire structure. The device can thus act as a switch, opening and closing an electronic gate. From this point of view, the optical configuration we propose shows transistor like behavior (see Fig. 1-4.2).

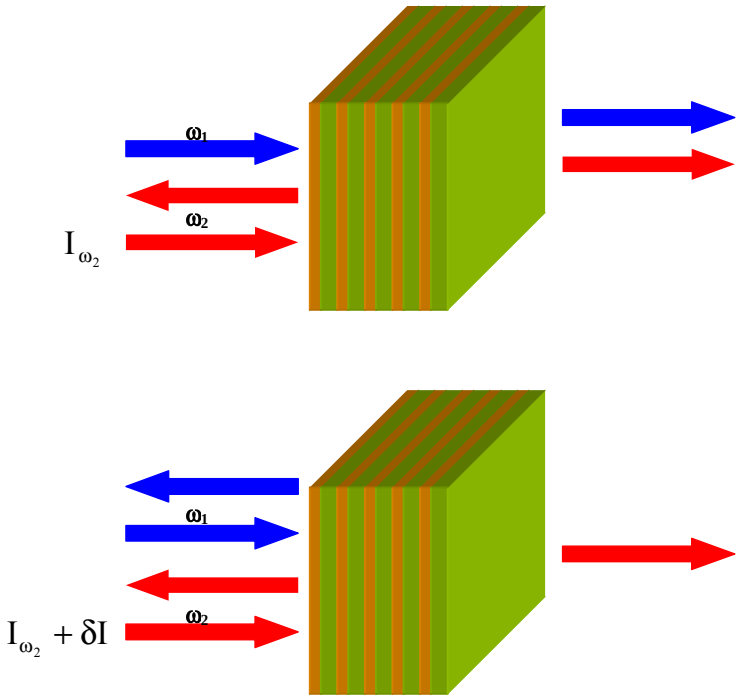

Fig. I-4. 2: Schematic drawing of our optical transistor. A small change in the intensity of the ω_2 field induces a large change in the transmission of the ω_1 field.

In Fig. (I-4. 3) we show that a small change in the intensity of the ω_2 pump produce a large change in the transmitted intensity of the ω_1 field (dashed line), a behavior that is due to the

optical bistability induced by the ω_2 pump. In fact, if we turn off the electric field E_2 and allow the intensity of the ω_1 pump to vary, no bistable behavior is noted. (Fig. (I-4. 3)-solid line).

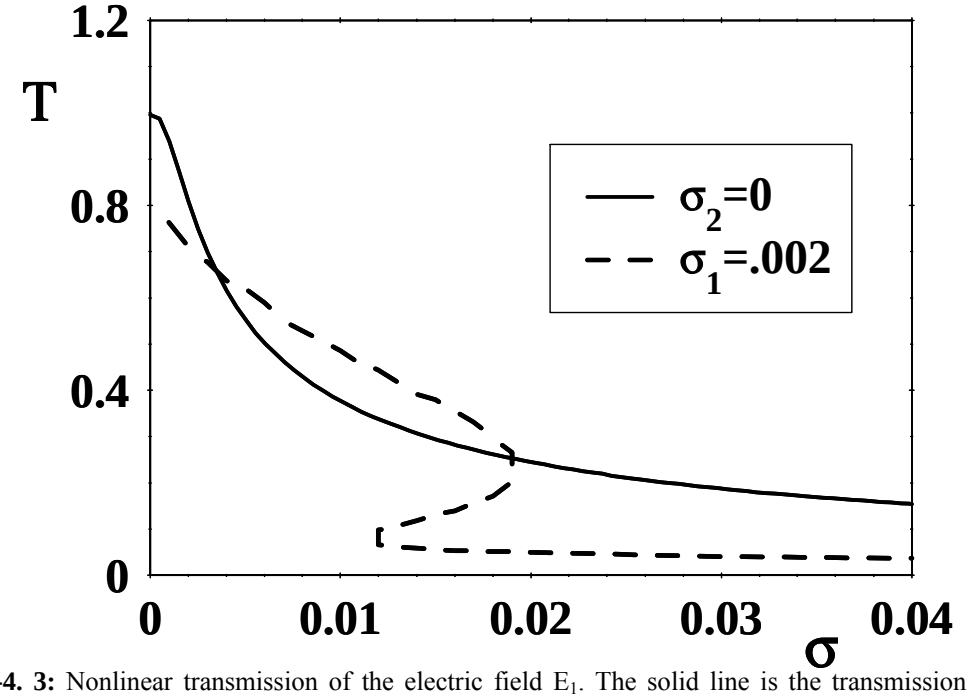

Fig. I-4. 3: Nonlinear transmission of the electric field E_1. The solid line is the transmission of the electric field E_1 as a function of its own control parameter $\sigma_1=\chi^{(3)}|E_1^{(0)}|^2$(the second pump ω_2 is in this case turned off: i.e. $\sigma_2=0$). $E_j^{(0)}$ with j=1,2 are the amplitudes of the input fields at frequency ω_1 and ω_2 respectively. The dashed line is the transmission of the electric field E_1 as a function of the control parameter $\sigma_2=\chi^{(3)}|E_2^{(0)}|^2$ (the first pump ω_1 is in this case set at a fixed value: $\sigma_1=0.002$). In the first case (solid line) in the abscise axis σ stays for σ_1 while in the second case (dashed line) σ stays for σ_2.

The ω_2 pump also manifests bistable behavior, as shown in Fig. (I-4. 4). The device can then be used as a double switch, as the switching point of the transmitted fields at ω_1 and ω_2 is the same for both curves. In Figs. (I-4. 5) and (I-4. 6) we show the square modules of E_1 and E_2, respectively, inside the PC before the switch (thin solid line), when $\sigma_1=0.002$ and $\sigma_2=0.002$, and after the switch (thick solid line), when $\sigma_1=0.002$ and $\sigma_2=0.03$. Note that for $\sigma_1=0.002$ the nonlinear transmission for ω_1 is T~0.75, and E_1 has the characteristic bell-shaped envelope consistent with its tuning very near the peak of transmission of the low frequency band edge [11], close to its original tuning position. This clearly indicates that the transmission resonance for the ω_1 pump has suffered a small, nonlinear shift toward low frequencies. On the other hand, for the same control parameter (i.e. $\sigma_2=\sigma_1=0.002$), the high frequency band edge transmission resonance has already suffered a large shift toward low frequencies causing the E_2 field to "fall"

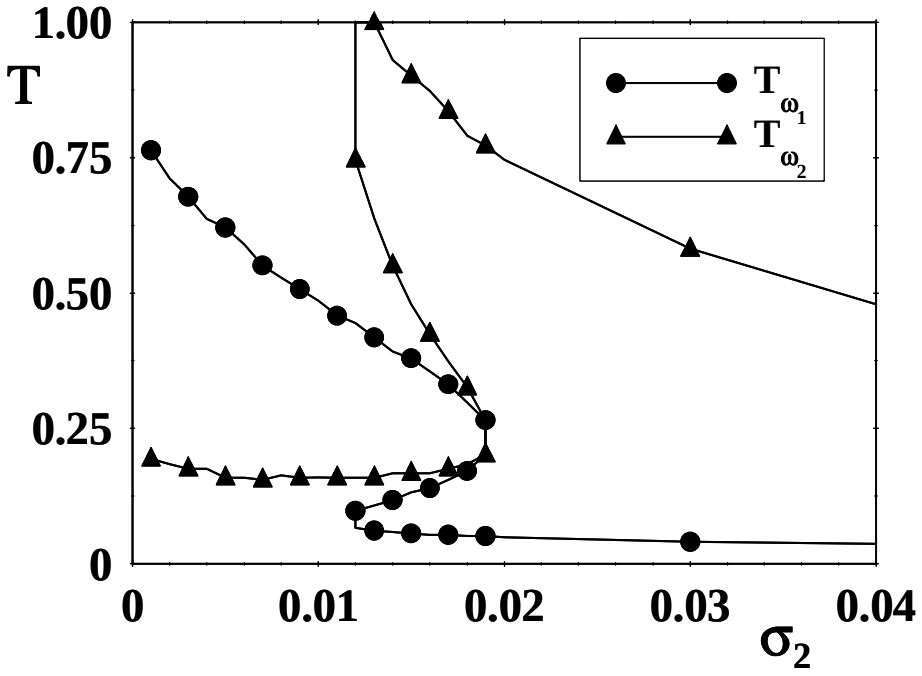

Fig. I-4. 4: Transmission of the electric fields E_1 and E_2 vs. σ_2. The control parameter of the first pump is set at σ_1=0.002.

in the valley between the first and the second transmission resonances, at the high frequency band edge, with T~0.25. The different behavior of the two fields can be easily explained because of their different localization properties within the PC: E_1 is initially mostly localized on the linear, high-index layers, while E_2 is initially localized in the nonlinear, low-index, layers. After switching occurs, the nonlinear shift of the transmission cause the E_1 field to fall inside the gap, near the low frequency band edge. The E_2 field is then tuned near the second peak of transmission of the high frequency band edge, consistent with its double-bell shaped envelope.

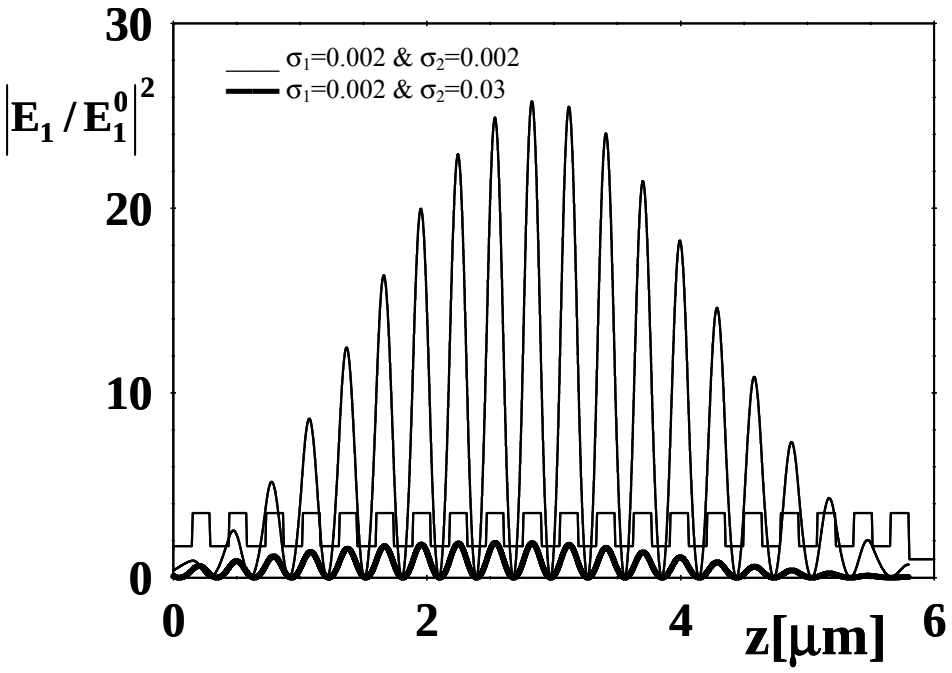

Fig. I-4. 5: Square modulus of $E_1/E_1^{(0)}$ inside the structure. The solid line represents the field profile after the switching (σ_1=0.002 and σ_2=0.03). The dashed line represents the profile of the field before the switching (σ_1=0.002 and σ_2=0.002).

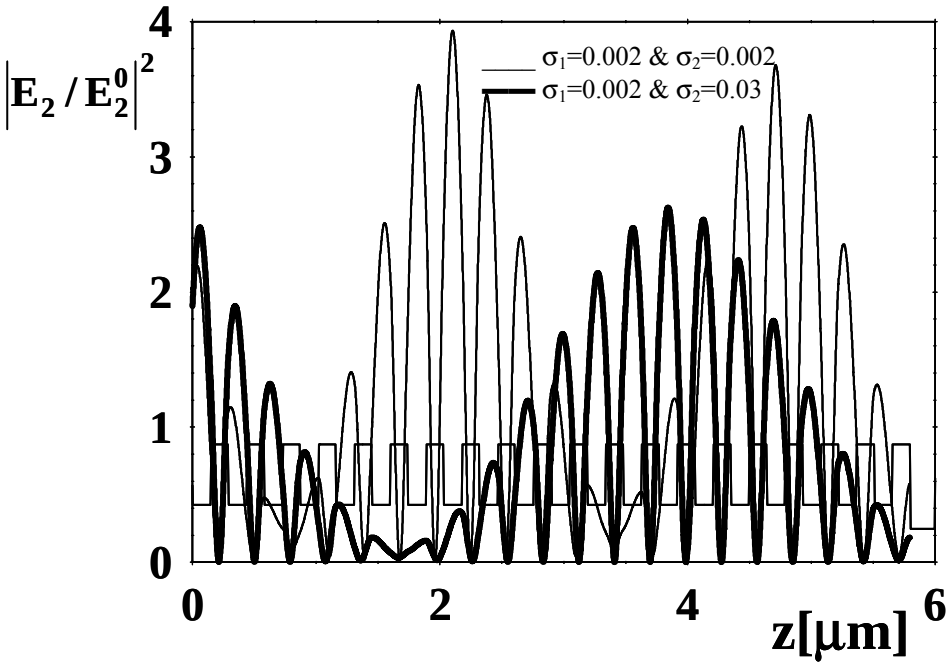

Fig. !-4. 6: Square modulus of $E_2/E_2^{(0)}$ inside the structure after the switching (solid line) for σ_1=0.002 and σ_2=0.03 and before the switching (dashed line) for σ_1=0.002 and σ_2=0.002.

I-4.3 Dynamical switch.

A simple all-optical switch in PC structures with a cubic nonlinearity has been studied in Refs.[3-4]. In the present case, our device can benefit from additional flexibility by dynamically (or parametrically) controlling the switching point of the E_2 field using the intensity of the E_1 field. In other words, we fix the intensity of the E_1 input field, vary the intensity of the E_2 field, and so monitor the change of the switching point of the E_2 field for different values of the E_1 intensity. In Fig.(I-4. 7) we calculate the nonlinear transmission curves of the E_2 field vs. σ_2 for different values of the parameter σ_1 (σ_1=0; 0.004; 0.008). The figure shows that the switching point is reached for lower values of σ_2 as σ_1 increases. In other words, the larger the intensity of the ω_1 pump is, the lower the intensity of the ω_2 pump will be to achieve self-switching. In Fig.(I-4. 8) we show the variation of the switching point (σ_{2s}) as a function of the σ_1 parameter. Note that while for low values of σ_1 the curve is linear, for higher values of σ_1 the curve show saturating behavior.

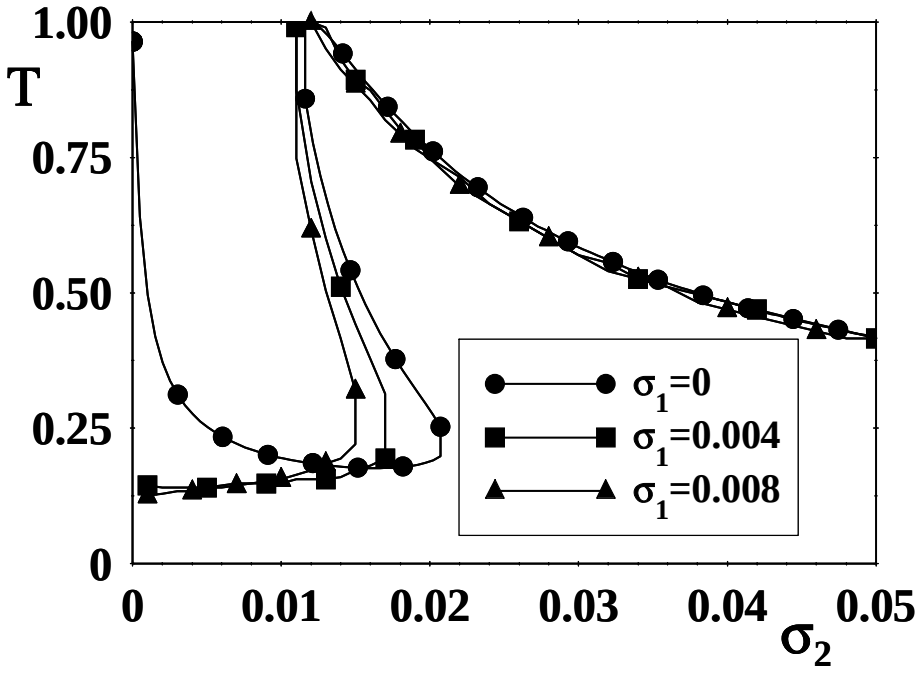

Fig. I-4. 7: Transmission of the electric field E_2 vs. σ_2, for different values of the control parameter σ_1.

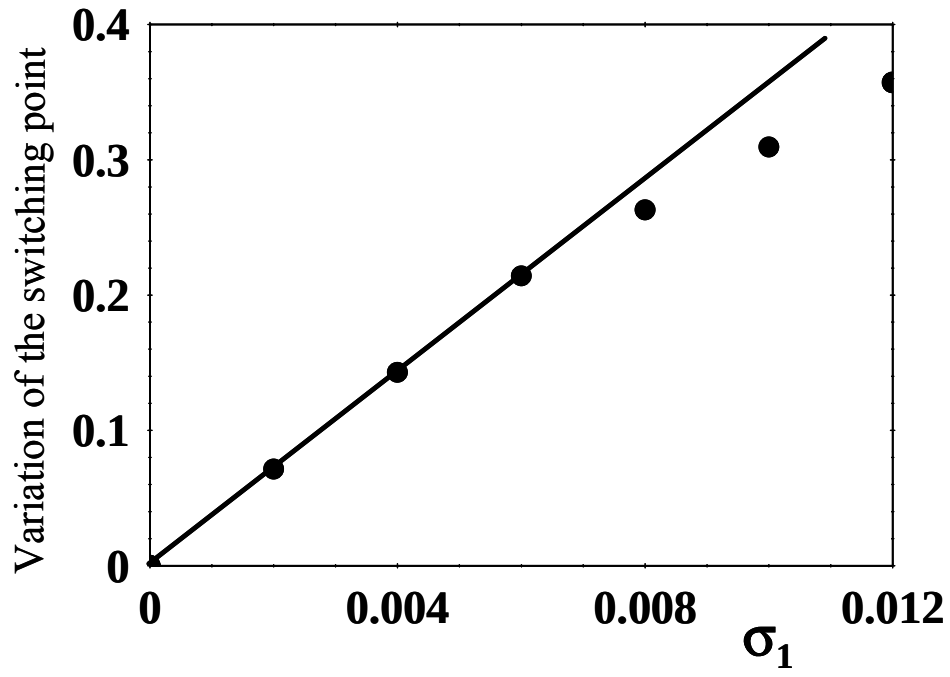

Fig. I-4 8: Variation of the switching point of the E_2 field vs.σ_1. The switching point is indicated as σ_{2s} and the relative variation of the switching point is calculated as follows:

$$(\sigma_{2s}(\sigma_1=0)-\sigma_{2s}(\sigma_1))/\sigma_{2s}(\sigma_1=0).$$

The circles represent the actual data calculated. The straight, solid line connecting the first points indicates that the variation of the switching point is linear only for small values of the control parameter σ_1. In this case saturation effects come into play above σ_1~0.006.

Conclusions.

In summary, we have shown that a 1-D PC doped with a $\chi^{(3)}$ nonlinearity, and pumped with two electromagnetic fields, can act as a more versatile device compared to having just a single pump. The switching properties of the structure [3, 4 and 7] can be improved by using a double pumping scheme such that both pumps are tuned their respective band edges, and become localized inside the stack. The dynamics that ensues, gives rise to a double switch (Fig. (I-4. 4)), and to a dynamical switch (Fig. (I-4. 7)). An all-optical transistor (Figs. (I-4. 2) and (I-4. 3)) is also envisioned.

References

[1] W. Chen, D.L.Mills: Phys. Rev. Lett. **58**, 160 (1987)

[2] J. He, M. Cada: Appl. Phys. Lett. **61**, 2150 (1992)

[3] B. Acklin, M. Cada, J. He, M.-A. Dupertuis: Appl. Phys. Lett. **63**, 2177 (1993)

[4] M. Scalora, J.P. Dowling, C.M.Bowden, M.J. Bloemer: Phys. Rev. Lett. **73**, 1368 (1994)

[5] M. Scalora, J.P. Dowling, C.M.Bowden, M.J. Bloemer: J. Appl. Phys. **76**, 2023 (1994)

[6] M.D. Tocci, M.J. Bloemer, M. Scalora, J.P. Dowling, C.M.Bowden: Appl. Phys. Lett. **66**, 2324 (1995)

[7] S. Janz, J. He, Z.R. Wasilewski, M. Cada: Appl. Phys. Lett. **67**, 1051 (1995)

[8] P. Xie and Z-Q. Zhang: J. Appl. Phys. **95**, 1630 (2004)

[9] R.S.Bennink, Y-K. Yoon, R.W. Boyd, J.E. Sipe Opt. Lett. **24**, 1416 (1999)

[10] W.H. Press, B.P. Flannery, S.A. Teukolsky, and W.T. Vetterling, *Numerical Recipes in C,* (Cambridge Univ. Press, Cambridge,1988)

[11] G. D'Aguanno, M. Centini, M. Scalora, C. Sibilia, Y. Dumeige, P. Vidakovic, J.A. Levenson, M.J. Bloemer, C.M. Bowden, J.W. Haus, and M. Bertolotti, *Phys.l Rev. E* **64,** 16609 (2001)

Part II:

“Negative index materials.”

II-1 Introduction

II-1.1 Historical background

When both the electric susceptibility ε and the magnetic permeability μ are simultaneously negative, the index of refraction $n=\pm\sqrt{\varepsilon\mu}$ admits the negative root as a possible solution, leading to negative refraction of the incident beam, among other things. Those features had been first pointed out in 1968 by V. G. Veselago in his paper: "The electrodynamics of substance with simultaneous negative values of ε and μ" [1]. That paper remained forgotten for more than thirty years, until recently in 2000 Pendry [2] conjectured that a material with the properties just described may be used to construct a "perfect" lens, i.e. a lens that can focus all Fourier components of a 2D image, even those that do not propagate in a radiative manner. Although some aspects of the "superlensing" effect are still under debate, the work of Pendry has nevertheless paved the way to an intense, sometimes quite passionate, investigation on the possibility of creating new artificial materials with simultaneous negative ε and μ and low absorption that could match the properties of the material envisioned by Veselago more than 30 years before.

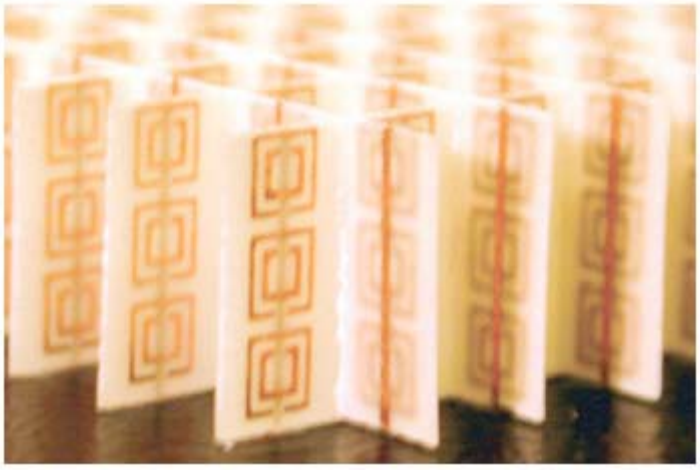

Fig.II-1. 1: Left-Handed Material (LHM) or Negative Index Material (NIM)sample. The LHM sample consists of square copper split ring resonators and copper wire strips on fiber glass circuit board material . Photo taken from Ref.[3]

In 2001 Shelby, Smith and Schultz published the result of their experimental work [3] in which they demonstrated negative refraction, in the microwaves regime, from a material made by a two dimensional array of repeated unit cells of copper strips and split-ring resonators (see Fig.II-1 1). Nowadays these substances are sometimes referred to as negative index materials (NIMs), or left handed materials (LHMs). A large number of papers have been published on the subject just in the last few years and a review can be found in Ref.[4].

II-1.2 Basic properties

The refractive index *n* and the extinction coefficient β of a material are found by solving the following complex, algebraic equation:

$$\hat{n}^2 = \varepsilon\mu \qquad \text{(II-1.1)}$$

where $\hat{n} = n + i\beta$ is the complex refractive index, ε and μ are the frequency dependent, complex, electric susceptibility and magnetic permeability functions of the medium, respectively. In general, in the case of a passive medium the law of increase of entropy determines that *Im(ε)* and *Im(μ)*, which are linked to the electric and magnetic losses respectively, *are always positive.* Moreover, to the extent that every non-steady process is thermodynamically irreversible, *Im(ε) and Im(μ) are not exactly zero for any frequency other than zero* [5]. These considerations lead to the condition that the damping term β *must be always positive* for a wave propagating in the positive direction and also that β *is never exactly zero*. Physically, this means that, slight as it may be, there is always some damping of the electromagnetic wave during its propagation. Now, by equating the real and imaginary parts of the right hand and left hand sides of Eq.(1), and by solving the corresponding system of algebraic equations with the condition β>0, we find the expressions for the refractive index and the extinction coefficient as follows:

$$n = \frac{\mathrm{Im}(\varepsilon\mu)}{\sqrt{2}\sqrt{-\mathrm{Re}(\varepsilon\mu) + \sqrt{[\mathrm{Re}(\varepsilon\mu)]^2 + [\mathrm{Im}(\varepsilon\mu)]^2}}}, \qquad \text{(II-1. 2a)}$$

$$\beta = \frac{\sqrt{-\mathrm{Re}(\varepsilon\mu) + \sqrt{[\mathrm{Re}(\varepsilon\mu)]^2 + [\mathrm{Im}(\varepsilon\mu)]^2}}}{\sqrt{2}}. \qquad \text{(II-1. 2b)}$$

We note that Eqs.(2) are valid in general for any kind of passive medium, and we also note that that the sign of *n* depends on the sign of the quantity $Im(\varepsilon\mu)=Re(\varepsilon)Im(\mu)+Re(\mu)Im(\varepsilon)$. Now, for a passive medium $Im(\varepsilon)$ and $Im(\mu)$ must be positive and therefore it is straightforward to verify that when $Re(\varepsilon)$ and $Re(\mu)$ are simultaneously negative the refractive index *n* given by Eq.(II-1 2a) is also negative [6].In the limit of negligible losses (i.e. $\mathrm{Im}(\varepsilon)\to 0$ and $\mathrm{Im}(\mu)\to 0$), from Eqs.(II-1) we have that:

$$\begin{aligned}
&\text{for } \mathrm{Re}(\varepsilon)>0 \text{ and } \mathrm{Re}(\mu)>0 \begin{cases} \beta \to 0 \\ n \to \sqrt{\mathrm{Re}(\varepsilon)\,\mathrm{Re}(\mu)} \end{cases} \\
&\text{for } \mathrm{Re}(\varepsilon)<0 \text{ and } \mathrm{Re}(\mu)<0 \begin{cases} \beta \to 0 \\ n \to -\sqrt{\mathrm{Re}(\varepsilon)\,\mathrm{Re}(\mu)} \end{cases} . \qquad \text{(II-} \\
&\text{for } \mathrm{Re}(\varepsilon)<0 \text{ and } \mathrm{Re}(\mu)>0 \\
&\text{or } \mathrm{Re}(\varepsilon)>0 \text{ and } \mathrm{Re}(\mu)<0 \begin{cases} \beta \to \sqrt{\left|\mathrm{Re}(\varepsilon)\,\mathrm{Re}(\mu)\right|} \\ n \to 0 \end{cases}
\end{aligned}$$

1.3)Therefore, we can distinguish three different regimes: a) positive index regime, where n is positive and β is negligible; b) negative index regime, where n is negative and β is negligible; c) transient or zero-n regime where n is zero and β is significantly different from zero. Let us now consider a plane monochromatic wave incident at the plane boundary between two generic materials. The incident wave gives raise to a reflected and to a transmitted wave. The time averaged Poynting vector ($\vec{S}=\frac{1}{2}\mathrm{Re}[\vec{E}\times\vec{H}^{*}]$) for the transmitted wave can be written both in the positive and in the negative index regime as:

$$\vec{S}=\frac{c^{2}|E|^{2}}{4\pi\omega\mu}\vec{k}_{t}, \qquad \text{(II-1. 4)}$$

where $\vec{k}_t$ is the k-vector of the transmitted wave, and it must be consistent with the Snell law. Moreover, causality requires that the direction of the Poynting vector of the transmitted field (i.e. the energy flow in the refracting material) always point away from the source towards the refracting material itself.

The Snell's law states that, for monochromatic, plane-waves "any boundary condition that relates the incident, the reflected and the transmitted field amplitudes at the plane interface will require that the spatial (and temporal) variation of all fields be the same"[7]. Therefore, the wavevectors respectively of the incident ($\vec{k}_i$), reflected ($\vec{k}_r$) and transmitted ($\vec{k}_t$) wave must satisfy the

following relation: $\vec{k}_i \cdot \vec{r} = \vec{k}_r \cdot \vec{r} = \vec{k}_t \cdot \vec{r}$ at the interface. This means that the transverse component of the k-vector ($\vec{k}_{//}$)must be the same for all the k-vectors. This requirement can be satisfied by the transmitted wave in two different ways (see figure II-1. 2): a) $\vec{k}_t$ pointing towards the refractive material and to the "right"(Fig II-1. 2a) or b) $\vec{k}_t$ pointing towards the

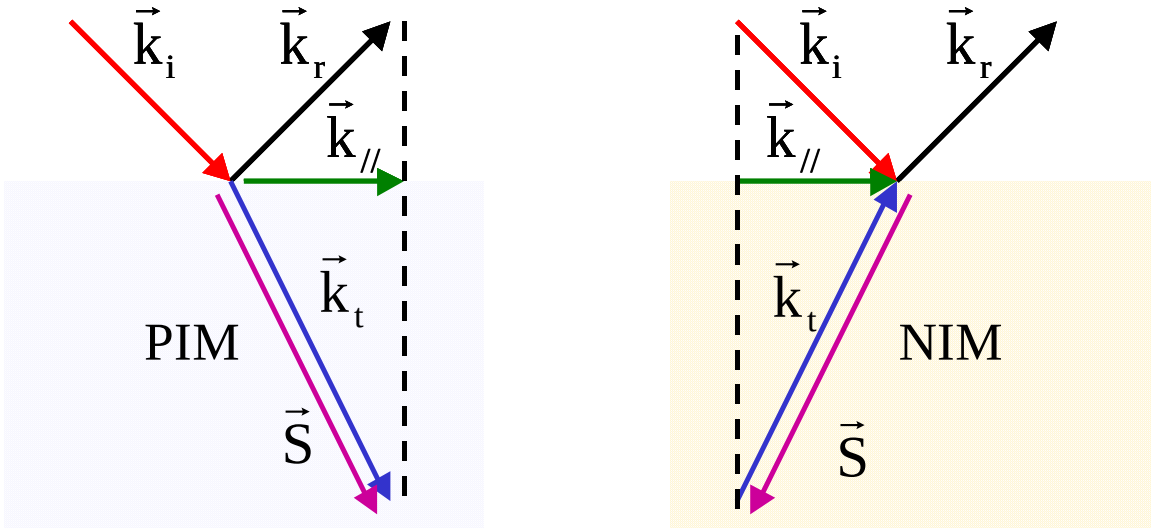

Fig II-1. 2: a) Reflection and refraction of a plane wave at an air/positive index material (PIM) interface b) Reflection and refraction of a plane wave at an air/NIM interface. $\vec{k}_i$ is the k-vector of the incident wave, $\vec{k}_r$ is the k-vector of the reflected wave, $\vec{k}_t$ is the k-vector of the transmitted wave, $\vec{k}_{//}$ is the transverse component of the k-vectors and $\vec{S}$ is the Poynting vector of the transmitted wave. Note that in both cases $\vec{k}_{//}$ is conserved as required by the Snell law and the Poynting vector of the transmitted wave points in the just direction, i.e. towards the refractive material. Also note that in the case of air/PIM interface $\vec{k}_t$ and $\vec{S}$ are parallel while they are anti-parallel in the case of air/NIM.

incident material and to the "left"(Fig II-1. 2b). The correct choice is the one that ensures the right behavior of the Poynting vector (see Eq. II-1. 4). In the negative index regime, i.e. μ and ε simultaneously negative, $\vec{S}$ and $\vec{k}_t$ are anti-parallel. This means that the correct behavior is the one with $\vec{k}_t$ pointing to the "left", contrary of what happens for ordinary positive index materials (PIMs). These considerations, together with Fig.II-1.2, also explain why sometimes negative index materials are also referred to as "left-handed materials". A consequence of the behavior just described is that, as predicted by Veselago [1], a concave/concave lens made of a NIM is

divergent, while a convex/convex lens is convergent, contrary of what would happen for lenses made of ordinary dielectric materials (see Fig. II-1.3)

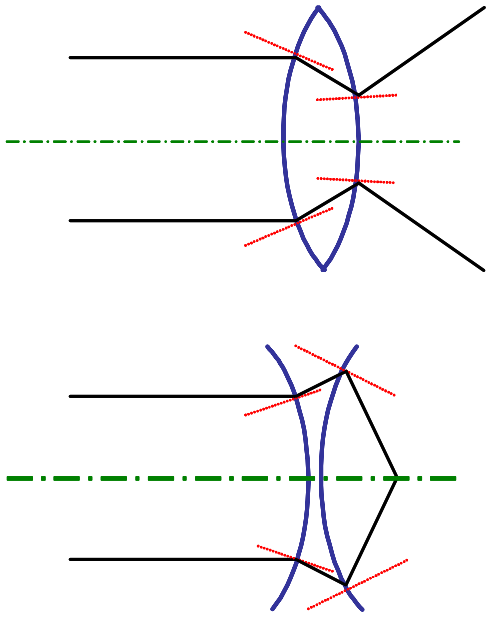

Fig II-1. 3: Path of the optical rays through lenses made of a negative index material.

II-1.3 Negative index materials and Drude model

The electric susceptibility and the magnetic permeability of a NIM can be described with a lossy Drude model [2,8]:

$$\varepsilon(\tilde{\omega}) = 1 - \frac{1}{\tilde{\omega}(\tilde{\omega} + i\tilde{\gamma}_e)}, \qquad \text{(II-1. 5a)}$$

$$\mu(\tilde{\omega}) = 1 - \frac{(\omega_{pm}/\omega_{pe})^2}{\tilde{\omega}(\tilde{\omega} + i\tilde{\gamma}_m)}, \qquad \text{(II1.5b)}$$

where $\tilde{\omega} = \omega/\omega_{pe}$ is the normalized frequency, ω_{pe} and ω_{pm} are the respective electric and magnetic plasma frequencies, $\tilde{\gamma}_e = \gamma_e/\omega_{pe}$ and $\tilde{\gamma}_m = \gamma_m/\omega_{pe}$ are the respective electric and magnetic loss terms normalized with respect to the electric plasma frequency. One may ask: "How realistic is the Drude model to describe the dispersive properties of a NIM?" In order to

answer this question we direct the reader's attention to Figs. (II.1-4). In Fig.(II.1-4(a)) we show the refractive index, the extinction coefficient, the real part of the electric susceptibility, and the real part of the magnetic permeability for a NIM whose dispersion is described by Eqs.(3). In Fig.(II.1-4(a)) we have taken the following parameters: $\omega_{pm}/\omega_{pe} = 0.8$ and $\tilde{\gamma}_e \approx \tilde{\gamma}_m \approx 10^{-4}$. In Fig. (II.1-4(b)) we show the refractive index and the extinction coefficient, in the range between 10.7 and 15 GHz, deduced from the *experimental* data reported in Ref.[3]. The figure shows that

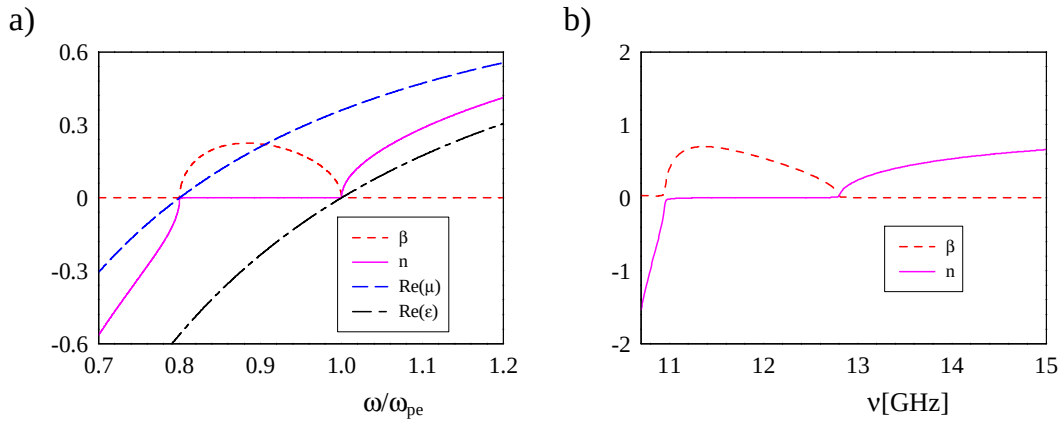

Fig II-1. 4: (a) Refractive index *n* (solid line), extinction coefficient β (short dashed line), Re(ε) (long-short dashed line), and Re(μ) (dashed line) vs. ω/ω_{pe} where ω_{pe} is the electric plasma frequency. In this case we have chosen in Eq.(3) $\omega_{pm}/\omega_{pe} = 0.8$ and $\tilde{\gamma}_e \approx \tilde{\gamma}_m \approx 10^{-4}$. The refractive index n goes from positive values at higher frequencies to negative values at lower frequencies. Moreover, where Re(ε) and Re(μ) have opposite sign *n* is nearly zero. Note that in the transition region the extinction coefficient increases considerably. (b) Refractive index (solid line) and extinction coefficient (short dashed line) as calculated from the experimental data reported in Ref.[3]. Note that the parameters in Fig.(a) have not been chosen in order to numerically fit the results presented in Fig.(b). The comparison only intends to show that the salient characteristics of the refractive index and the extinction coefficient can be qualitatively described by a Drude model.

the complex refractive index is negative below 11GHz and becomes almost a pure imaginary number in the range between 11GHz and 12.8GHz, where $-10^{-2}<n<10^{-2}$. Although the parameters in Fig. .(II.1-4(a)) were not chosen with the intent to fit the experimental data of Fig.(II.1-4(b)), nevertheless their behavior is remarkably similar in both cases. In other words, the salient characteristics of the refractive index and the extinction coefficient of currently available negative index meta-materials appear to be well-described by an effective Drude model. This is the main reason why the Drude model is widely used in most theoretical efforts [8] that address negative index materials.

II-1.4 Pulse propagation

Electromagnetic propagation in negative index materials can be, of course, also studied in pulsed regime. The dynamics of pulses can on one hand confirm the results obtained in the monochromatic plane wave approach, on the other hand it can put into evidence different aspects of negative refraction that are not taken into account in the former approach. Solving Maxwell's equations with two spatial coordinates (one longitudinal, one transverse) and time Scalora et al. [9] found negative refraction as the wave packet undergoes significant and unusual shape distortions. Both a direct calculation of the spatial derivative of the instantaneous, local phase of the pulse and a Fourier analysis of the signal reveal the same inescapable fact: that inside a negative-index material, a *transmitted, forward-moving* wave packet is indeed a superposition of *purely negative* wave vectors. In contrast, in positive index materials the generation of negative wave-numbers is associated with reflected or backward-propagating components. Moreover, the calculation confirms that causality is not violated in the short-pulse regime, and that energy and

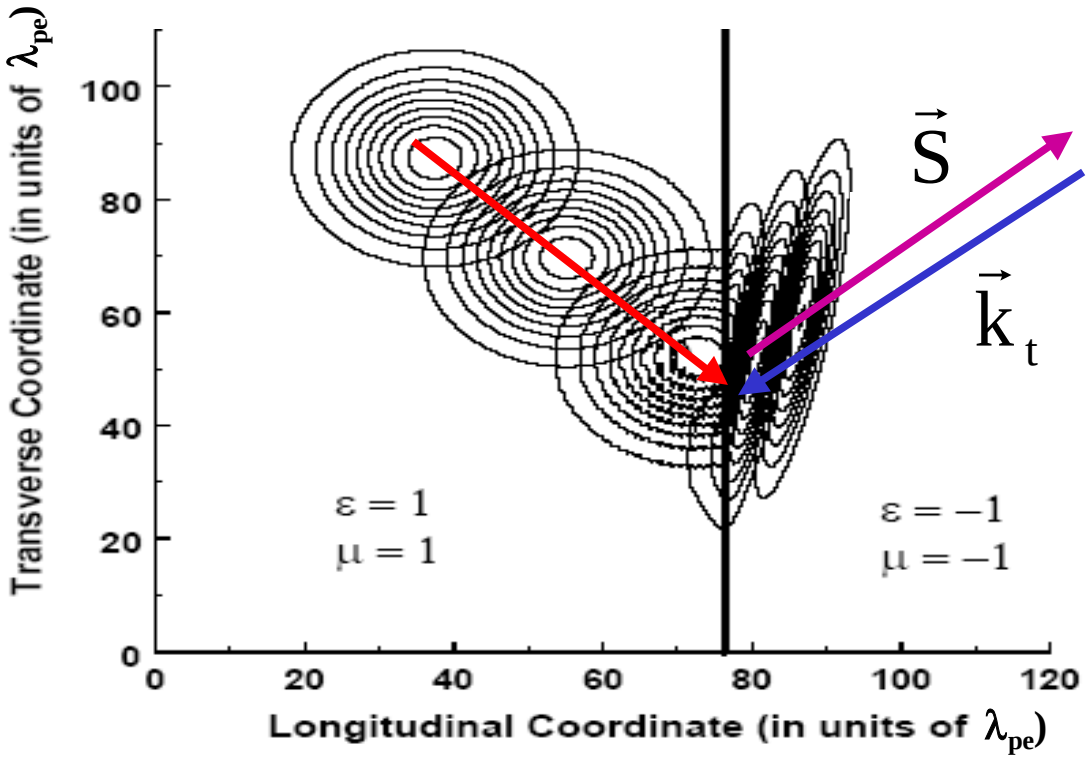

Fig. II-1. 5: A 100-wave cycles pulse crosses from vacuum into a NIM at an incident angle of 45 degrees, assuming a Drude-like dispersion model, and no absorption. $\lambda_{pe}= 2\pi c/\omega_{pe}$.The refraction angle is -45 degrees, as predicted by Snell's law and an index of refraction *n=-1*.

group velocities never exceed the speed of light in vacuum. Here we do not go into the technical details of the calculation. Suffice it to say that the pulse propagation algorithm uses a FFT-BPM (fast Fourier transform beam propagation method) ad hoc modified in order to handle reflections. More details can be found in our Ref. [9]. In Fig. (II-1. 5) we show the case of negative refraction of a pulse launched at 45 degree impinging the air/NIM interface. The dispersion properties of the NIM are taken according to the Drude model as in Eqs. (II-1. 3) with $\omega_{pe}=\omega_{pm}$ and negligible losses. The carrier frequency of the pulse ω_0 is centered in the spectral region where $\varepsilon=\mu=-1$.

References and Notes

[1] V.G. Veselago, *Sov. Phys. Usp*. **10**, 509 (1968).

[2] J. B. Pendry, *Phys. Rev. Lett*. **85**, 3966 (2000).

[3] R.A. Shelby, D.R. Smith, and S. Schultz, Science **292**, 77 (2001).

[4] Focus issue on: Negative Refraction and Metamaterials, *Optics Express*, **11**, pp.639-760 (2003) and references therein.

[5] L.D. Landau and E.M. Lifshitz "Electrodynamics of continuous media", Pergamon Press, NY (1960)

[6] Note that while solving Eq.(II-1.1) with the condition $\beta>0$ leads to the correct expressions of the refractive index and the extinction coefficient as given in Eqs.(2), on the other hand solving Eq.(1) with the condition $n>0$ leads to the following expressions:

$$n = \frac{\sqrt{\mathrm{Re}(\varepsilon\mu) + \sqrt{[\mathrm{Re}(\varepsilon\mu)]^2 + [\mathrm{Im}(\varepsilon\mu)]^2}}}{\sqrt{2}}, \quad \beta = \frac{\mathrm{Im}(\varepsilon\mu)}{\sqrt{2}\sqrt{\mathrm{Re}(\varepsilon\mu) + \sqrt{[\mathrm{Re}(\varepsilon\mu)]^2 + [\mathrm{Im}(\varepsilon\mu)]^2}}}.$$

The above expressions are equivalent to those given into Eqs.(II-1 2) only when $\mathrm{Im}(\varepsilon\mu)>0$ and they cannot be considered valid in general.

[7] P. Yeh "Optical waves in layered Media", John Wiley $Sons, New York (1988) cap 3.

[8] In addition to Pendry's work cited in Ref.[2] we give here a list of other theoretical papers where the dispersive properties of a NIM are described through a Drude model as in our Eq.(3): W. Ziolkowski and E. Heyman, *Phys. Rev. E* **64,** 056625 (2001); R.W. Ziolkowski and A.D. Kipple, *Phys. Rev. E* **68,** 026615 (2003); R.W. Ziolkowski, *Opt. Expr*. **11**,662 (2003); R.W. Ziolkowski, *Phys. Rev. E* **70,** 046608 (2004); G.D'Aguanno et al., *Phys. Rev. Lett.* **93,** 213902 (2004). In addition to Ref.[3], that is the case explicitly considered for the comparison drawn in Figs.1, several other experimental papers have been published where a NIM material has been realized with dispersive properties that can be described in a particular spectral range by a Drude model as in our Eq.(3). We cite for example: D.R. Smith et al. *Phys. Rev. Lett.* **84,** 4184 (2000); C.G. Parazzoli *et al*. *Phys. Rev.*

Lett. **90,** 107401 (2003); S. Linden *et al.*, *Science* **306,** 1351 (2004). In the last paper a magnetic resonance has been implemented at 100THz.

[9] M. Scalora, G. D'Aguanno, N. Mattiucci, M.J. Bloemer, J.W. Haus, A. M. Zheltikov, *App. Phys. B*, **81,** 393 (2005)

II-2 Linear Properties

II-2.1 Transmission properties, field localization and tunneling times.

We start studying the transmission properties of a *single* slab, Fabry-Perot etalon composed of a negative index material. Some of those properties are reminiscent of those of a multilayer, one-dimensional photonic band gap structure (1-D PBG) [1]. It is worth to point out that *while in a PBG structure the formation of the gap is due to interferential effects, in the case at hand the formation of the gap is essentially due to the peculiar dispersion properties of the bulk of the material.* We begin by describing the electric susceptibility and the magnetic permeability of the NIM with a lossy Drude model [2]:

$$\varepsilon(\tilde{\omega}) = 1 - \frac{1}{\tilde{\omega}(\tilde{\omega} + i\tilde{\gamma}_e)} \quad , \quad \mu(\tilde{\omega}) = 1 - \frac{(\omega_{pm}/\omega_{pe})^2}{\tilde{\omega}(\tilde{\omega} + i\tilde{\gamma}_m)}, \qquad \text{(II-2. 1)}$$

where $\tilde{\omega} = \omega/\omega_{pe}$ is the normalized frequency, ω_{pe} and ω_{pm} are the respective electric and magnetic plasma frequencies, $\tilde{\gamma}_e = \gamma_e/\omega_{pe}$ and $\tilde{\gamma}_m = \gamma_m/\omega_{pe}$ are the respective electric and magnetic loss terms normalized with respect to the electric plasma frequency. The refractive index *n* and the extinction coefficient β of the material are given by: $n + i\beta = \pm\sqrt{\varepsilon\mu}$. As already discussed in Chap. II-1, the sign in front of the square root must be chosen in a way that ensures the Poynting vector of the light refracted into a semi-infinite slab of NIM will always be directed away from the interface into the refracting material itself. Only one of the two possible solutions of the square root satisfies this requirement. The complex wavevector of the material is then calculated as $K(\omega)=(\omega/c)(n+i\beta)$ and the dispersion relation of the NIM can be visualized in the (K,ω) plane. In Figs.(II-2. 1) we show the dispersion relation of the NIM for two different values of the ratio ω_{pm}/ω_{pe} . We have also performed a systematic study of the dispersion relations as a function of the ratio ω_{pm}/ω_{pe} , and our findings can be summarized as follows: (i) the dispersion relation gives rise to a band gap in a spectral range around the electric plasma frequency where the refractive index gets value near to zero. (ii) The center-gap frequency $\omega_{c,gap}$ and the spectral width of the gap $\Delta\omega_{gap}$ depend on the electric and magnetic plasma frequency as

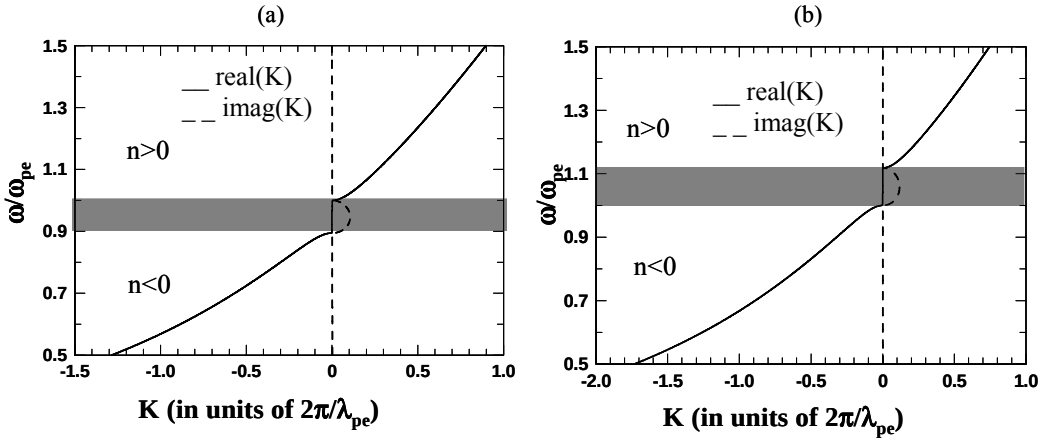

Fig. II-2. 1: Normalized frequency ω/ω_{pe} vs. K in units of $2\pi/\lambda_{pe}$ where $\lambda_{pe}=2\pi c/\omega_{pe}$ is the wavelength corresponding to the electric plasma frequency for (a) $\omega_{pm}/\omega_{pe}=(0.8)^{1/2}$ and (b) $\omega_{pm}/\omega_{pe}=(1.25)^{1/2}$. The solid lines correspond to Re(K) and the dashed lines to Im(K). In this case we have chosen in Eq.(1) $\tilde{\gamma}_e \approx \tilde{\gamma}_m \approx 4.5*10^{-4}$. The shaded regions indicate the spectral position of the band-gap. In the region below the gap n is negative.

follows: $\omega_{c,gap}=(\omega_{pe}+\omega_{pm})/2$ and $\Delta\omega_{gap}=|\omega_{pe}-\omega_{pm}|$. The only gap that forms disappears when $\omega_{pe}=\omega_{pm}$. (iii) The results shown in Figs. (II-2. 1) refer to the bulk properties of our NIM.

In Fig.(II-2. 2) we show the transmittance (bold-solid line) and the group velocity (thin-line) for a slab of NIM whose dispersion relation is described in Fig.(II-2. 1a). The group velocity is

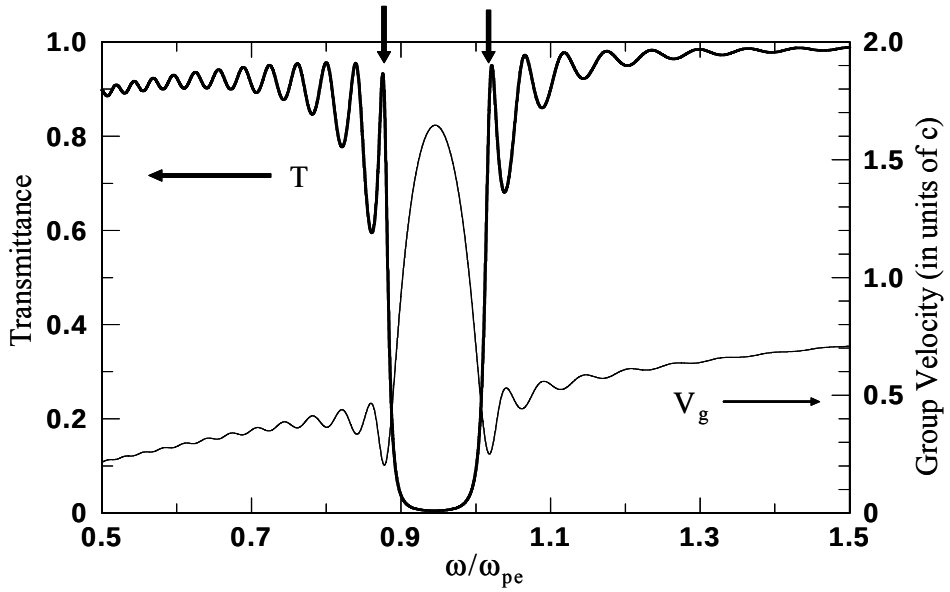

Fig. II-2. 2: Transmittance at normal incidence (solid-line) and group velocity (thin- line) vs. ω/ω_{pe} for a NIM of length $L=5\lambda_{pe}$ and $\omega_{pm}/\omega_{pe}=(0.8)^{1/2}$, i.e. with the dispersion properties described in Fig.(II-2. 1a). The arrows indicate the position of the band edge resonances.

calculated as: $V_g = L/\tau_\varphi$, where L is the length of the cavity and τ_ϕ is the Wigner time (or "phase time") and it gives the time that the transmitted part of an incident, quasi-monochromatic, un-chirped pulse takes to traverse a 1-D barrier [3]. In particular the group velocity is superluminal inside the gap while slow group velocities, less than 0.3c in this case, characterize the high and low frequency band-edge. The reflectivity near the center of the stop band is approximately 99%. Field localization properties at the high and low frequency band-edge are shown in Figs.(II-2. 3). In this case the structure admits localized modes at the peaks of

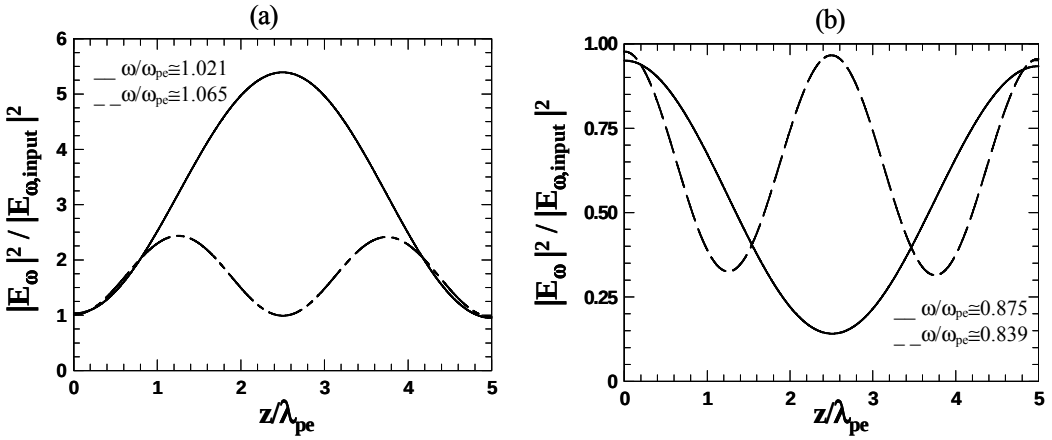

Fig. II-2. 3: (a) Field localization in the NIM for an input field tuned near the high-frequency band-edge at the first peak of transmission, $\omega/\omega_{pe}\cong 1.021$, (solid line) and at the second peak of transmission, $\omega/\omega_{pe}\cong 1.065$, (dashed line). (b) Field localization near the low frequency band edge at the first peak of transmission, $\omega/\omega_{pe}\cong 0.875$, (solid line) and at the second peak of transmission, $\omega/\omega_{pe}\cong 0.839$, (dashed line).

transmission near the high-frequency band edge (Fig. (II-2. 3a)) and delocalized modes at the low frequency side (Fig. (II-2. 3b)).

In the case of Figs.(II-2. 3) we have $\omega_{pm}/\omega_{pe} < 1$ and the localized mode is found at the high-frequency band edge. In contrast, when $\omega_{pm}/\omega_{pe} > 1$ the localized mode shifts to the low-frequency band-edge, as shown in Fig.(II-2. 4). In terms of the refractive index of the material, the field localization occurs for refractive indices in the range: $1 > n > 0$ when $\omega_{pm}/\omega_{pe} < 1$, while in the range: $0 > n > -1$ when $\omega_{pm}/\omega_{pe} > 1$.

Another aspect worthy of note is that the spectral position and the spectral width of the gap are independent on the length of the NIM at normal incidence. This is shown in Fig.(II-2. 5) where the transmission is calculated for different lengths of the NIM slab. The figure suggests

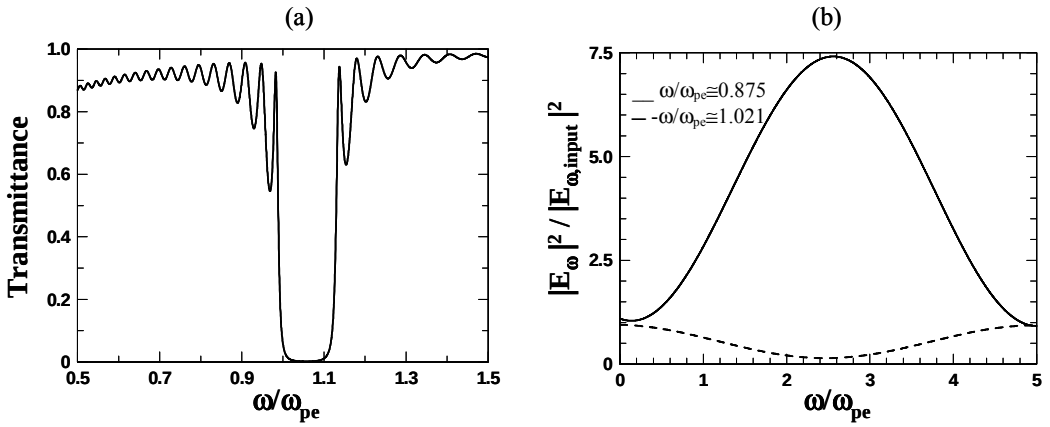

Fig. II-2. 4: (a) Transmittance vs. ω/ω_{pe} for a NIM of length L=5λ_{pe}. In this case $\omega_{pm}/\omega_{pe}=(1.25)^{1/2}$, i.e. the NIM has the dispersion properties described in Fig.(II-2. 1b). (b) Field localization at the low frequency band edge (solid line) and at the high frequency band edge (dashed line).

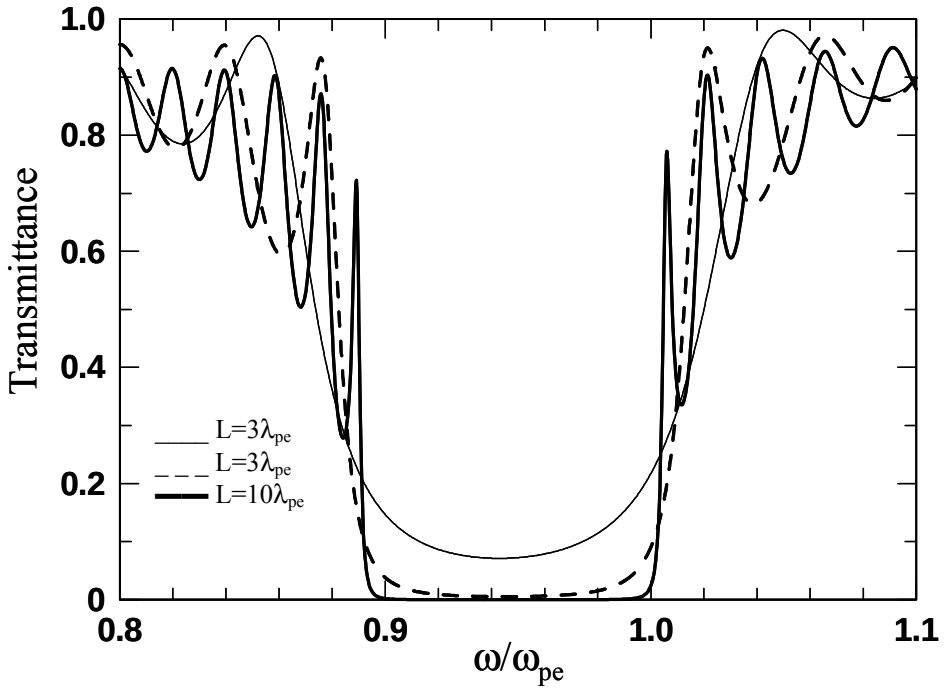

Fig. II-2. 5: Transmittance vs. ω/ω_{pe} for different lengths of the slab. The NIM has the dispersion properties described in Fig. (II-2. 1a). L=3λ_{pe}(thin-solid line), L=5λ_{pe} (dashed line), L=10λ_{pe} (thick-solid line)

that although the number of resonances in the pass band increases proportionally to the length of the structure, the position and the spectral width of the gap remain practically unchanged. The reason for this is due to the peculiar dispersion characteristics of the bulk of NIM, and not to interference effects, as for example in PBG structures.

At angular incidence and for a fixed length, the width of the gap increases as shown in Fig. (II-2. 6). This behavior is unusual compared to PBG structures where at angular incidence a blue shift of the gap is expected, but it can be easily explained as a total internal reflection. In fact the

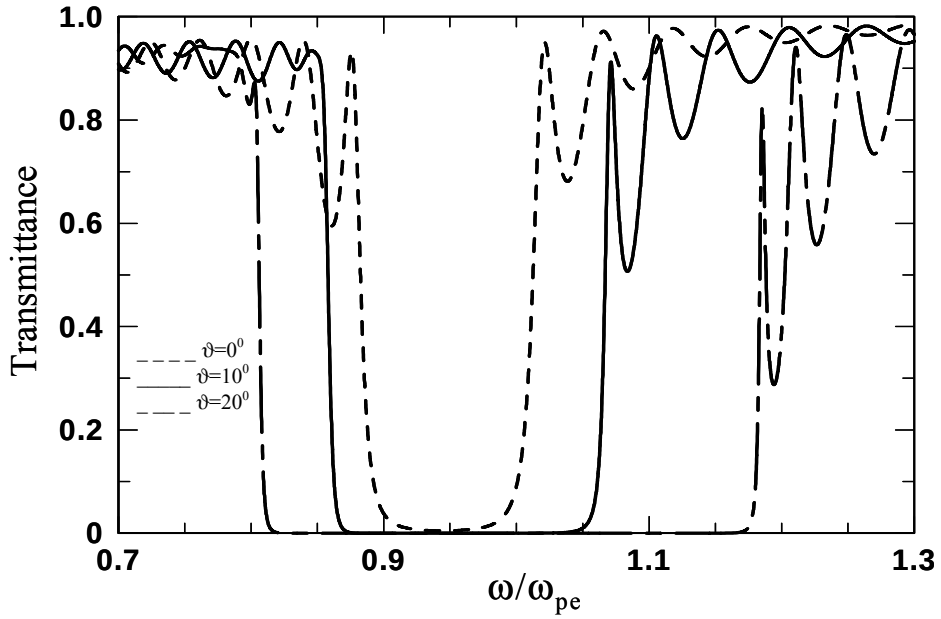

Fig. II-2. 6: Transmittance vs. ω/ω_{pe} for different angles (ϑ) of the incident radiation: 0^o (dashed line), 10^o(solid line), 20^o (long-short dashed line). The length of the NIM is $L=5\lambda_{pe}$ The NIM has the dispersion properties described in Fig. (II-2. 1a).

refraction index in the gap of the NIM is very close to zero and therefore a field incident at an angle (ϑ) from air, the air is in this case the high index medium, undergoes to a total internal reflection.

II-2.2 Omnidirectional gap.

Omnidirectional reflectors have been made in 1D PBGs by forming an extra wide gap[4-6]. The idea is to make the normal incidence gap extremely wide so that the shift with angle is not large enough to completely move the entire stop band to a new range of frequencies. The gap in a 1D PBG can be widened by having a very large index contrast and/or by adding more periods with different lattice constants. Omnidirectional NIMs do not have these constraints since the gap does not shift and actually widens with increasing angle of incidence. As already discussed in Chap. II-1, a convincing experimental demonstration of negative refraction was made by Shelby, Smith, and Schultz. They constructed a 2D NIM consisting of metal wires for the electric

response and split ring resonators (SRRs) for the magnetic response. According to their experimental results, the complex, frequency dependent electric susceptibility ε and the magnetic permeability μ of the NIM can be modeled as follows[7, 8]:

$$\varepsilon(\omega) = 1 - (\omega_{ep}^2 - \omega_{eo}^2)/(\omega^2 - \omega_{eo}^2 + i\gamma\omega) \quad \text{(II-2. 2a)}$$

$$\mu(\omega) = 1 - (\omega_{mp}^2 - \omega_{mo}^2)/(\omega^2 - \omega_{mo}^2 + i\gamma\omega) \quad \text{(II-2. 2b)}$$

where ω_{ep} is the electric plasma frequency, ω_{eo} is the electric resonance frequency, ω_{mp} is the magnetic plasma frequency and ω_{mo} is the magnetic resonance frequency and γ the loss term. The parameters are taken according to the experimental results reported in Ref. 7, i.e.: $\omega_{ep}=2\pi\times12.8$GHz, $\omega_{eo}=2\pi\times10.3$GHz, $\omega_{mp}=2\pi\times10.95$GHz, $\omega_{mo}=2\pi\times10.05$GHz, $\gamma=2\pi\times10$MHz. We want to clarify that in the following discussion, the material parameters of the NIM from Eqs. II-2. 2 are assumed to be isotropic, that is, we are assuming a fully 3D NIM structure. The NIM of Ref. [7] is actually a combination of a 1D electric and 2D magnetic metamaterial. The experimental results of negative refraction in Ref. [7] were demonstrated for TE polarization with the incident electric field always parallel to the metal wires. Therefore, we expect the NIM

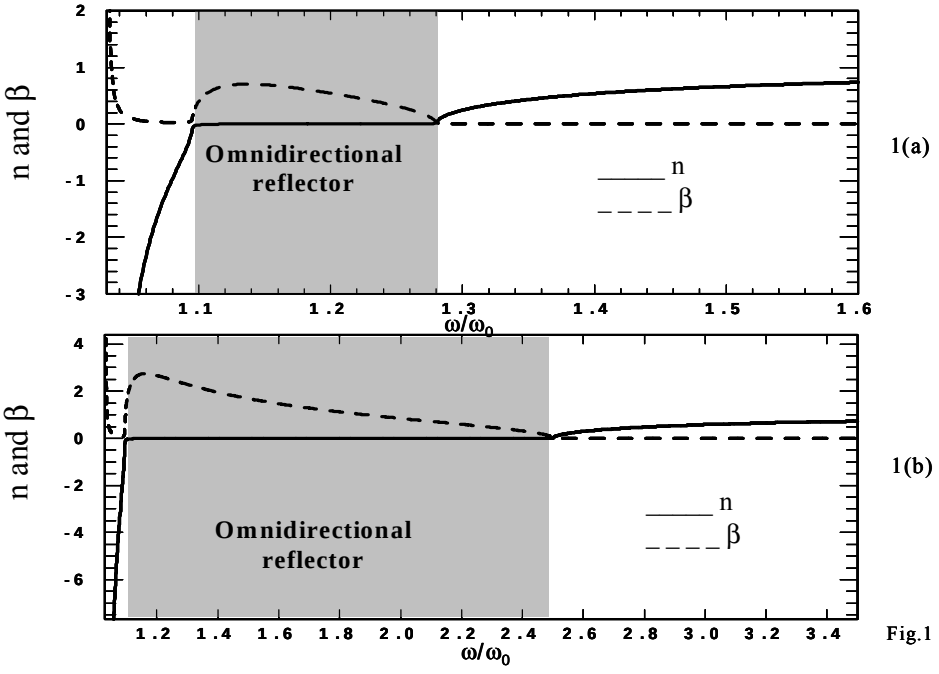

Fig. II-2. 7: Optical constants of a broadband omnidirectional reflector. Index of refraction n (solid line) and extinction coefficient β (dashed line) vs. ω/ω_0 where $\omega_0=2\pi\times10$GHz. a) optical constants based on the experimental parameters of Ref. [7]. b) we use the same parameters as in Fig. (II-2. 7a) except that $\omega_{ep}=2\pi\times25$GHz.

of Ref. [7] to display omnidirectional reflection for only TE polarization. A true omnidirectional reflector requires a 3D structure. Fig. (II-2. 7a) shows the optical constants for the material parameters described above. Fig. (II-2. 7b) shows the optical constants for the same material parameters as in Fig. (II-2. 7a) with the exception that the electric plasma frequency has been moved to $\omega_{ep} = 2\pi \times 25\text{GHz}$. Notice that a gap forms between the electric and magnetic plasma frequencies. On the low frequency side of the gap is the region of negative index. Inside the gap, the optical constants of the NIM are similar to a metal at optical frequencies with a small index of refraction and a small but finite extinction coefficient. For comparison, the optical constants of silver at λ = 620 nm are n=0.131 and β=3.88 (Ref. [9]). Metals are good reflectors at optical frequencies because the refractive index is close to zero and β is reasonably large. NIMs reflect radiation more efficiently than metals because the refractive index is essentially zero inside the gap.

Comparing Figs (II-2. 7a) with (II-2. 7b) illustrates the dependence of the gap on the choice

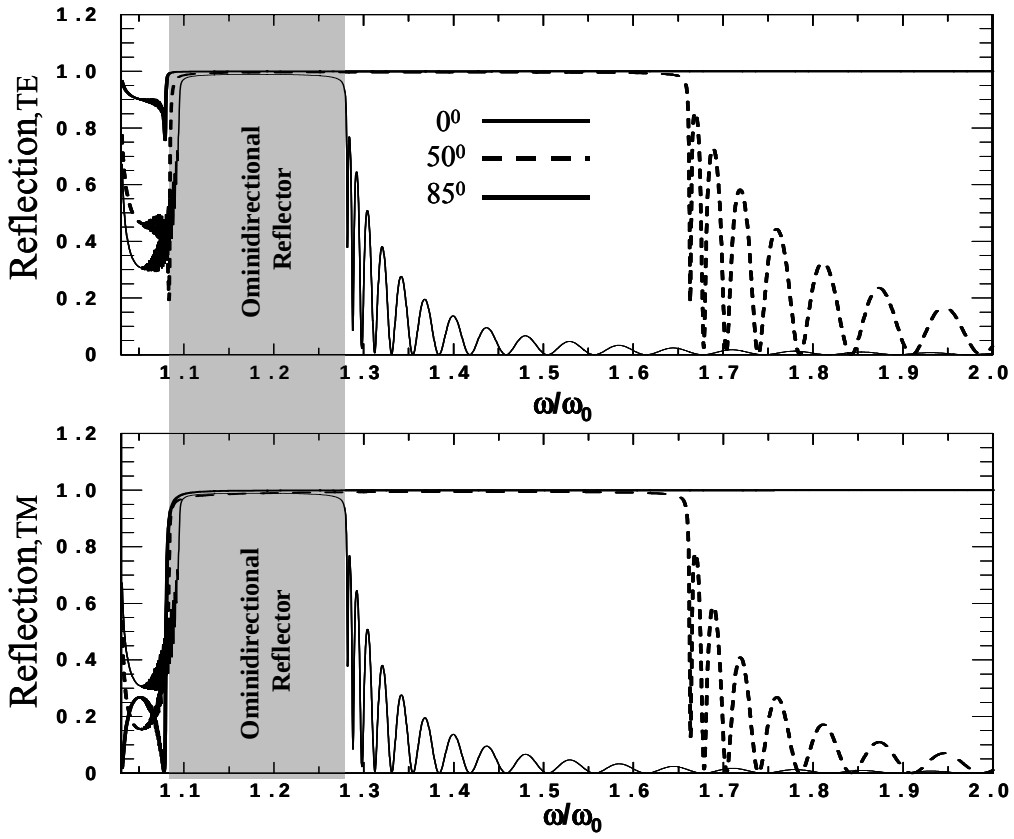

Fig. II-2. 8: Angular reflectivity of TE and TM polarized light for the optical constants shown in Fig. (II-2. 7a). The shaded area indicates the spectral position of the omnidirectional gap.

of ω_{ep} and ω_{mp}. Increasing the separation of the electric and magnetic plasma frequencies has expanded the width of the gap by a factor of five. It has been previously shown that the width and center frequency of the gap can be written as $\Delta\omega \sim |\omega_{ep}-\omega_{mp}|$ and $\omega_c \sim (\omega_{ep}+\omega_{mp})/2$, respectively, therefore, the larger the separation between the electric and magnetic plasma frequency the wider the spectral region where the NIM behaves as an omni-directional reflector. In Fig. (II-2. 8) we plot the reflectivity from a single layer of NIM having the optical constants shown in Fig. (II-2. 7a). The reflectivity has been calculated by the standard matrix transfer method. The structure is $L=5\lambda_0$ in length where $\lambda_0=2\pi c/\omega_0=3$cm. At normal incidence, the highly reflecting band occupies the region between the magnetic plasma frequency and the electric plasma frequency of the NIM. At the steeper angles of incidence, the low frequency side of the reflecting band remains fixed at the magnetic plasma frequency. On the high frequency side of the gap where the NIM has a positive index of refraction, the reflecting band begins to widen as the angle of incidence increases. In this frequency region, the optical constants of the NIM are similar to a low loss dielectric with the exception that the index of refraction is less than unity. The radiation is propagating from a high index region to a low index region and the highly

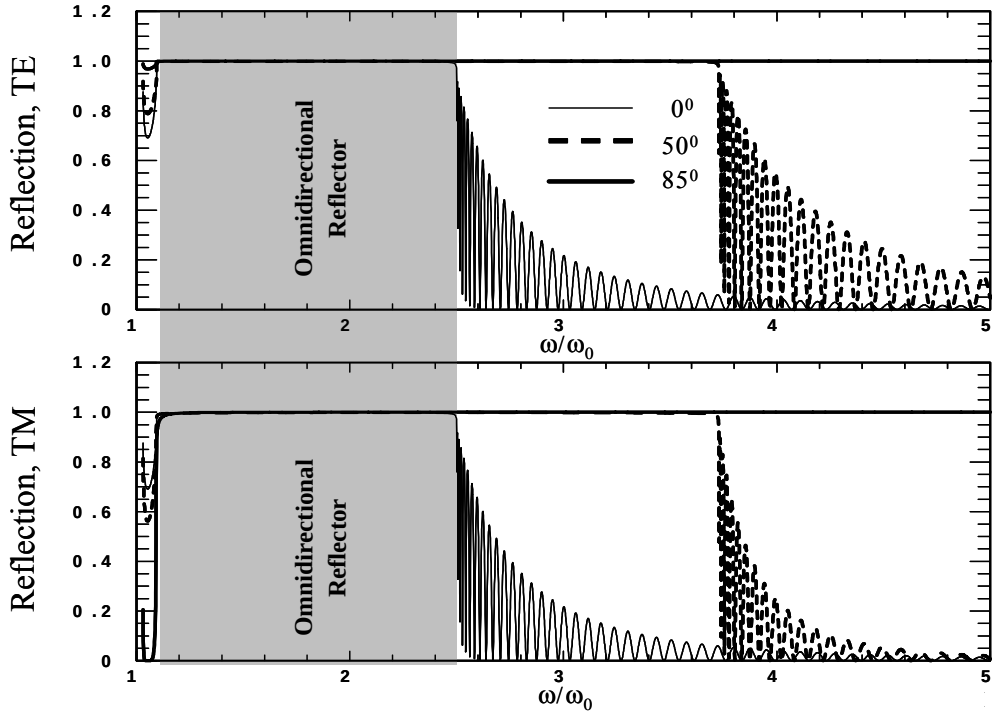

Fig. II-2. 9: Angular reflectivity of TE and TM polarized light for the optical constants shown in Fig. (II-2. 7b). The shaded area indicates the spectral position of the omnidirectional gap.

reflecting band terminates when the angle of incidence is less than the angle required for total internal reflection. In Fig. (II-2. 9) we show that increasing the separation between the magnetic plasma frequency and the electric plasma frequency can expand the omnidirectional reflecting band. The optical constants used to calculate the reflectivity are plotted in Fig. (II-2. 7b). By moving the electric plasma frequency from $\omega_{ep}=2\pi\times12.8$GHz to $\omega_{ep}=2\pi\times25$GHz, the

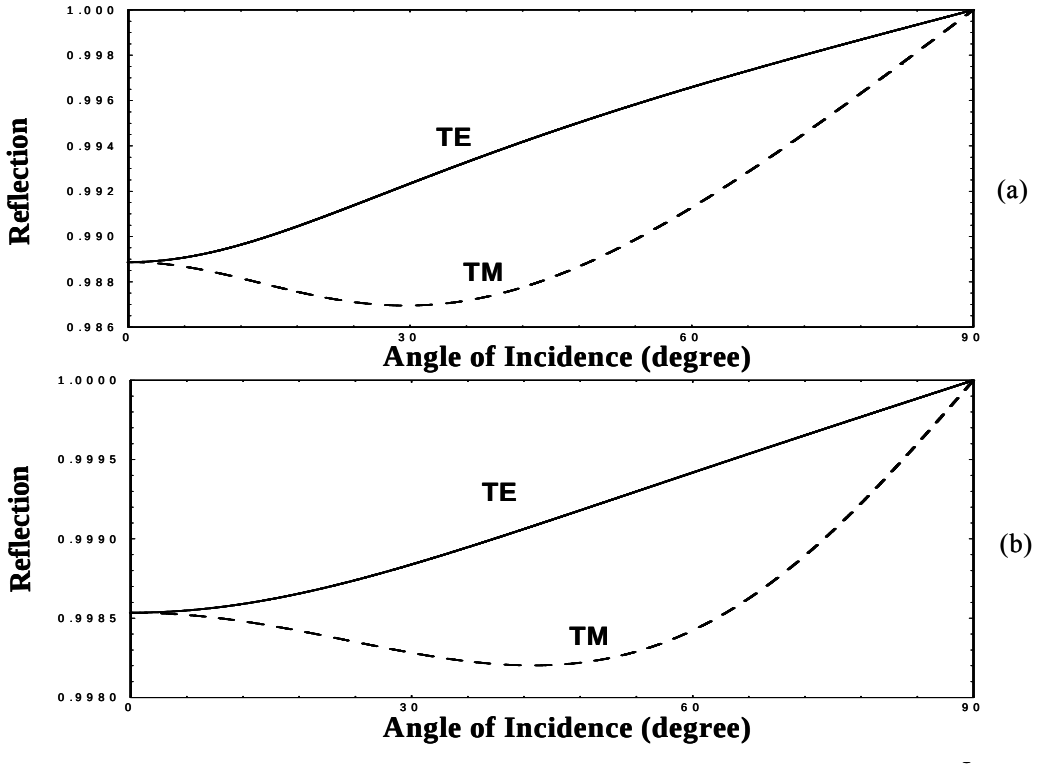

Fig. II-2. 10: TE and TM reflectivity vs. the angle of incidence at ω_c, i.e. at the central frequency of the gap. Figs. (II-2. 10a) and (II-2. 10b) are calculated using the optical constants of Fig. (II-2. 7a) and (II-2. 7b) respectively.

omnidirectional reflecting band has increased from $\Delta\omega/\omega_c$~15% to $\Delta\omega/\omega_c$ ~ 78%. The overall features of Figs (II-2. 8) and (II-2. 9) are similar with the exception that the width of the omnidirectional reflecting band has increased fivefold by shifting the electric plasma frequency.

For the center gap frequency, Fig. (II-2. 10) shows the complete angular dependence of the reflectivity for TE and TM polarizations. The polarization dependence shown in Fig. (II-2. 10) is reminiscent of a metal with the TM polarization showing a reduced reflectivity relative to TE polarization. The unusual feature illustrated in Fig. (II-2. 10) is that the reflectivity for all angles and polarizations never drops below 98.6%. The reflectivity plots of Figs. (II-2. 9) and (II-2. 10)

show that the larger the separation between the electric and magnetic plasma frequencies not only makes the omnidirectional reflecting band wider but also deeper. The center gap reflectivity for the NIM having $\Delta\omega/\omega_c \sim 78\%$ is never less than 99%. In this paper we have demonstrated that a single layer of a NIM has omnidirectional reflecting properties in the region between the electric and magnetic plasma frequencies. In this frequency region, the optical constants of a NIM are similar to real metals at optical frequencies. However, the reflecting properties of "metallic NIMs" are far superior to ordinary metals as a result of the real part of the index of refraction being nearly zero. The wide range of applications for NIMs in general and for metallic NIMS in particular, such as hollow core waveguides [10] and highly efficient back-reflectors for common light fixtures, give additional motivation to develop these unique metamaterials.

II-2.3 Dispersion-Free Pulse Propagation

Now, we will demonstrate that a NIM allows an ultrashort pulse to propagate with minimal

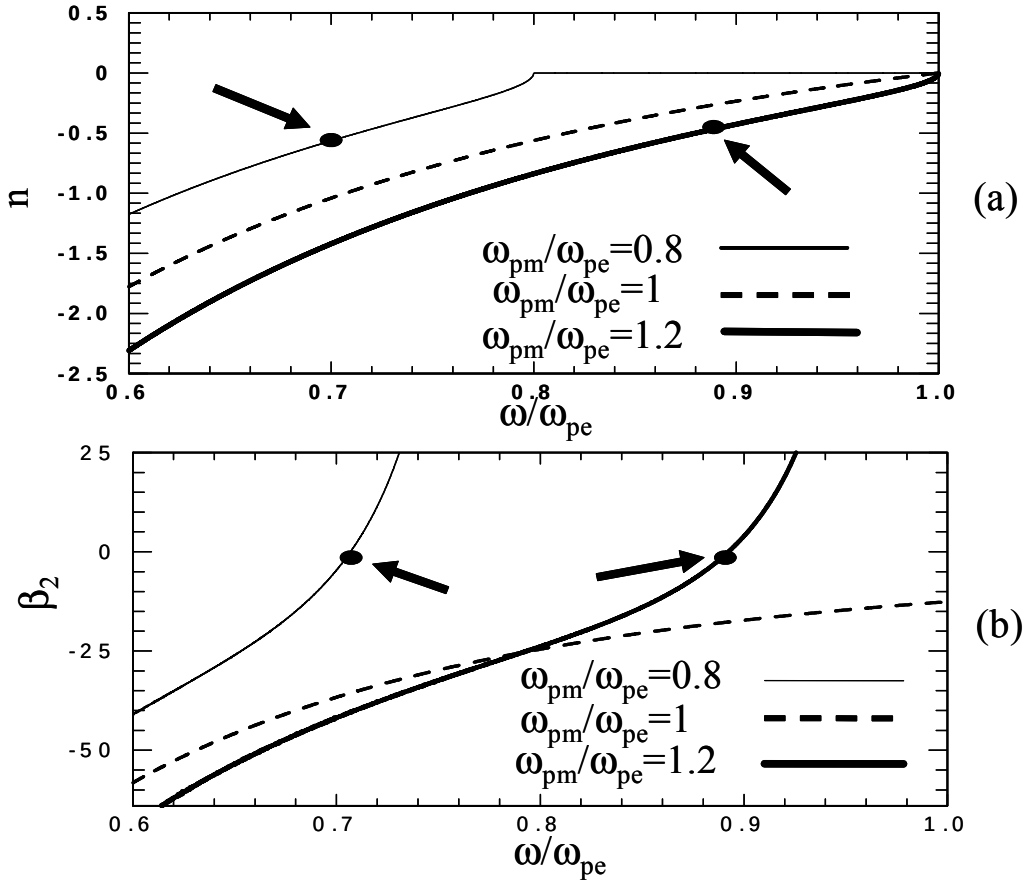

Fig. II-2. 11: a) Refractive index n vs. ω/ω_{pe} for different values of the ratio ω_{pm}/ω_{pe}; ω_{pm}/ω_{pe} =0.8 (thin solid line), ω_{pm}/ω_{pe} =1 (dashed line), ω_{pm}/ω_{pe} =1.2 (thick solid line). b) GVD parameter β_2 vs. ω/ω_{pe} for different values of the ratio ω_{pm}/ω_{pe}. Note that the β_2's curves are plotted only in the region around their respective zero GVD points. The arrows indicate the position of the zero GVD points. β_2 is calculated in units of $\lambda_{pe}/(4\pi^2c^2)$ where $\lambda_{pe}=2\pi c/\omega_{pe}$.

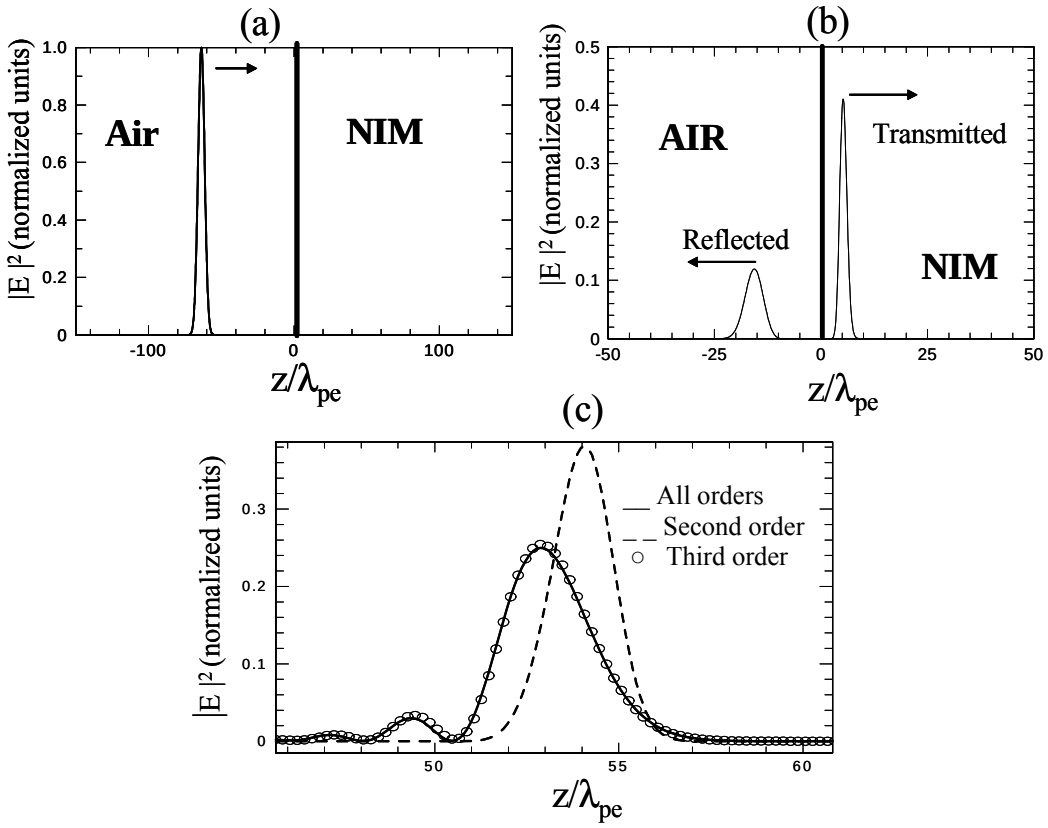

Fig. II-2. 12: Pulse propagation at different times of an ultrashort, gaussian, unchirped pulse in a NIM at the zero GVD point for ω_{pm}/ω_{pe} =0.8. a) At t_0=0, the pulse is in air directed toward the NIM, z=0 is the air/NIM interface. The peak of the square modulus of the incident electric field is normalized to 1. Its FWHM is ~$5\lambda_{pe}$ b) At t_1= $600\lambda_{pe}/(2\pi c)$, the incident pulse has entered the NIM giving rise to a reflected and to a transmitted pulse. The FWHM of the transmitted field is ~$2\lambda_{pe}$ c) At t_2=$1400\lambda_{pe}/(2\pi c)$, the transmitted pulse (thick solid line) has propagated for approximately $50\lambda_{pe}$ in the NIM and its FWHM is ~$2.67\lambda_{pe}$. For comparison: the same pulse (dashed line) at the same time after it has propagated in the same NIM but with the dispersion approximated up to the second order and with the dispersion approximated up to the third order (open circles).

dispersion due to the presence of a zero group velocity dispersion (GVD) point. We describe the NIM with a lossy Drude model as in Eqs. II-2. 1. In Fig.(II-2. 11a) we show the refraction index n for different values of the ratio ω_{pm}/ω_{pe} and in Fig.(II-2. 11(b)) we show the GVD parameter $\beta_2 = d^2k/d\omega^2$ [11], where k=nω/c is the NIM wavevector. In our model we assume $\tilde{\gamma}_e \sim \tilde{\gamma}_m \sim 10^{-4}$ and the extinction coefficient δ in the region around the zero GVD point is also of order 10^{-4}.

Note that the zero GVD points (i.e. the points where β_2=0) are located in the region where $\omega<\omega_{pe}$, and that no zero GVD point is present when $\omega_{pm}/\omega_{pe}=1$. In figures (II-2. 12) we show three snapshots of an unchirped, ultrashort, gaussian pulse with its central frequency tuned at $\omega_c=0.706\omega_{pe}$ that corresponds to a zero GVD point for $\omega_{pm}/\omega_{pe}=0.8$ as shown in Fig. (II-2. 11b).

In Fig. (II-2. 12a) the pulse is in air away from the interface air/NIM and its full width half maximum (FWHM) is ~$5\lambda_{pe}$, in Fig. (II-2. 12b) the pulse has entered the NIM giving rise to a reflected and a transmitted field. $\lambda_{pe}=2\pi c/\omega_{pe}$ is the electric plasma wavelength and c is the velocity of the light in vacuo. Note that the transmitted pulse is now spatially compressed with a FWHM of ~$2\lambda_{pe}$ while its temporal duration shortly after it has entered in the medium is $T\sim 2\lambda_{pe}/V_g\sim 5.8\lambda_{pe}/c$ where $V_g\sim 0.34c$ is the group velocity of the pulse. In Fig. (II-2. 12c) we show the transmitted pulse after it has propagated in the NIM for ~25 times its FWHM width, i.e. ~ $50\lambda_{pe}$. The pulse maintains a FWHM of less than $3\lambda_{pe}$. The ripples that appear on the left of the main pulse, and the slight increase in FWHM, are due mostly to third order dispersion. In our calculations all dispersion orders are taken into account [12].

In Fig.(II-2. 12c) we also show the pulse at the same time after it has propagated in the same NIM except that now the complex wavevector of the NIM, $\hat{k}(\omega)=(n+i\delta)(\omega/c)$, is approximated up to second order (dashed line) around the central frequency of the pulse, and up to the third order (open circles). In the case of second order dispersion only, the pulse propagates undistorted and with no dispersion, as expected. A small decrease in the amplitude of the undistorted pulse with respect to the amplitude of the incident pulse (see Fig. (II-2. 12b)) is due to linear absorption. On the other hand, taking dispersion terms up to third order produces a pulse almost identical in shape and amplitude to the pulse obtained via the exact calculation. The high order dispersion length, $L_D^{(3)}=T_0^3/|\beta_3|$, gives an estimate of the propagation distance over which the cubic dispersion term starts to play a significant role [13], T_0 is a measure of the initial pulse duration in time, and $\beta_3=d^3k/d\omega^3$. In the case depicted in figure (II-2. 12), $T_0\sim 5\lambda_{pe}/c$, and $d^3k/d\omega^3 \sim 700\lambda_{pe}^2/(8\pi^3c^3)$, giving a dispersion length $L_D^{(3)}\sim 40\lambda_{pe}$, consistent with the results of our numerical calculation. In figures (II-2. 13) the central frequency of the pulse is now tuned at $\omega_c=0.892\omega_{pe}$, that corresponds to the zero GVD point when $\omega_{pm}/\omega_{pe}=1.2$. The incident pulse has the same duration in time of that shown in Fig. (II-2. 12a), i.e. $T_0\sim 5\lambda_{pe}/c$. The calculated high-order dispersion length is now $L_D^{(3)}\sim 60\lambda_{pe}$, which is longer than that of the previous case; this is consistent with the results of our numerical calculation (see Fig.(II-2. 13c)).

In principle, the use of longer pulses would give rise to much longer dispersion length: for example the use of a pulse of time duration $T_0\sim 5\times 10^3\lambda_{pe}/c$ would make the dispersion length

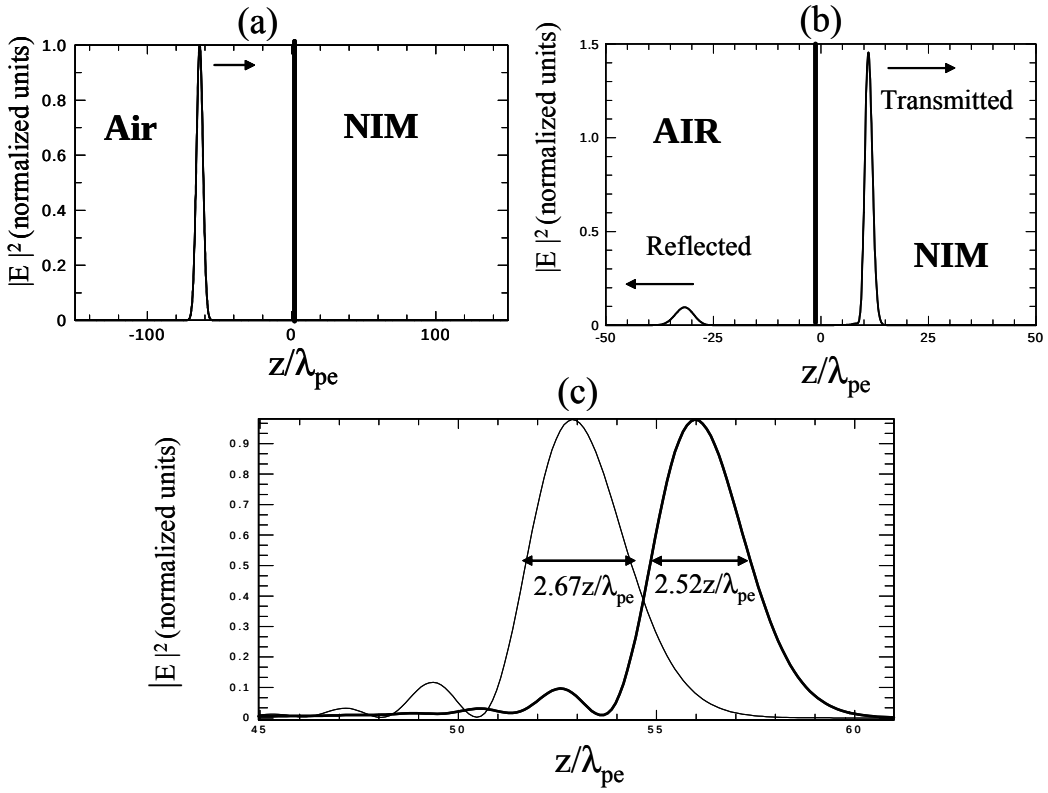

Fig. II-2. 13: Pulse propagation in a NIM at the zero GVD point for ω_{pm}/ω_{pe} =1.2. a) Incident pulse at t_0=0. b) Transmitted and reflected fields at t_1= $600\lambda_{pe}/(2\pi c)$. c) Transmitted pulse (thick solid line) at t_2=$1400\lambda_{pe}/(2\pi c)$. For comparison: transmitted pulse calculated in Fig. II-2. 12c) (thin solid line in the present figure) but with its amplitude renormalized to the amplitude of the pulse calculated in this case.

longer of a factor 10^9 than those previously calculated and therefore the pulse could propagate undistorted and with no dispersion for a distance of approximately $10^{10}\lambda_{pe}$. Moreover the dependence of the position of the zero GVD points on the electric and magnetic plasma frequency might open the door to a whole new class of artificial materials assembled in such a way to obtain dispersion free propagation in spectral regions otherwise inaccessible for conventional positive index materials. In photonic crystal fibers [13] or in tapered fibers [14], for example, the tunability of the zero-GVD point has been demonstrated within the entire visible range. In contrast, NIMs offer the possibility to tune the zero GVD zone in a quite different spectral range that spans from the microwave to near-infrared range. In Reference [7], for example, a NIM was fabricated and experimentally tested in the microwave range, while the experimental results reported in Reference [15] point toward the possibility to have a NIM operating in the near infrared regime.

However, although at least in principle dispersion-free propagation in NIMs is possible, still the issue of the absorption and/or loss is a serious obstacle to its practical realization. In our model the extinction coefficient is of the order of 10^{-4} , corresponding to an attenuation length of several hundreds of wavelengths in units of λ_{pe}. This means that, for example, a pulse of temporal duration $T_0 \sim 5\times10^2\lambda_{pe}/c$ will be attenuated by a factor 1/e after it has propagated only for approximately one FWHM. Currently available meta-materials experimentally tested have an even shorter attenuation length:~10 wavelengths or less [7]. It is interesting to note that absorption represents a limiting factor also in the case of the so-called "superlensing" effect [16]. On the other hand, while the causality principle requires that the real and imaginary parts of the dispersion of a medium be Kramers-Kronig pairs, it does not put a limit to how small the absorption of a medium should be, as long as it is not zero. The real and imaginary parts of both ε and μ in our lossy Drude model are in fact Kramers-Kronig pairs regardless of how small the electric and magnetic loss terms may be. Therefore, while NIMs with low absorption are at the present time out of reach, nevertheless, in principle, nothing prevents their availability in the near future.

Conclusions

We have reported novel, interesting properties of NIMs. We have shown that even a single slab of such material has several significant characteristics, such as: high transmittance and slow group velocity near the band edge; high reflectivity and superluminal group velocity in the band gap. Moreover, a single layer of a negative index material has omnidirectional reflection properties. In the range between the electric plasma frequency and the magnetic plasma frequency, negative index materials reflect radiation for all angles of incidence and polarization with reflectivities of ~99%. In addition, with increasing angles of incidence, the reflecting band does not shift in frequency but actually widens. The operational bandwidth can be 100% or greater by increasing the separation between the electric and magnetic plasma frequencies.

The dispersion properties of NIMs allow the presence of a zero group velocity dispersion point. The spectral position of the zero group velocity dispersion point can be controlled varying the ratio between the electric and magnetic plasma frequency. In this way it is possible, at list in principle, to obtain dispersion free propagation in spectral regions otherwise inaccessible using conventional positive index materials. Our predictions are confirmed by pulse propagation simulations where all orders of the complex dispersion of the material are taken into account.

References and Notes

[1] G. D'Aguanno, M.Centini, M.Scalora, C.Sibilia, M.J BLoemer, C.M. Bowden, J.W Haus, and M. Bertolotti, *Phys. Rev. E* **63,** 36610 (2001).

[2] R.W. Ziolkowski and E. Heyman, Phys. Rev E **64,** 056625 (2001)

[3] G. D'Aguanno, M. Centini, M.J. Bloemer, K. Myneni, M. Scalora, C. Sibilia, M. Bertolotti, *Opt. Lett.* **27**, 176 (2002).

[4] K.V. Popov, J.A. Dobrowolski, A.V. Tikhonravov, B.T. Sullivan, Applied Optics **36**, 2139 (1997).

[5] M. Deopura, C.K. Ullal, B. Temelkuran, Y. Fink, Optics Letters **26**, 1197 (2001).

[6] E. Xifre-Perez, L.F. Marsal, J. Pallares, and J Ferre-Borrull, J. Appl. Phys. **97**, 064503 (2005).

[7] R.A. Shelby, D.R. Smith, and S. Schultz, Science **292**, 77 (2001).

[8] R.W. Ziolkowski and E. Heyman, Phys. Rev. E **64**, 056625 (2001).

[9] *Handbood of Optical Constants of Solids,* edited by E.D. Palik, (Academic, New York, 1985).

[10] G. D'Aguanno, N. Mattiucci, M. Scalora, M.J. Bloemer, Phys Rev. E **71** 046603 (2005).

[11] G.P. Agrawal, *Nonlinear Fiber Optics*, Academic Press, San Diedgo, 1995

[12] The electric field has been calculated as follows:

$$E(z,t) = \int_{-\infty}^{+\infty} E(0,\omega)\exp(-i\omega t)[\exp(i\omega z/c) + r(\omega)\exp(-i\omega z/c)]d\omega \text{ for } z<0 \text{ and}$$

$$E(z,t) = \int_{-\infty}^{+\infty} t(\omega)E(0,\omega)\exp[i(\hat{k}(\omega)z - i\omega t)]d\omega \text{ for } z>0,$$

where $r(\omega)$ and $t(\omega)$ are respectively the reflection and transmission coefficient of the air/NIM interface, $E(0,\omega)$ is the spectral amplitude of the incident pulse, $\hat{k}(\omega)$ is the complex wavevector of the NIM.

[13] P. St. J. Russell, Science **299**, 358 (2003), and references therein.

[14] R. Zhang, J. Teipel, X. Zhang, D. Nau, H. Giessen, *Opt. Express* **12,** 1700 (2004), and references therein.

[15] S. Linden, C. Enkrich, M. Wegener, J. Zhou, T. Koschny, C.M. Soukoulis , *Science* **306,** 1351 (2004).

[16] J.B. Pendry, *Phys. Rev. Lett*. **85,** 3966 (2000)

II-3 Guiding properties of negative index materials.

II-3.0 Introduction

We numerically demonstrate that a planar waveguide in which the inner layer is a gas with refractive index $n_0=1$, sandwiched between two identical semi-infinite layers of a negative index material, can support both transverse electric (TE) and transverse magnetic (TM) guided modes with low losses. Recent developments in the design of meta-materials with an effective negative index suggest that this waveguide could operate in the infrared region of the spectrum.

In optics it is well known that when the inner layer of a planar waveguide is a gas with refractive index $n_0=1$ and it is sandwiched by two standard dielectric materials with refractive index $n>1$, total internal reflections cannot be achieved. The field coupled inside such a waveguide attenuates in the propagation direction by leaking power to the two bounding media [1]. The losses suffered via these "leaky" modes may be balanced when the molecular gas in the core is an active medium, as for example in CO_2 waveguide lasers [2-3]. In metal-clad waveguides [4] the refractive index of the guiding layer can be arbitrarily low as long as it is greater than the refractive index of the substrate. Total internal reflections are always achieved thanks to the low refractive index of the metal. In Ref.[4] guiding has been demonstrated in an air-polystyrene-silver waveguide at optical frequencies, in a 1.81μm thick polystyrene film. Losses were estimated at approximately 1dB/cm for the fundamental TE mode. The theory of hollow waveguides has been developed in Ref.[5], and different types of hollow waveguides in the infrared have been realized during the years. We cite for example hollow sapphire fibers [6], hollow Ag/AgI coated glass waveguides [7], ZnS-coated Ag hollow waveguides [8]. These guides have losses as low as 0.1dB/m at 10.6μm, for a bore diameter of approximately 1000μm. In the visible region, a tremendous breakthrough in the possibility of confining light in air has been achieved at the end of 1999, with the introduction of the so-called photonic crystal fibers (PCFs) [9-10]. In a PCF light confinement does not require a core with a higher refractive index because guidance is achieved not by total internal reflection, but by the presence of a cladding in the form of a full two-dimensional photonic band gap. We note also that PCFs are single-mode fibers, while traditional hollow waveguides are highly multimodal. On the other hand, the fundamental mode in traditional hollow waveguides has generally a much longer attenuation length than all higher order modes thanks to lower diffraction losses. Therefore, it is clear that for some applications the initial presence of many modes can be easily overcome.

The aim of this work is to demonstrate that light can be confined in air also by using a waveguide where the bounding medium, or cladding, is made of a NIM. In this case the confinement is due, as in classical waveguides, to total internal reflections. The guiding properties of a waveguide with a core made of NIM and a cladding composed of a standard dielectric material have been studied in Refs.[11], where it was demonstrated that guided modes are admitted. In our work we study the opposite configuration, i.e. a symmetric waveguide where an air-core is surrounded by a NIM. We note that, to our knowledge, at the present time an experimental realization of a meta-materials that posses an effective negative index has been achieved only in the microwave regime [12]. In this regard, several efforts are currently underway to design NIMs at higher frequency than the microwave regime. In Ref.[13-14], for example, O' Brian and Pendry have designed a NIM in the infrared region, and its nonlinear properties also has been numerically studied. The structure consists of a periodic nano-structured array of modified split-ring resonator which is magnetically active in the near-infrared region of the spectrum. The structure is numerically demonstrated to posses a negative effective permeability at telecommunications wavelengths, i.e. 1.5μm. Although further material development is still clearly needed, the practical realization of meta-materials in the infrared region seems to be within reach [15], and the results reported in Ref.[13-15] help to put our present work in its proper perspective.

II-3.1 Basic equations

In the last chapter we have widely explored the linear properties of negative index material and the similarity with PBG structures. Both exhibit a transmission gap, but in PBG the formation of the gap is due to destructive interference caused by the periodic arrangement of scattering or diffracting elements whose sizes are on the order of the incident wavelength. In contrast, NIMs are structured on a much finer scale that ranges from $1/10^{th}$ to $1/1{,}000^{th}$ of the wavelength [15], and therefore they respond with an effective dispersion that is essentially due to the bulk properties of the medium. However, while the nature of the gap is different in the two cases, it would be interesting to explore the possibility of using NIMs in the spectral region of opacity as the cladding of a waveguide (see Fig. (II-3. 1)). In analogy with PCF, where the a 2-D PBG is used as a cladding. As usual we will describe the electric and magnetic response of NIMs thought a lossy Drude model:

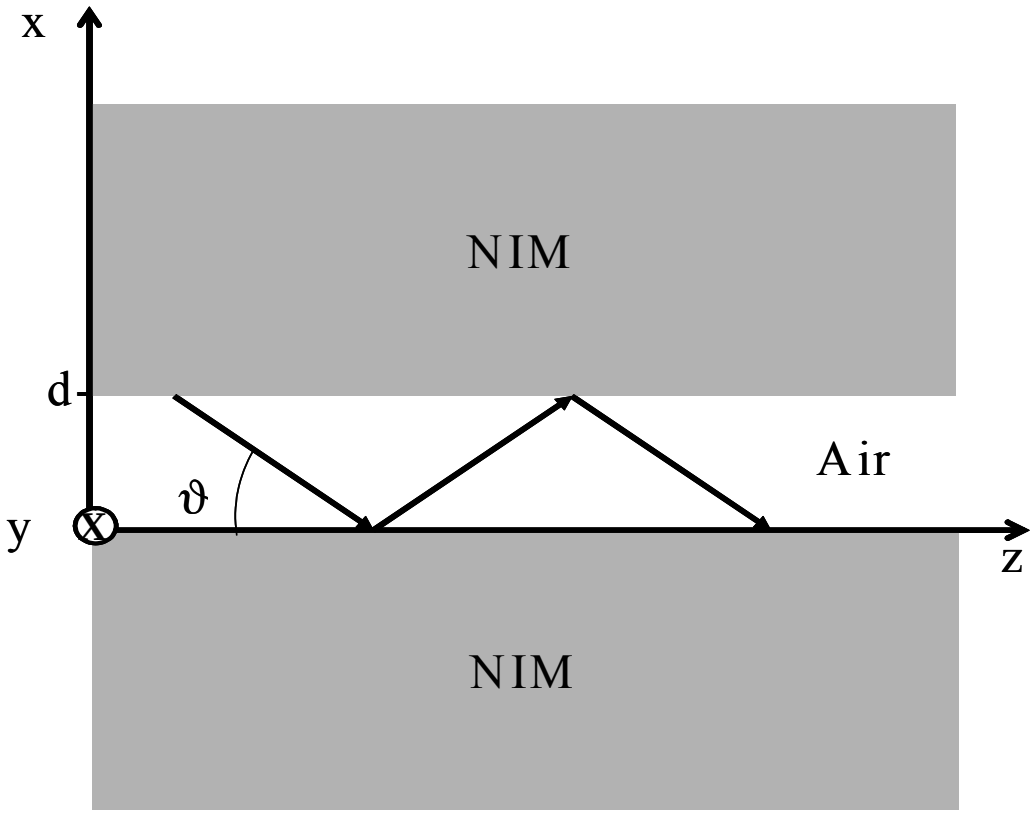

Fig. II-3. 1 Schematic representation of the geometry we study. A core of air of thickness *d* is sandwiched between two identical semi-infinite layers of NIM. ϑ is the angle formed by the wavevector of the radiation with the propagation axis z. The y axis is orthogonal to the plane (x,z).

$$\varepsilon(\tilde{\omega}) = 1 - \frac{1}{\tilde{\omega}(\tilde{\omega} + i\tilde{\gamma}_e)} \quad , \quad \mu(\tilde{\omega}) = 1 - \frac{(\omega_{pm}/\omega_{pe})^2}{\tilde{\omega}(\tilde{\omega} + i\tilde{\gamma}_m)} , \qquad \text{(II-3. 1)}$$

where $\tilde{\omega} = \omega/\omega_{pe}$ is the normalized frequency, ω_{pe} and ω_{pm} are the respective electric and magnetic plasma frequencies, $\tilde{\gamma}_e = \gamma_e/\omega_{pe}$ and $\tilde{\gamma}_m = \gamma_m/\omega_{pe}$ are the respective electric and magnetic loss terms normalized with respect to the electric plasma frequency. We have taken the following parameters: $\omega_{pm}/\omega_{pe} = 0.8$ and $\tilde{\gamma}_e \approx \tilde{\gamma}_m \approx 10^{-4}$.

We begin by first focusing on the TE modes. In this case the electric field is polarized along the y axis, (see Fig. (II-3. 1)) and the Helmholtz equation for our geometry is:

$$\frac{\partial^2 E_y(x,z)}{\partial x^2} + \frac{\partial^2 E_y(x,z)}{\partial z^2} + \frac{\omega^2}{c^2}\hat{f}(x)E_y(x,z) = 0 , \qquad \text{(II-3. 2)}$$

where $\hat{f}(x)=\hat{n}^2$ for x>d and x<0 , while $\hat{f}(x)=n_0$ for d ≥x≥0. $\hat{n}$ is the refractive index of the NIM and n_0 is the refractive index of the core of the waveguide. The solution of Eq. (II-3. 2)can be written as follows:

$$E_y(x,z)=\begin{cases} A_1 exp\left[i\frac{\omega}{c}\left(n_0 z\cos\hat{\vartheta}-\hat{n}x\sqrt{1-\frac{n_0^2\cos^2\hat{\vartheta}}{\hat{n}^2}}\right)\right] & x<0 \\ exp\left(i\frac{\omega}{c}n_0 z\cos\hat{\vartheta}\right)\left[A_2 exp\left(i\frac{\omega}{c}n_0 x\sin\hat{\vartheta}\right)+A_3 exp\left(-i\frac{\omega}{c}n_0 x\sin\hat{\vartheta}\right)\right] & 0\le x\le d \\ C exp\left[i\frac{\omega}{c}\left(n_0 z\cos\hat{\vartheta}+\hat{n}(x-d)\sqrt{1-\frac{n_0^2\cos^2\hat{\vartheta}}{\hat{n}^2}}\right)\right] & x>d \end{cases} \quad \text{(II-3. 3)}$$

where C is an arbitrary normalization constant that is chosen consistent with the following normalization condition: $\int_{-\infty}^{+\infty}\left|E_y(x,z=0)\right|^2 dx=1$. The choice of the complex parameters A_1, A_2, A_3 and $\hat{\vartheta}$ is determined by imposing that E_y, as well as $(1/\mu)(\partial E_y/\partial x)$, must be continuous at both x=0 and x=d. The continuity requirements lead to the following modal equation for $\hat{\vartheta}$:

$$tan\left(\frac{\omega}{c}n_0 d\sin\hat{\vartheta}\right)=-i\frac{\frac{2n_0\hat{n}\sin\hat{\vartheta}}{\mu}\sqrt{1-\frac{n_0^2}{\hat{n}^2}\cos^2\hat{\vartheta}}}{n_0^2\sin^2\hat{\vartheta}+\frac{\hat{n}^2}{\mu^2}-\frac{n_0^2}{\mu^2}\cos^2\hat{\vartheta}}, \quad \text{(II-3. 4)}$$

and to the following system of linear algebraic equations for A_1, A_2, and A_3:

$$\begin{pmatrix} 1 & -1 & -1 \\ \frac{\hat{n}}{\mu}\sqrt{1-\frac{n_0^2}{\hat{n}^2}\cos^2\hat{\vartheta}} & n_0\sin\hat{\vartheta} & -n_0\sin\hat{\vartheta} \\ 0 & exp\left(i\frac{\omega}{c}n_0 d\sin\hat{\vartheta}\right) & exp\left(-i\frac{\omega}{c}n_0 d\sin\hat{\vartheta}\right) \end{pmatrix}\begin{pmatrix} A_1 \\ A_2 \\ A_3 \end{pmatrix}=\begin{pmatrix} 0 \\ 0 \\ C \end{pmatrix}. \quad \text{(II-3. 5)}$$

We note that ϑ (i.e. the angle that the wavevector of the radiation forms with the propagation axis z - see Fig. (II-3. 1)) and the attenuation length L' (i.e. the length along z covered by the radiation before its intensity drops of a factor *1/e*) are linked to the complex parameter $\hat{\vartheta}$ through the following relations:

$$\vartheta = ar\cos[Re(\cos\hat{\vartheta})]\ , \qquad \text{(II-3. 6a)}$$

$$L' = \frac{c}{2\omega n_0\, Im(\cos\hat{\vartheta})}\ . \qquad \text{(II-3. 6a)}$$

The calculation for TM modes follows a development similar to that of TE modes. In the case of TM modes we must impose the continuity conditions on the magnetic field H_y and on $(1/\varepsilon)(\partial H_y/\partial x)$. The solution for TM modes and the modal condition can be obtained from those calculated for TE modes by making the following formal transformations: $E_y \rightarrow H_y$ and $\mu \rightarrow \varepsilon$.

II-3.2 Results and discussion.

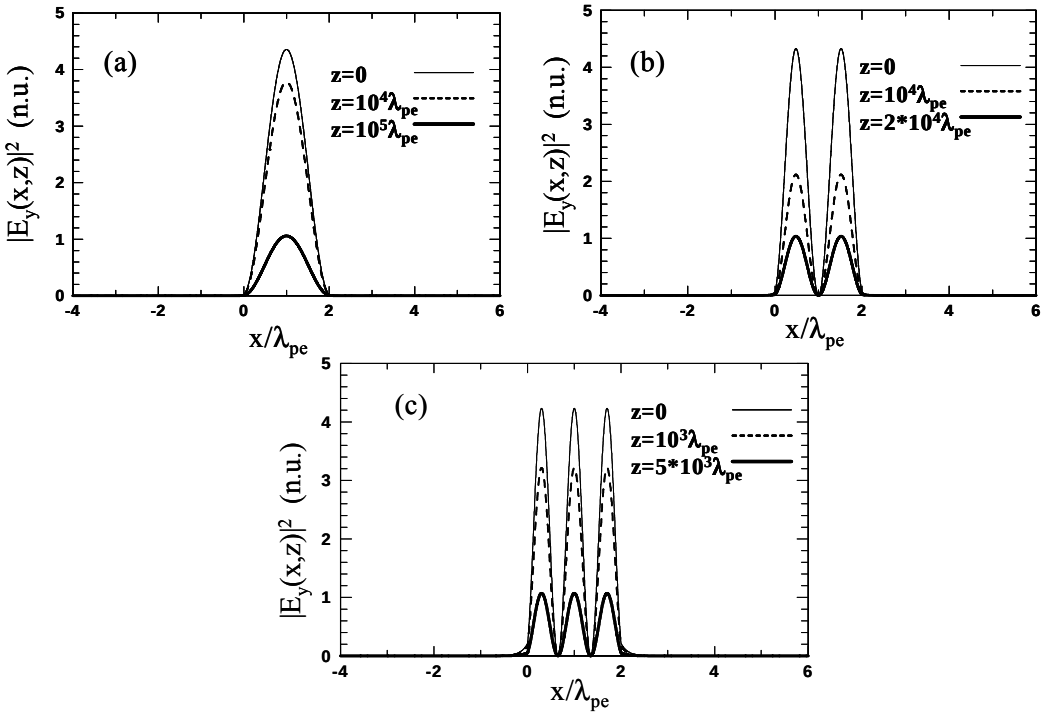

Fig. II-3. 2: Transverse profile of the TE guided modes at different propagation distances for a waveguide whose air core has a thickness $d=2\lambda_{pe}$,λ_{pe} $=2\pi c/\omega_{pe}$. The frequency of the field is $\omega=0.88\omega_{pe}$ (a) TE_0. (b) TE_1. (c) TE_2

In order to calculate the modes admitted by our waveguide, we have to solve Eq.(II-3. 4) for TE modes and the corresponding equation for TM modes. Eq.(II-3. 4) is a complex, transcendental equation that does not admit analytical solutions. It can be solved numerically by using the Newton-Rapson method [16]. Then, by using Eqs.(II-3. 3) and (II-3. 5) we can calculate the transverse mode profile for different propagation distances. In Fig.(II-3. 2) we show

TE guided modes for a waveguide whose core has thickness $d=2\lambda_{pe}$, where $\lambda_{pe}=2\pi c/\omega_{pe}$.. The electromagnetic field is approximately tuned at the center of the opaque region of the NIM, where $\omega=0.88\omega_{pe}$. The thickness of the core is in this case large enough to accommodate three confined modes at different angles: $\vartheta\cong15.9^0$ for TE_0, $\vartheta\cong33^0$ for TE_1, and $\vartheta\cong53.9^0$ for TE_2. In the case of the fundamental mode (TE_0), we find an attenuation length of approximately $L'\cong7*10^4\lambda_{pe}$ .Supposing that that the waveguide operates around 10μm, the attenuation length is approximately 0.7m, which corresponds to a loss factor of approximately 6dB/m.

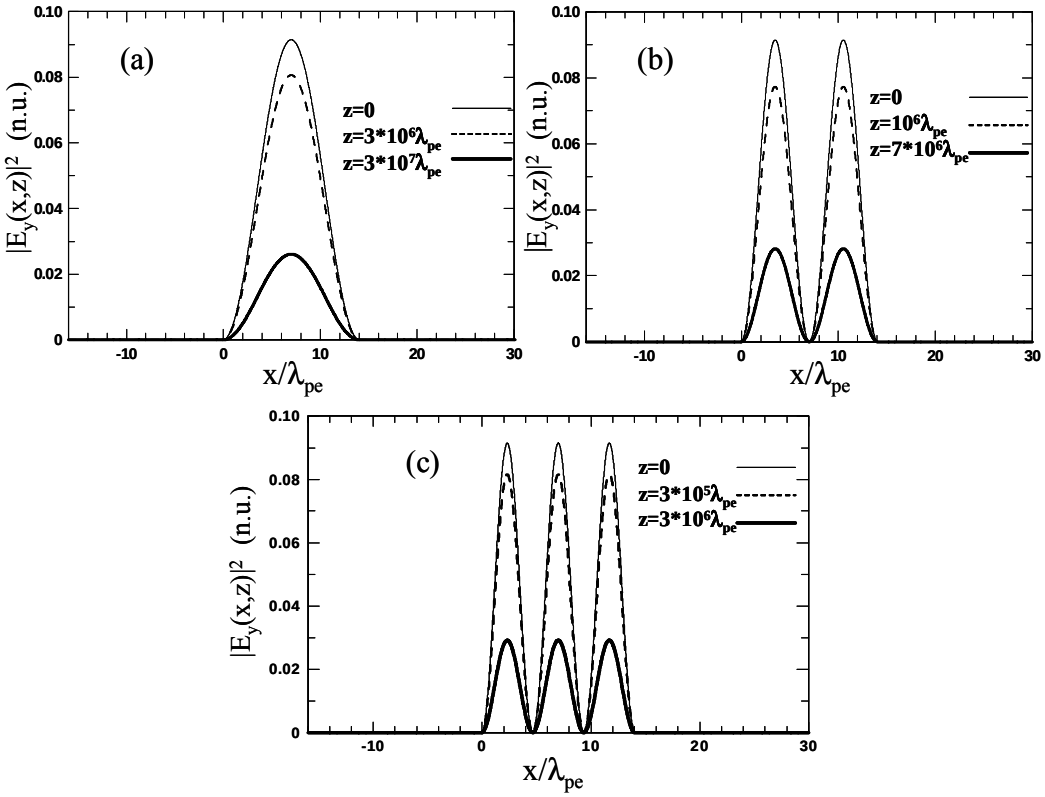

Fig. II-3. 3: Transverse profile of the first three TE guided modes at different propagation distances for a waveguide whose air core has a thickness $d=14\lambda_{pe}$. (a) TE_0. (b) TE_1. (c) TE_2

The losses drastically drop for larger core diameters, as shown in Fig.(II-3. 3), where the core is $d=14\lambda_{pe}$. In the case of Fig.(II-3. 3), for an operational wavelength around 10μm, the attenuation length of the TE_0 mode is approximately 240m, the losses are approximately 0.01dB/m, and the size of the air core is only 140μm. In this case the guide accommodates a large number of modes at different angles. The first three modes are excited respectively at $\vartheta\cong2.2^0$, $\vartheta\cong4.4^0$ and $\vartheta\cong6.6^0$. In Fig. (II-3. 4) we show the TM_0 mode for : a) $d=2\lambda_{pe}$ and b) $d=14\lambda_{pe}$. In the case of Fig. (II-3.

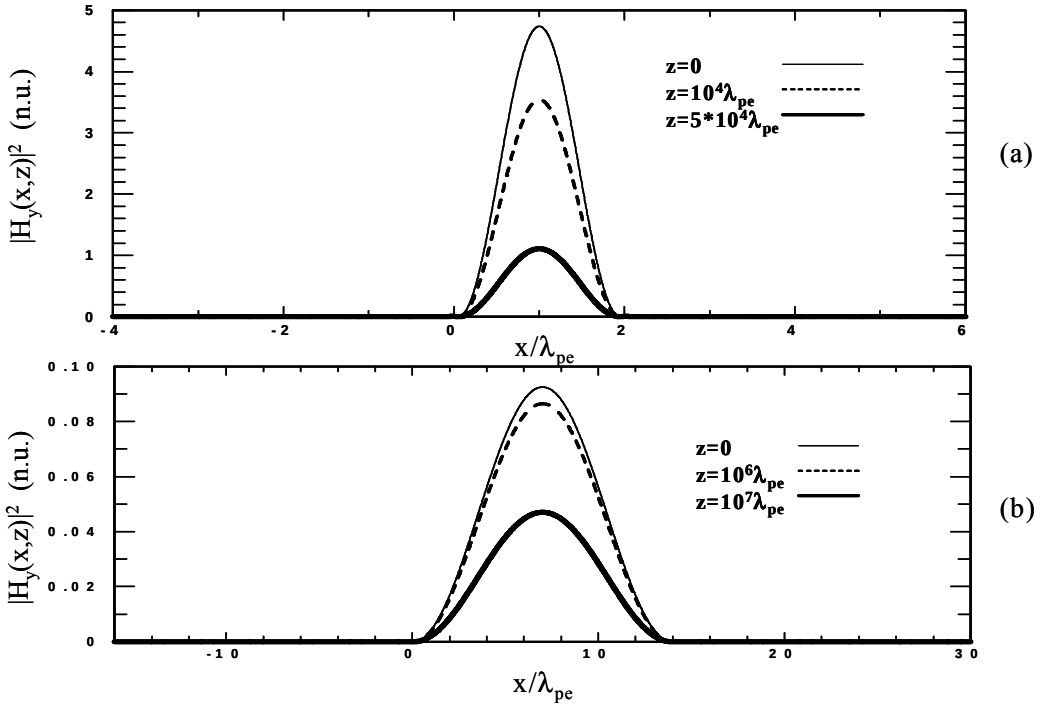

Fig. II-3. 4: Transverse profile of the TM_0 mode for different propagation distances. The waveguide has an air core of thickness respectively: (a) $d=2\lambda_{pe}$,(b) $d=14\lambda_{pe}$.

4a) the angle formed by the wavevector with the z-axis is $\vartheta\cong 17.3^0$ and the attenuation length is $L'\cong 3.4*10^4\lambda_{pe}$, which corresponds to approximately 12dB/m in losses for a wavelength of 10μm. In Fig. (II-3. 4b) $\vartheta\cong 2.3^0$, $L'\cong 1.4*10^7\lambda_{pe}$ and the losses are of the order of 0.03dB/m. Note that in the case we have studied the TE guided modes have longer attenuation lengths than the TM guided modes, and in the opaque region of the NIM Re(ε) is less than zero while Re(μ) is greater than zero. If we consider the opposite case, i.e. Re(ε) >0 and Re(μ)<0, the TM guided modes would have a longer attenuation length than the TE guided modes.

Finally we note that recently waveguides with an air core and a cladding made by a two-dimensional square array of silver nano-wires embedded in an air host medium have been numerically demonstrated to guide at optical frequency more efficiently than silver waveguides [17]: the effective extinction coefficient of the nano-structured cladding is smaller than that of a homogeneous silver cladding. In the case of Ref. [17] the effective index of the cladding can be made to vary in the range 0<n<1, depending on the ratio between the width of the silver wires and the periodicity of the array. Of course, a meta-material designed in this way is by definition not a NIM, and light refraction will be right handed as in standard positive index materials. In

this work we have instead explored the guiding properties of a NIM in its opaque region, i.e. in the region where its refractive index varies in the range $-10^{-2}<n<10^{-2}$.

Conclusions

In conclusion, we have studied a symmetric hollow waveguide made with a NIM cladding. In the opacity region of the NIM, the waveguide admits both TE and TM guided modes with relatively low losses. While further material development is still needed, recent advancements in the design of meta-materials suggest that this waveguide could operate in the infrared regime with better performances compared to more traditional hollow waveguides. Although, we have studied only planar waveguides we expect to find similar results also for cylindrical waveguides due to the intrinsic nature of the omnidirectional gap. The topic of cylindrical waveguides will be the subject of future investigation.

References and Notes

[1] A. Yariv, P. Yeh, "Optical Waves in Crystals", John Wiley& Sons, New York (1984)

[2] P.W. Smith, *Appl. Phys. Lett.* **19,** 132 (1971)

[3] T.J. Bridges, E.G. Burkhardt, and P.W. Smith, *Appl. Phys. Lett.* **20,** 403 (1972)

[4] P.K. Tien, R.J. Martin, and S. Riva-Sanseverino, *Appl. Phys. Lett.* **27, 251** (1975)

[5] E.A.J. Marcatili and R.A. Schmeltzer, *Bell Syst. Tech. J.* **43,** 1783 (1964)

[6] J.A. Harrington and C.C. Gregory, *Opt. Lett.* **15,** 541 (1990)

[7] J. Dai and J.A. Harrington, *Appl. Opt.* **36,** 5072 (1997)

[8] Y. Matsuura and M. Miyagi, *Appl. Opt.* **32,** 6598 (1993)

[9] J.C. Knight *et al.*,, *Science*, **282,** 1476 (1998)

[10] R.F Cregan *et al.*, *Science*, **285,** 1537 (1999)

[11] I.V. Shadrivov, A.A. Sukhorukov, and Y.S. Kivshar, *Phys. Rev E* **67,** 057602 (2003); Bae-Ian Wu *et al*., *Journ. Appl. Phys.* **93,** 9386 (2003)

[12] R.A. Shelby, D.R. Smith, and S. Schultz, *Science **292***, 77 (2001). [1] V.G. Veselago, *Sov. Phys. USPEKHI* **10**, 509 (1968).

[13] S. O' Brien and J. B. Pendry, *J. Physics: Condens. Matter* **14,** 6393 (2002)

[14] S. O'Brien, *et al.*, *Phys. Rev B* 69, 241101 (R) (2004), and references therein

[15] J. Pendry, *Opt. and Photon. News,* **15** , No9, 33 (2004)

[16] W.H. Press, B.P. Flannery, S.A. Teukolsky, and W.T. Vetterling, *Numerical Recipes in C,* (Cambridge Univ. Press, Cambridge,1988). In our case the Newton-Rapson procedure is initialized with a trial solution $\hat{\vartheta}_0$ that solves the following equation:

$$\tan\left(\frac{\omega}{c} n_0 d \sin\hat{\vartheta}_0\right) = \mathrm{Re}\left[-i\frac{\dfrac{2n_0\hat{n}\sin\hat{\vartheta}_0}{\mu}\sqrt{1-\dfrac{n_0^2}{\hat{n}^2}\cos^2\hat{\vartheta}_0}}{n_0^2\sin^2\hat{\vartheta}_0+\dfrac{\hat{n}^2}{\mu^2}-\dfrac{n_0^2}{\mu^2}\cos^2\hat{\vartheta}_0}\right].$$

[17] B.T. Schwartz and R. Piestun, *Appl. Phys. Lett.* **85,** 1 (2004).

II-4 Second Harmonic Generation in NIM/PIM Hetero-Structure

II-4.0 Introduction.

Using a Green function approach, we will study second harmonic generation in single and coupled cavities made of a generic, quadratic, positive index material (PIM) sandwiched between two negative index materials. Some of the linear and nonlinear properties of NIM/PIM cavities have been already studied: for example, in Ref [1] a PIM/NIM/PIM structure is studied; Ref [2] deals with finite and infinite one-dimensional photonic crystals (1-D PCs) made of a NIM/PIM unit cell; in Ref [3] and [4] omni-directional reflectance is predicted for NIM/PIM 1-D PCs; finally, in Ref.[5], the authors show how an optical diode can be realized with NIM/PIM stratifications. This study differs from the works cited above in that we focus on the region where the NIM displays its intrinsic gap, where the refractive index is approximately equal to zero as its magnitude changes sign, as discussed at length in Ref.[6].

II-4.1 Single Cavity.

We begin by studying the linear and nonlinear behavior of a single NIM/PIM cavity. The electric and magnetic responses of the NIM are modeled with a lossy Drude model [5]:

$$\varepsilon^{\mathrm{NIM}}(\tilde{\omega}) = 1 - \frac{1}{\tilde{\omega}(\tilde{\omega} + i\tilde{\gamma}_e)} \quad , \quad \mu^{\mathrm{NIM}}(\tilde{\omega}) = 1 - \frac{(\omega_{pm}/\omega_{pe})^2}{\tilde{\omega}(\tilde{\omega} + i\tilde{\gamma}_m)} , \qquad \text{(II-4. 1)}$$

where $\tilde{\omega} = \omega / \omega_{pe}$ is the normalized frequency, ω_{pe} and ω_{pm} are the respective electric and magnetic plasma frequencies, $\tilde{\gamma}_e = \gamma_e / \omega_{pe}$ and $\tilde{\gamma}_m = \gamma_m / \omega_{pe}$ are the respective electric and magnetic loss terms normalized with respect to the electric plasma frequency. Here we take $\omega_{pm}/\omega_{pe}=0.8$, and $\gamma_e/\omega_{pe}=\gamma_m/\omega_{pe}=10^{-4}$. As discussed at length in Refs.[6-8], the transmission spectrum of a single layer of NIM exhibits a gap with band-edge resonances around the electric and magnetic plasma frequencies that are very similar to those of a PBG structure. In our case, the gap of the single slab of NIM is located in the spectral range between $0.8 < \tilde{\omega} < 1$. Moreover, the width of the gap depends upon the separation of the electric and magnetic plasma frequencies, and its depth is related to the thickness of the layer [7]. Now, when we sandwich one layer of PIM between two layers of NIMs, a transmission resonance appears in the middle of the gap, similar to a defect-resonance of PBG structures.

In figure (II-4. 1) we plot the transmission spectrum of a cavity made with a single layer of non-dispersive PIM enclosed between two layers of NIM. The layers of NIM have thicknesses $a=2.5\lambda_{pe}$, while the PIM layer has thickness $d=0.16338\lambda_{pe}$, where $\lambda_{pe}=2\pi c/\omega_{pe}$ is the electric

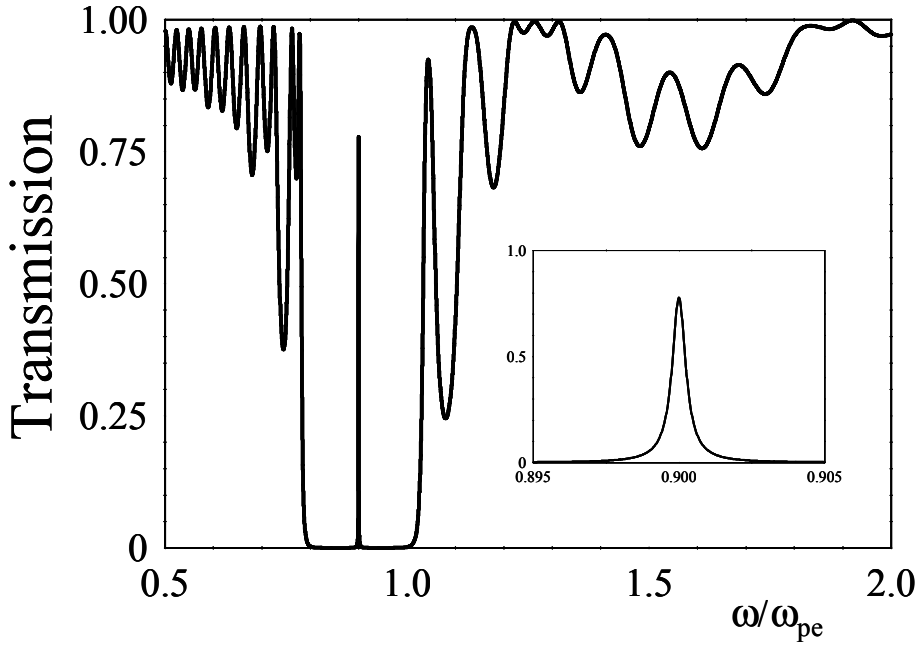

Fig. II-4. 1: Transmission spectrum of a NIM/PIM/NIM cavity vs ω/ω_{pe}. The thickness of each layer of NIM is $2.5\lambda_{pe}$, while the thickness of the PIM is $0.16338\lambda_{pe}$, $\lambda_{pe}=2\pi c/\omega_{pe}$ is the electric plasma wavelength. The PIM is assumed to be non dispersive and non-absorbing with a refractive index of n=1.4. Inset: magnification of the defect resonance inside the gap. The defect resonance is centered around $0.9\omega_{pe}$.

plasma wavelength. The thickness of the PIM has been chosen in order to have a transmission resonance at the frequency $\tilde{\omega}=0.9$, and its refractive index is assumed to be n=1.4. Note that at $\tilde{\omega}=1.8$, or double the frequency where the transmission resonance occurs, the curve is relatively smooth. In Figs (II-4. 2a) we choose $\tilde{\omega}=0.9$, and plot the transmission as a function of the PIM thickness. In Figs(II-4. 2b) and (II-4. 2c) we show magnifications of the first and second transmission resonances, which correspond to PIM layer thicknesses of $d=0.16338\lambda_{pe}$ (Fig. (II-4. 2b)) and $d=0.5602\lambda_{pe}$ (Fig. (II-4. 2c)) respectively. In Figs. (II-4. 3a) and (II-4. 3b) we show field localization inside the structure corresponding to the first and the second transmission resonances shown in Figs. (II-3. 2), respectively. As one may expect, the field intensity is single-peaked at the first transmission resonance, double-peaked at the second transmission resonance, and so on.

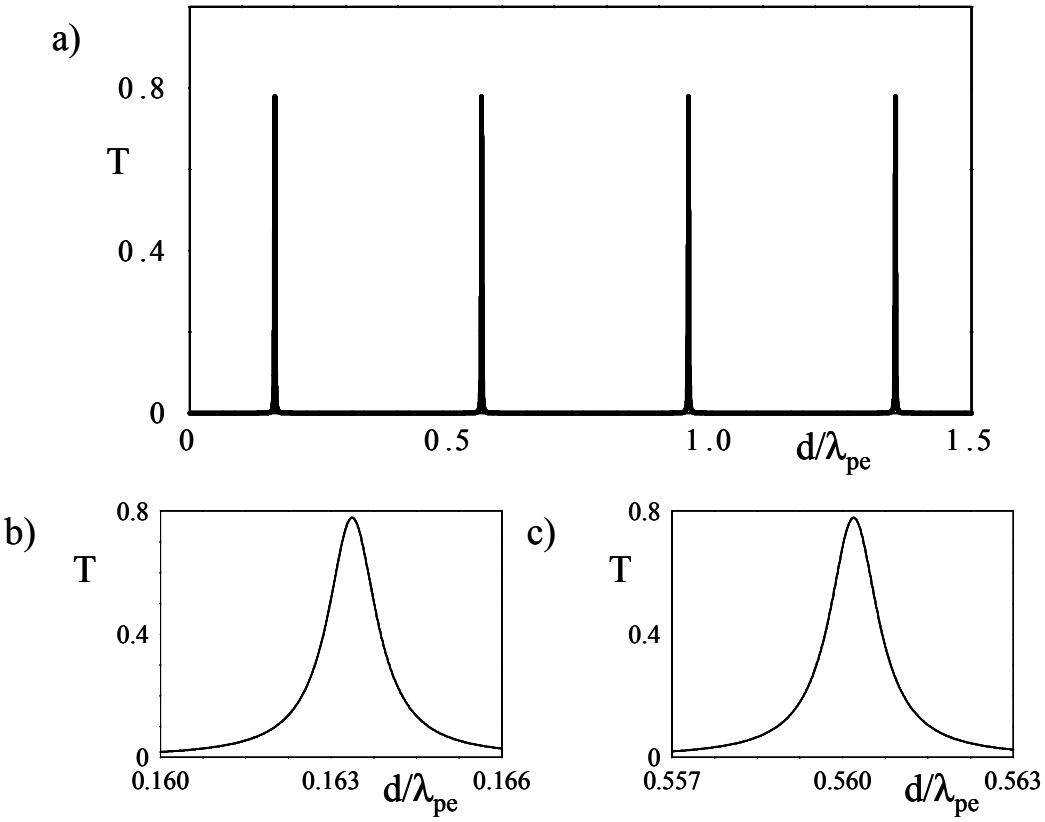

Fig. II-4. 2: a) Transmission vs. PIM thickness, for the NIM/PIM/NIM cavity described in Fig.1 at the frequency of $0.9\omega_{pe}$ that corresponds to the peak of the band gap transmission resonance in Fig.1. The thickness of the two NIM mirrors is fixed at $2.5\lambda_{pe}$. b) Magnification of the first transmission resonance around d= $0.16338\lambda_{pe}$. c) Magnification of the second transmission resonance around d= $0.5602\lambda_{pe}$..

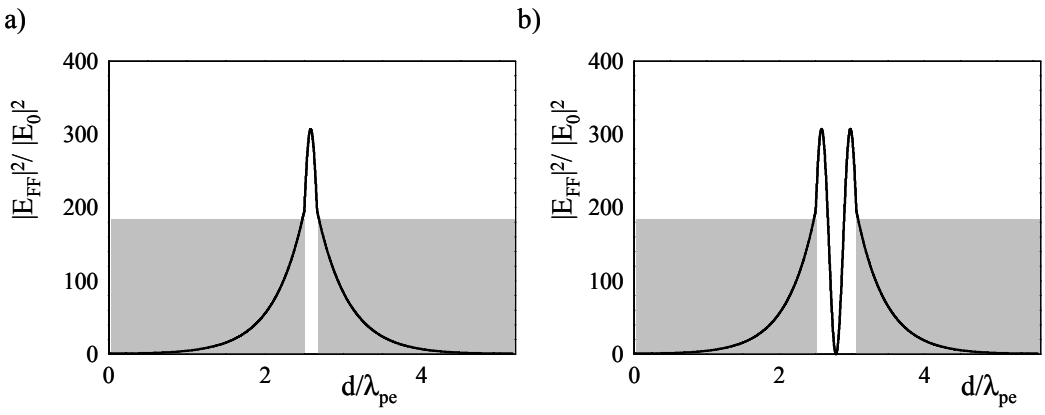

Fig. II-4. 3: Square modulus of the electric field for the NIM/PIM/NIM cavity at $0.9\omega_{pe}$ when a) the PIM thickness is $0.16638\lambda_{pe}$ and b) when the PIM thickness is $0.5602\lambda_{pe}$.

Let us go to the main focus of our study, i.e. second harmonic generation (SHG) in this cavity where only the PIM possesses a quadratic nonlinearity. Under the monochromatic, plane wave approximation, and for normal incidence, the Helmholtz equations that describe SHG in the NIM/PIM/NIM cavity are given by:

$$\frac{d^2E_\omega}{dz^2}+\frac{\omega^2\varepsilon_\omega(z)\mu_\omega(z)E_\omega}{c^2}=-2\frac{\omega^2}{c^2}\mu_\omega d^{(2)}(z)E_\omega^* E_{2\omega}, \qquad \text{(II-4. 2a)}$$

$$\frac{d^2E_{2\omega}}{dz^2}+\frac{(2\omega)^2\varepsilon_{2\omega}(z)\mu_{2\omega}(z)E_{2\omega}}{c^2}=-\frac{(2\omega)^2}{c^2}\mu_{2\omega}d^{(2)}(z)E_\omega^2, \qquad \text{(II-4. 2b)}$$

where $\varepsilon_{\omega,2\omega}$, $\mu_{\omega,2\omega}$ are respectively the z-dependent electric susceptibility and magnetic permeability at the fundamental (FF) and second harmonic (SH) frequency. $d^{(2)}$ is the quadratic coupling coefficient of the PIM: $\varepsilon_{\omega,2\omega}=\varepsilon_{\omega,2\omega}^{NIM}$, $\mu_{\omega,2\omega}=\mu_{\omega,2\omega}^{NIM}$, and $d^{(2)}=0$ for $0<z<a$ and $2a+d>z>a$; $\varepsilon_{\omega,2\omega}=\varepsilon_{\omega,2\omega}^{PIM}$, $\mu_{\omega,2\omega}=1$ and $d^{(2)}\neq 0$ for $a<z<a+d$, where a and d are the thicknesses of the NIM and PIM layers respectively, and $L=2a+d$ is the total length of the structure. In what follows we suppose that the structure is surrounded by air. Eqs. (II-4. 2) should be solved in each layer separately and then the solutions should be matched at the interfaces by using the boundary conditions appropriate to the case of magnetically active materials. In general, given the nonlinear nature of the equations, this computational task can be accomplished only numerically. In the undepleted pump regime, a fast and elegant way to proceed is to resort to the Green function approach. In that case, the formal expression for the electric fields that is valid inside the structure can be written as:

$$E_\omega(z)=A\Phi_\omega^+(z)+B\Phi_\omega^-(z) \quad , \qquad \text{(II-4. 3a)}$$

$$E_{2\omega}(z)=-4\frac{\omega^2}{c^2}\int_0^L G_{2\omega}(\xi,z)d^{(2)}(\xi)E_\omega^2(\xi)d\xi, \qquad \text{(II-4. 3b)}$$

where Φ_ω^+ and Φ_ω^- are the Right-to-Left (RTL) and Left-to-Right (LTR) linear modes of the structure at the FF as described in Refs [9-11]. RTL and LTR propagating modes can be calculated independently using a standard linear matrix-transfer technique [12] adapted to the case of magnetic active materials. In Eq.(II-4. 3a), A and B are complex coefficients that have the dimensions of an electric field. These coefficients are uniquely determined by the boundary conditions. In the special case of LTR incidence B is zero, while A is the complex amplitude of

the FF pump field incident from LTR. In Eq. (II-4. 3b), $G_{2\omega}$ is the Green function at frequency 2ω. The Green function can be calculated in term of the RTL and LTR propagating modes of the structure at frequency 2ω. In order to do so, the theory developed in references [10, 11] has been extended to magnetically active media (see appendix A for details).

Eq.(II-4. 3a) gives the generated electric SH field in all the space, and allows the calculation of the conversion efficiency (η). In the plane wave regime the conversion efficiency is defined as the sum of the forward and backward generated SH intensity divided by the input pump intensity:

$$\eta = \frac{I_{2\omega,\text{Backward}}^{\text{output}} + I_{2\omega,\text{Forward}}^{\text{output}}}{I_{\omega}^{\text{input}}} \qquad \text{(II-4. 4)}$$

where $I_{2\omega,\text{Backward}}^{\text{output}} = (1/2)\varepsilon_0 c\left|E_{2\omega}(0)\right|^2$ and $I_{2\omega,\text{Forward}}^{\text{output}} = (1/2)\varepsilon_0 c\left|E_{2\omega}(L)\right|^2$ in the case of a cavity embedded in air, and $I_{\omega}^{\text{input}}$ is the intensity of the pump beam incident from LTR. Now, taking into account Eqs. (II-4. 3a) and (II-4. 4), and using Eqs. (II-4. A4) and (II-3. A5) of the Appendix, we finally arrive to an expression for the conversion efficiency in term of overlap integrals [13]:

$$\eta = \frac{2\omega^2 L^2}{\varepsilon_0 c^3}\left(\left|\frac{1}{L}\int_0^L d^{(2)}(z)[\Phi_{\omega}^{+}(z)]^2\Phi_{2\omega}^{-}(z)dz\right|^2 + \left|\frac{1}{L}\int_0^L d^{(2)}(z)[\Phi_{\omega}^{+}(z)]^2\Phi_{2\omega}^{+}(z)dz\right|^2\right) I_{\omega}^{\text{input}}. \qquad \text{(II-4. 5)}$$

In Eq.(II-4. 5), two contributions to the conversion efficiency can be easily identified. The first integral refers to the forward conversion efficiency, while the second integral gives the backward conversion efficiency.

In Fig.(II-4. 4a) we plot the total conversion efficiency (forward+backward) as a function of the PIM thickness, when the pump is tuned to a frequency $\tilde{\omega} = 0.9$, and its intensity is 100MW/cm^2. The nonlinear coefficient is taken to be $d^{(2)}$=9pm/V. The conversion efficiency shows a series of peaks in correspondence to the transmission resonances shown in Fig.(II-4. 2a). In this case we have considered the quadratic material as being non dispersive. Note that the conversion efficiency grows approximately as the square of the length of the quadratic material, as one may expect for perfectly phase-matched interactions. For comparison, in Fig.(II-4. 4b) we plot the total conversion efficiency of a single layer of the same quadratic material as a function of its

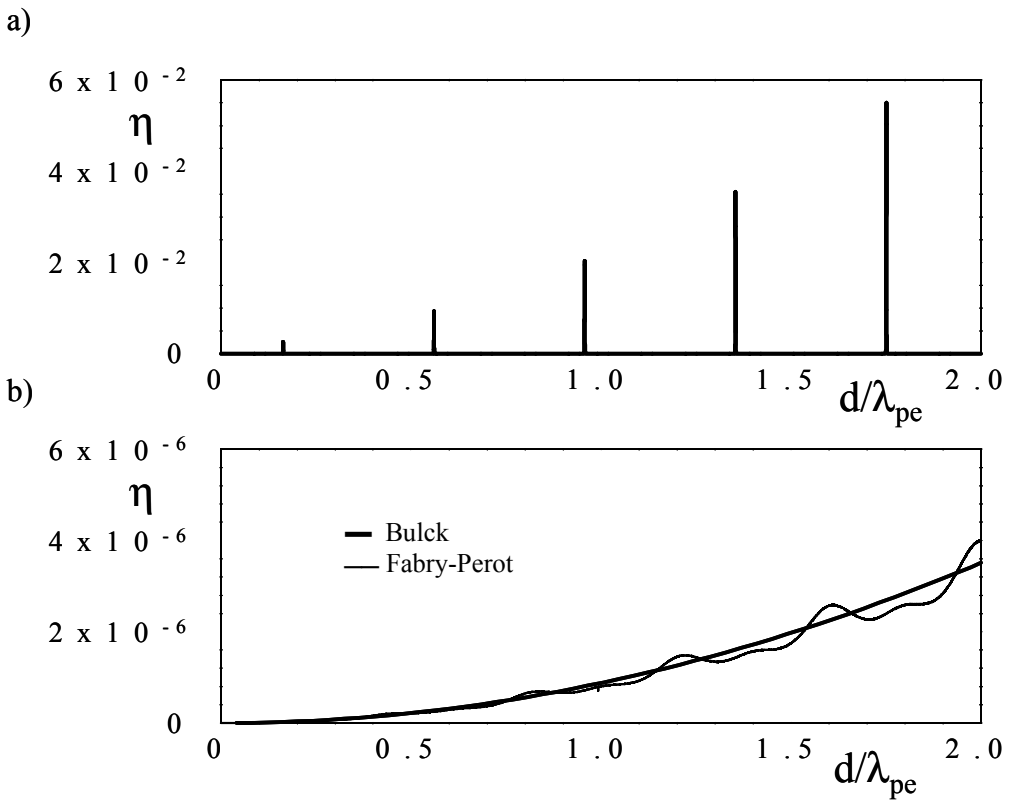

Fig. II-4. 4: a) Conversion efficiency (η) vs. PIM thickness for the NIM/PIM/NIM cavity. b) Conversion efficiency vs. thickness for a single layer of PIM. As explained in the text, the thin line refers to the conversion efficiency calculated considering the layer as a Fabry-Perot etalon, the thick line considering it as a bulk material.

thickness. The conversion efficiency of the single layer has been calculated in two different ways: a) considering it as a Fabry-Perot etalon with all interference effects taken into account (thin line) and b) considering it as a bulk material (thick line) using the standard formula for SHG in bulk materials [14]:

$$\eta = \frac{2\mu_0}{n_\omega^2 n_{2\omega} c}\left(d^{(2)}\omega L\right)^2 \frac{\sin^2(\Delta k d/2)}{(\Delta k d/2)^2} I_\omega^{input} \qquad \text{(II-4. 6)}$$

where L is the length of the quadratic material, $\Delta k = (2\omega/c)(n_{2\omega} - n_\omega)$ is the phase mismatch, in the case of Fig.(II-4. 4) $n_\omega = n_{2\omega} = 1.4$, and I_ω^{input} is the input intensity calculated in a medium that has the same refractive index of the quadratic material at the FF frequency. The NIM/PIM/NIM cavity shows an enhancement in the conversion efficiency by a factor of 10^4 with respect to the PIM layer. Moreover, in the case of the NIM/PIM/NIM cavity the calculations shows that the SH signal is generated almost perfectly balanced in the forward and backward directions.

Conversion efficiencies balanced in the forward and backward directions are typical of structures with high feedback, as discussed at length in Ref. [15] for the case of PBG structures. On the other hand, in the case of the single layer shown in Fig.(II-4. 4b), our calculations show that approximately 5% of the total conversion efficiency is generated in the backward direction. In Figs.(II-4. 5) we plot the generated SH field for the first and the second resonance shown in Figs.(II-4. 2).

Let us now investigate SHG outside of phase matching conditions. In Fig. (II-4. 6a) we plot

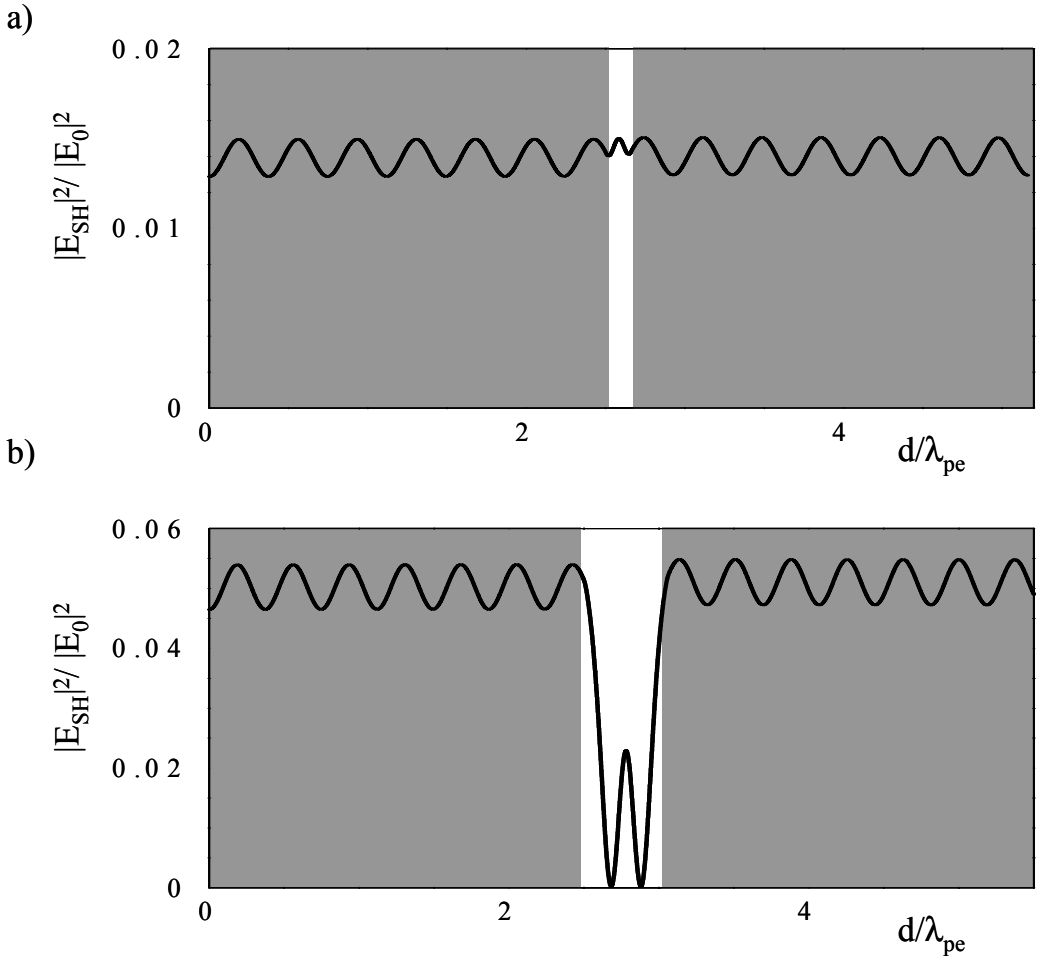

Fig. II-4. 5: Square modulus of the generated second harmonic electric field for a) PIM thickness of $0.16638\lambda_{pe}$ and b) PIM thickness is $0.5602\lambda_{pe}$. The pump field is tuned at $0.9\omega_{pe}$, i.e. at the transmission resonance in the band gap and its intensity is assumed to be 100 MW/cm^2 .The quadratic nonlinearity of the PIM layer is $d^{(2)}$=9pm/V . The PIM is assumed to be non dispersive and non-absorbing with a refractive index of 1.4.

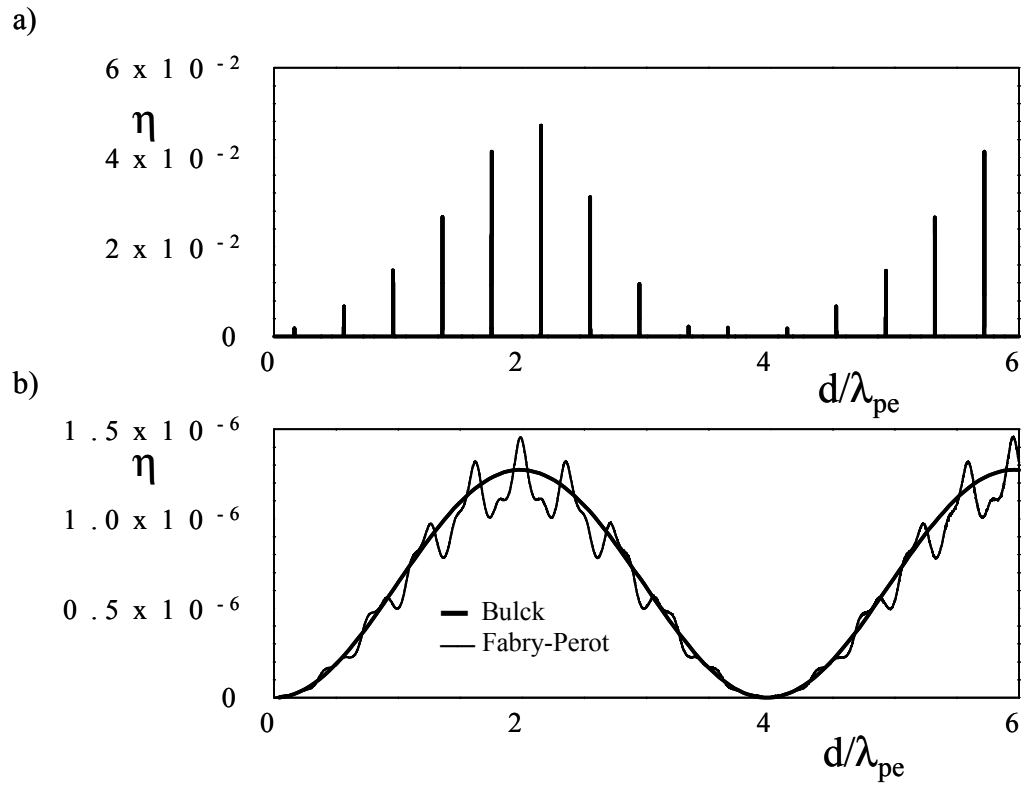

Fig. II-4. 6: a) Conversion efficiency (η) vs. PIM thickness as in Fig.(II-4. 4a) except that now the PIM is assumed to be dispersive with a 10% linear dispersion between the FF and the SH. b) Conversion efficiency vs. thickness for single layer of PIM. The thin and thick line refers respectively to the Fabry-Perot and bulk configuration as in Fig. (II-4. 5b).

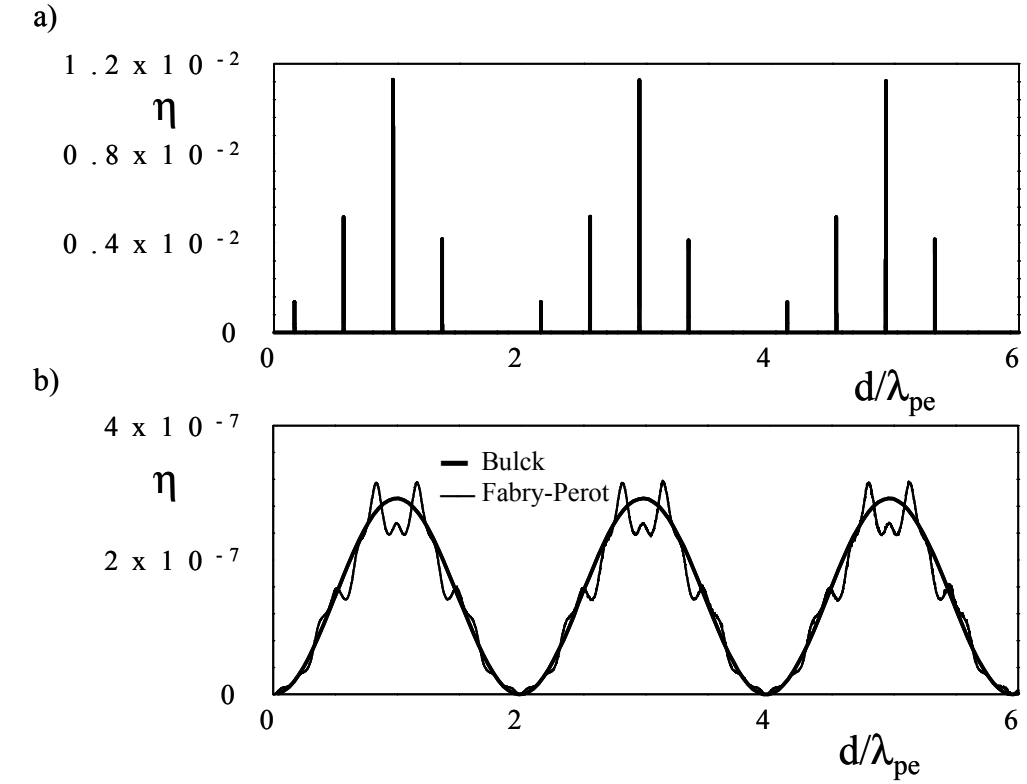

Fig. II-4. 7: Same as Figs.(II-4. 6) except that now the PIM is assumed to have a 20% dispersion.

the conversion efficiency of the NIM/PIM/NIM cavity as a function of the PIM thickness, and assuming a normal dispersion of 10% of the refractive index of the PIM at the SH frequency with respect to the refractive index at the FF, i.e. n_ω=1.4 and $n_{2\omega}$=1.54. In Fig. (II-4. 6b) we plot the conversion efficiency of a slab of the same PIM material as function of its thickness. As in Fig.(II-4. 4), the thin line corresponds to the conversion efficiency calculated assuming the PIM layer is a Fabry-Perot etalon, while the thick line is calculated using the bulk conversion efficiency Eq.(II-4. 6). In this case the coherence length of the PIM calculated from Eq.(II-4. 6) is $L_c=2\pi/\Delta k\cong 3.97\lambda_{pe}$. We note that the concept of coherence length is still valid in the case of the NIM/PIM/NIM cavity. In fact, comparing Fig.(II-4. 6a) and (II-4. 6b), it is evident that the conversion efficiency of the NIM/PIM/NIM cavity at the transmission resonances is approximately modulated by the function $\sin^2(\Delta kd/2)$. Comparing the SH energy generated from the NIM/PIM/NIM cavity to the SH generated in the single layer, our calculations show an enhancement factor of approximately 4×10^4. Once again we find that SH emission from the NIM/PIM/NIM cavity is balanced between the forward and backward directions, while in the single phase matched PIM layer SHG occurs almost completely in the forward direction. Finally, in Figs.(II-4. 7a) and (II-4. 7b) we plot the same quantities shown in figures (II-4. 6a) and (II-4. 6b), respectively, but now assuming a normal PIM dispersion of 20%. In this case the coherence length of the PIM calculated from Eq.(II-4. 6) drops to $l_c=2\pi/\Delta k\cong 1.98\lambda_{pe}$, and the enhancement factor is approximately 4×10^4. One may therefore conclude that while material dispersion is detrimental to the conversion efficiency of the single PIM layer, the NIM/PIM/NIM cavity conversion efficiency seems to benefit by as much as a factor of four as the amount of dispersion changes from 10% to 20% (see Figs. (II-4. 4), (II-4. 6), and (II-4. 7)).

II-4.2 Coupled Cavities.

Let us now investigate the case of coupled, multiple cavities, and let us first discuss some of their linear properties. When we add more layers, the defect resonance found at the center of the gap splits into several transmission resonances whose number equals the number of coupled cavities, as one may expect. In Fig. (II-4. 8) we show the transmission spectrum of a symmetric, 3 and 1/2 period structure, with initial and and final NIM layers (Fig.(II-4. 9)). The thickness of each NIM layers is a =$2.5\lambda_{pe}$, and the thickness of each PIM layer is d =$0.5602\lambda_{pe}$. The PIM is

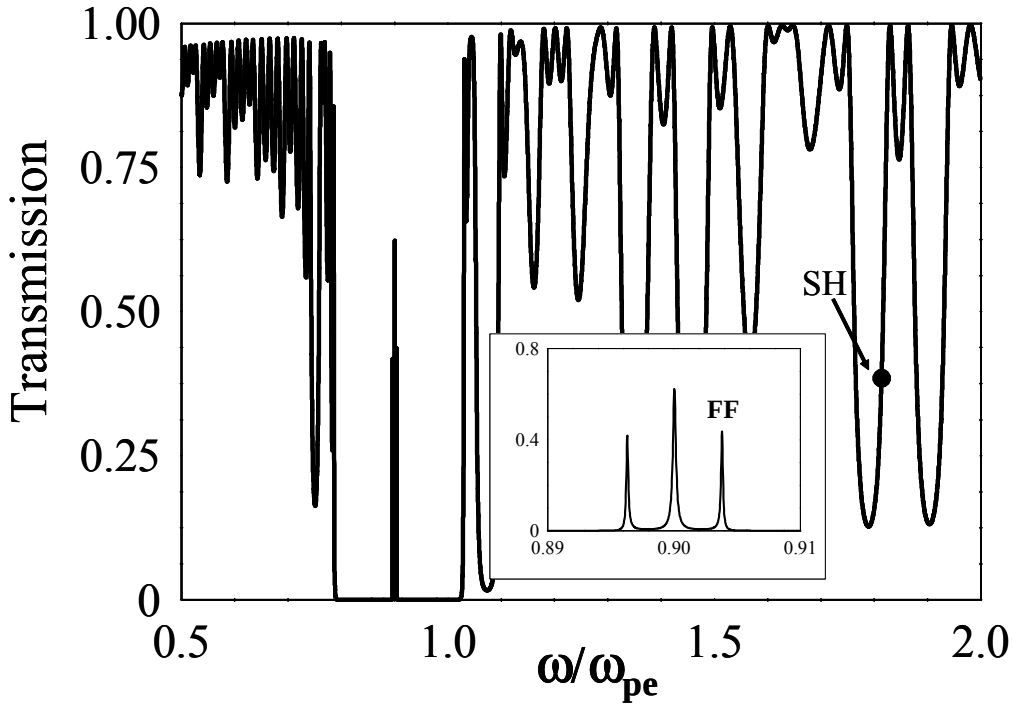

Fig. II-4. 8: Linear transmission of three coupled cavities, i.e. $(NIM/PIM)^3NIM$ with a 20% dispersion in the PIM and PIM thickness $d= 0.5602\lambda_{pe}$. The inset shows the three defect resonances that appear in the gap. The arrow indicates the tuning of the SH when the FF field is tuned at the third resonance.

assumed to be dispersive with a linear dispersion of 20% with respect to $\tilde{\omega} = 0.9$, i.e. $n(\tilde{\omega}) = 1.4 + (0.28/0.9)(\tilde{\omega} - 0.9)$. The dispersion relations for the NIM layers are the same as those used for the single cavity. The inset of Fig.(II-4. 8) shows the three defect resonances that appear inside the gap around $\tilde{\omega} = 0.9$. Note that the spectral position of the gap does not depend on the number of coupled cavities. In fact, the gap remains positioned in the spectral region between the electric and magnetic plasma frequencies, as for the case of the single cavity (see Fig.1). This fact confirms that the gap is intrinsic, i.e. it only depends on the dispersion relations of the NIM, not on any kind of interference effect from any of the layers, as it would for ordinary PBG structures made with PIMs [6-8], for example. Adding more cavities to the structure causes more transmission resonances to appear inside the gap, the transmission spectrum outside the gap become oscillates unpredictably, and SH emission is consequently much more difficult to control. For these reasons we focus our attention on the structure of Fig.(II-4. 8), which is formed by only three coupled cavities. In Fig. (II-4. 9) we plot the square modulus of the FF electric field tuned at the third transmission resonance inside the band gap of the structure. Note that the

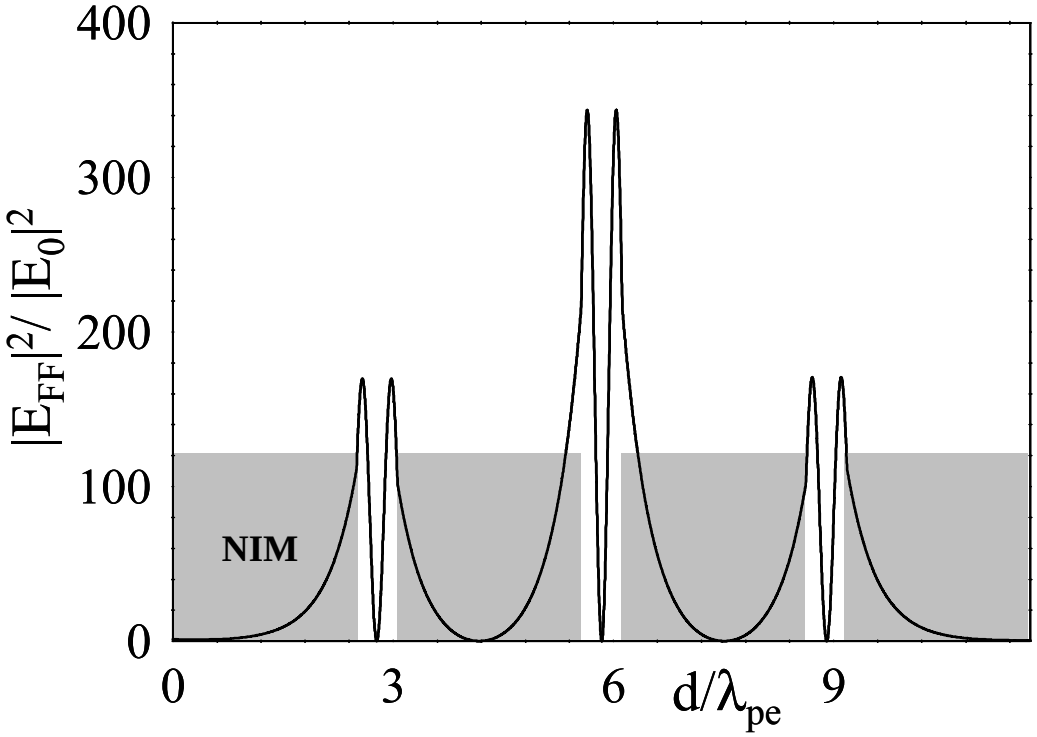

Fig. II-4. 9: Square modulus of the FF field when it is tuned at the third transmission resonance inside the band gap.

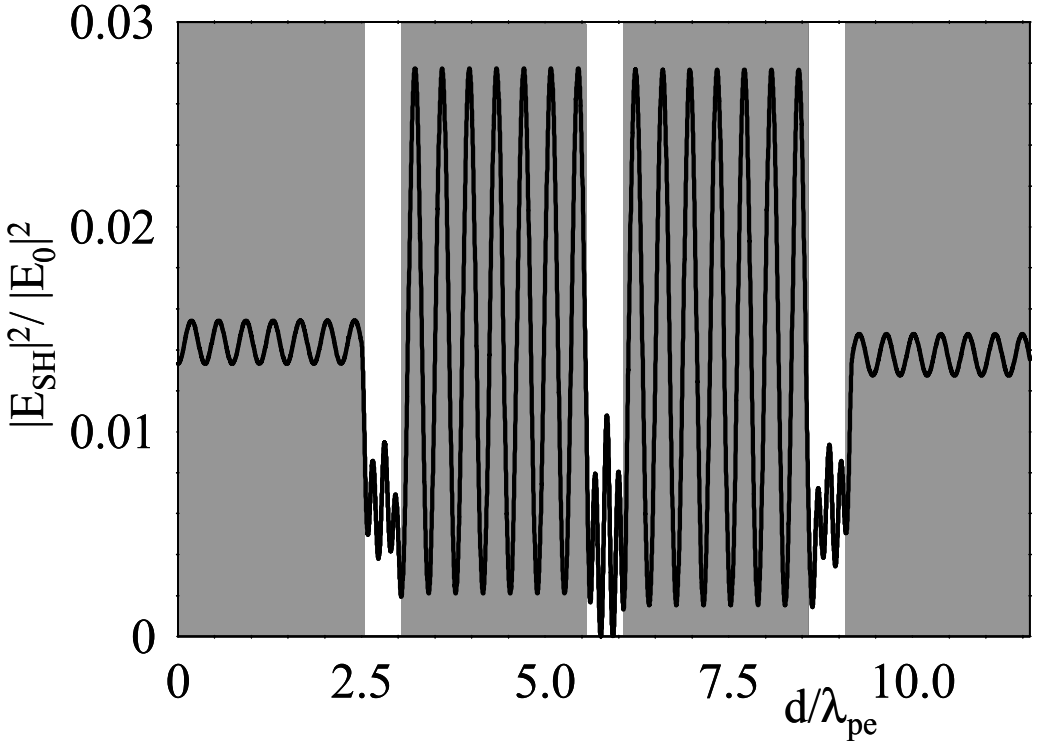

Fig. II-4. 10: Square modulus of the generated SH field for tuning conditions described in Fig. (II-3. 8). The pump intensity and the quadratic nonlinearity of the PIM arte the same used in the previous figures.

electric field profile inside the PIM layers is almost identical to the profile it has for the single cavity case (see Fig. (II-4. 3b)). In Fig.(II-4. 10) we plot the SH generated field when the FF is tuned to the third resonance peak. We find a conversion efficiency of 2.6 % with an input pump of 100MW/cm^2. We note that in the case of a single NIM/PIM/NIM cavity the maximum conversion efficiency available for the same intensity of input pump never exceeds 1.2% (see Fig.(II-4. 7a)). We have also calculated the conversion efficiency when the pump is tuned to the first and the second transmission resonances. Tuning to the first transmission resonance yields a conversion efficiency of 1.3%, while tuning to the second resonance peak is yields a conversion efficiency of 0.9%. The reasons the third resonance peak yields a higher conversion efficiency is due to a combination of higher field localization and better phase link for the FF and SH fields over the PIM layers; these conditions ultimately lead to a higher value of the square modulus of the overlap integrals calculated in Eq.(II-4. 5).

Conclusions.

In this paper we have explored the possibility of using NIMs as mirrors in the spectral region that contains an intrinsic gap, where the refractive index $n \cong 0$, in single or multiple coupled cavity configuration. Recent advancements in the field of metamaterials suggest that NIMs operating in the near infrared regime (~1.5μm) may be within reach [16-18], therefore suggesting that NIM/PIM/NIM single and multiple cavities may be exploited to obtain efficient SHG devices. From a more practical point of view, assuming a NIM operating around ~1.5μm, the defect resonances that appear in the intrinsic gap region may resolved with input pulses of temporal duration ~50ps÷100ps.

II-4.A Appendix A.

Let us consider Eq. (II-4. 2b) of the main text that here for the sake of clarity we write again:

$$\frac{d^2}{dz^2}E_{2\omega}+\frac{(2\omega)^2\varepsilon_{2\omega}(z)\mu_{2\omega}(z)E_{2\omega}}{c^2}=-\frac{(2\omega)^2}{c^2}\mu_{2\omega}(z)d^{(2)}E_{\omega}^2(z)\,. \qquad \text{(II-4. A1)}$$

In the undepleted pump approximation E_ω is a known function and therefore the term at the right hand side of Eq.(II-4. A1) acts as a source term. Because we are dealing with magnetic active materials, we associate to Eq.(II-4. A1) a Green function that satisfies the following equation:

$$\frac{\partial^2 G_{\omega}(z,\xi)}{\partial z^2}+\frac{(2\omega)^2\varepsilon_{2\omega}(z)\mu_{2\omega}(z)G_{\omega}(z,\xi)}{c^2}=\mu_{2\omega}(z)\delta(z-\xi), \qquad \text{(II-4. A2)}$$

where $\delta(z-\xi)$ is the so called "Dirac delta function that is in this case multiplied by the z-dependent magnetic permeability of the structure. As we will see later in this section, this is a more convenient choice when, as in this case, the problem is related to stratifications of magnetically active media. We can write the formal solution of Eq.(II-4. A1) as follows:

$$E_{2\omega}(z)=-4\frac{\omega^2}{c^2}\int_0^L G_{2\omega}(\xi,z)d^{(2)}(\xi)E_{\omega}^2(\xi)d\xi\,. \qquad \text{(II–4. A3)}$$

The Green function $G_{2\omega}(z,\xi)$ must be continuous at all points of the interval $0\le z\le L$ except at the point $z=\xi$, where it must have a jump equal to $\mu(z)$ in its first derivative. The calculation of the Green functions follows formally the same steps outlined in Ref.[11] with the only two differences: a) the jump in the derivative of the Green function at $z=\xi$ must be $\mu(z)$ and not 1 as it would be the case for non magnetic material and b) the boundary conditions appropriated for magnetic active materials must be applied. Following Ref.[11], Eq. (II-4. A2) can be solved in term of the RTL and LTR propagating modes of the structure at frequency 2ω:

$$G_{2\omega}(z,\xi)=\begin{cases}\dfrac{1}{W}\Phi_{2\omega}^{(+)}(\xi)\Phi_{2\omega}^{(-)}(z) & 0\le z<\xi\\[2ex] \dfrac{1}{W}\Phi_{2\omega}^{(-)}(\xi)\Phi_{2\omega}^{(+)}(z) & L\ge z>\xi\end{cases}, \qquad \text{(II-4. A4)}$$

where W is a conserved quantity, i.e. dW/dz=0, given by:

$W = W\left(\Phi_\omega^{(-)}, \Phi_\omega^{(+)}\right) \equiv \begin{vmatrix} \Phi_\omega^{(-)} & \Phi_\omega^{(+)} \\ \frac{1}{\mu} d\Phi_\omega^{(-)}/dz & \frac{1}{\mu} d\Phi_\omega^{(+)}/dz \end{vmatrix}$. Note that in the case of non magnetic materials, i.e. $\mu(z)=1$, W would be the Wronskian of the fundamental set of solutions. Now using the condition that W is a conserved quantity, it can be calculated using the boundary conditions at z=L or z=0:

$$W = i\frac{n_{0,2}}{\mu_{0,2}}(2\omega)t_{2\omega}^{LTR} = i\frac{n_{0,1}}{\mu_{0,1}}(2\omega)t_{2\omega}^{RTL}, \qquad \text{(II-4. A5)}$$

where $n_{0,1,2}$ and $\mu_{0,1,2}$ are the refractive index and the magnetic permeability of the materials surrounding the structure; $t_{2\omega}^{LTR}$ and $t_{2\omega}^{RTL}$ are respectively the linear transmission coefficient of the structure for an incident field from LTR and RTL respectively.

References and Notes

[1] Keunhan Park, Bong Jae Lee, Ceji Fu, and Zhuomin M. Zhang J. Opt. Soc. Am. B **22**, 1016 (2005)

[2] D.R. Fredkin, A. Ron, Appl. Phys. Lett. **81**,.1753 (2002).

[3] H. Jiang, H. Chen, H. Li, and Y. Zhang, S. Zhu, Appl. Phys. Lett. **83**,.5386 (2003).

[4] D. Bria, B. Djafari-Rouhani, A. Akjouj, L. Dobrzynski, J. P. Vigneron, E. H. El Boudouti, and A. Nougaoui Phys. Rev. E **69**, 066613 (2004).

[5] Michael W. Feise, Ilya V. Shadrivov, and Yuri S. Kivshar, Phys. Rev. E **71**, 037602-1 (2005)

[6] G. D'Aguanno, N. Mattiucci, M. Scalora, M.J. Bloemer, Phys Rev. Lett. **93** 213902 (2004).

[7] G. D'Aguanno, N. Mattiucci, M. Scalora, and M.J. Bloemer, Laser Physics **15**, 590 (2005)

[8] G. D'Aguanno, N. Mattiucci, M. Scalora, M.J. Bloemer, Phys Rev. E **71** 046603 (2005).

[9] G. D'Aguanno, M. Centini, M. Scalora, C. Sibilia, M. Bertolotti, M. J. Bloemer, and C. M. Bowden, J. Opt. Soc. Am. B **19**, 2111-2121 (2002).

[10] O.Di Stefano, S. Savasta, and R. Girlanda, J.Mod.Opt **48**, 67-84 (2001).

[11] G. D'Aguanno, N. Mattiucci, M. Scalora, M. J. Bloemer, and A. M. Zheltikov, Phys. Rev. E **70**, 016612 (2004)

[12] J. Lekner Journal of Optical Society of America A **11**, 2892 (1994)

[13] It is worth to note that an expression for SH conversion efficiency that involves overlap integrals has also been obtained in our Ref.[9] through a multiple scale expansion approach, see in particular Eqs.(16a) and (16b). While the two approaches give very similar results, in the case of Ref.[9] the formula for SH conversion efficiency also involve the calculation of the average of the momentum operator of the electromagnetic field that is coupled with the overlap integrals. There are two main advantages in using the Green's function approach instead of the multiple scale expansion approach to calculate SH conversion efficiency: a) it does not relay on the existence of a fast and a slow scale of variation of the involved fields; b) it only involves the calculation of overlap integrals and not that of the momentum operator and therefore a much simpler expression can be obtained.

[14] A. Yariv, P. Yeh, “Optical Waves in Crystals” John Wiley & Sons, New York 1984.

[15] G. D’Aguanno, M. Centini, M. Scalora, C. Sibilia, M. Bertolotti, C. M. Bowden, M. J. Bloemer, Phys. Rev. E **67**, 016606 (2003).

[16] J. Pendry, Opt. and Photon. News, **15,** No9, 33 (2004)

[17] S. Linden, C. Enkrich, M. Wegener, J. Zhou, T. Koschny, C.M. Soukoulis., Science **306,** 1351 (2004).

[18] Podolskiy, A.K. Sarychev, V.M. Shalev, Opt. Express **11**,735 (2003).

II-5 Dark and bright gap solitons in a negative index Fabry-Perot etalon with a $\chi^{(3)}$ nonlinearity.

II-5.0 Introduction

We predict the existence of bright and dark gap solitons in a single slab of negative index material. The formation of gap solitons is made possible by the exceptional interplay between the linear dispersive properties of the negative index etalon and the effect of a cubic nonlinearity. The presence of a cubic (Kerr) nonlinearity in structures characterized by a periodic variation of the linear refractive index leads to the formation of localized electromagnetic modes in spectral regions that otherwise would just allow evanescent modes. These localized modes are generally referred to as gap solitons (GS) [1]. GS have attracted the attention of many researchers for almost two decades, beginning with the theoretical predictions of Chen and Mills for one-dimensional (1-D) photonic lattices with a Kerr nonlinearity [1]. Subsequently GS have been studied both theoretically [2] and experimentally [3], and their existence has also been predicted in 1-D periodic media with shallow gratings and a quadratic nonlinearity [4]. GS in 2D and 3D photonic crystals (PCs) have also been theoretically studied using different mathematical approaches [5].

We will show that the presence of bright and dark GS is supported in a single slab of material. This surprising outcome is borne out of the peculiar dispersive properties of NIMs [6-8]. NIMs' most impressive property is their ability to refract light in the opposite way with respect to what an ordinary material does. Very recently, nonlinear effects in NIMs have been also investigated [9]. While it is not surprising that a single slab of frequency dispersive material together with a cubic nonlinearity can support soliton waves in general, what it is surprising is that in this case the *single slab appears to support both bright and dark GS*.

Before going into details, it is worth to say a few words to define the terms "bright" and "dark" GS in the case of NIMs. By the term "bright GS" in NIMs we refer to a highly localized electromagnetic mode with approximately decaying tails excited inside the gap of a NIM (see Figs. (II-5. 3b) and (II-5.3c)). These modes have localization properties similar to the classical GS excited in the gap of distributed feedback structures with a cubic nonlinearity [1-3]. We emphasize that the formation of the gap in the NIM is due to the peculiar dispersive properties of the bulk of the material, while the formation of the gap in distributed feedback structures is due

to interference effects. On the other hand, the physical mechanism that leads to the formation of bright GS in both cases is the same: a dynamical change in the refractive index of the material occurs due to the presence of a cubic nonlinearity that shifts the position of the band gap, and allows the formation of localized modes in a spectral region that would otherwise support only evanescent modes. While "bright GS" in NIMs are localized over the structure in way similar to GS in distributed feed-back structures, in contrast "dark GS" are excited in the gap of a NIM in the form of delocalized modes, with approximately non-decaying tails. These states display a low intensity at the center of the structure, and a high intensity at the edges (see Fig.(II-5. 5c)). We note that contrary to bright GS, the intensity inside the structure never exceeds 1 with respect to a unitary input intensity. Therefore, dark GS have no counterpart in the case of the structures studied in Ref.[1-4]. Dark solitons generated at frequencies outside the gap or in other systems where there is no photonic band gap structure are not uncommon. For example, light waves in the form of dark solitons appear in optical fibers operating in the normal dispersion regime [10], in Raman scattering [11], and atomic, out-of-gap dark soliton waves are supported in a Bose-Einstein condensate interacting with a periodic optical field [12]. In contrast, *here we present numerical evidence that dark solitons can also occur when the incident light frequency is tuned inside the photonic band gap of a NIM.*

II-5.1 Results and discussion

We will describe the effective electric susceptibility and magnetic permeability of a NIM with a lossy Drude model [13]:

$$\varepsilon(\tilde{\omega}) = 1 - \frac{1}{\tilde{\omega}(\tilde{\omega} + i\tilde{\gamma}_e)} \quad , \quad \mu(\tilde{\omega}) = 1 - \frac{(\omega_{pm}/\omega_{pe})^2}{\tilde{\omega}(\tilde{\omega} + i\tilde{\gamma}_m)}, \qquad \text{(II-5. 1)}$$

where $\tilde{\omega} = \omega/\omega_{pe}$ is the normalized frequency, ω_{pe} and ω_{pm} are the respective electric and magnetic plasma frequencies, $\tilde{\gamma}_e = \gamma_e/\omega_{pe}$ and $\tilde{\gamma}_m = \gamma_m/\omega_{pe}$ are the respective electric and magnetic loss terms normalized with respect to the electric plasma frequency.

In Fig. (II-5. 1a) we show the refractive index and the extinction coefficient for a NIM with $\omega_{pm}/\omega_{pe} = 0.8$ and $\tilde{\gamma}_e \approx \tilde{\gamma}_m \approx 4.5*10^{-4}$. The refractive index *n* and the extinction coefficient β of the material are given by: $n + i\beta = \pm\sqrt{\varepsilon\mu}$. The sign in front of the square root must be chosen in a way that ensures the Poynting vector of the light refracted into a semi-infinite slab of NIM will always be directed away from the interface into the refracting material itself. Of course, only

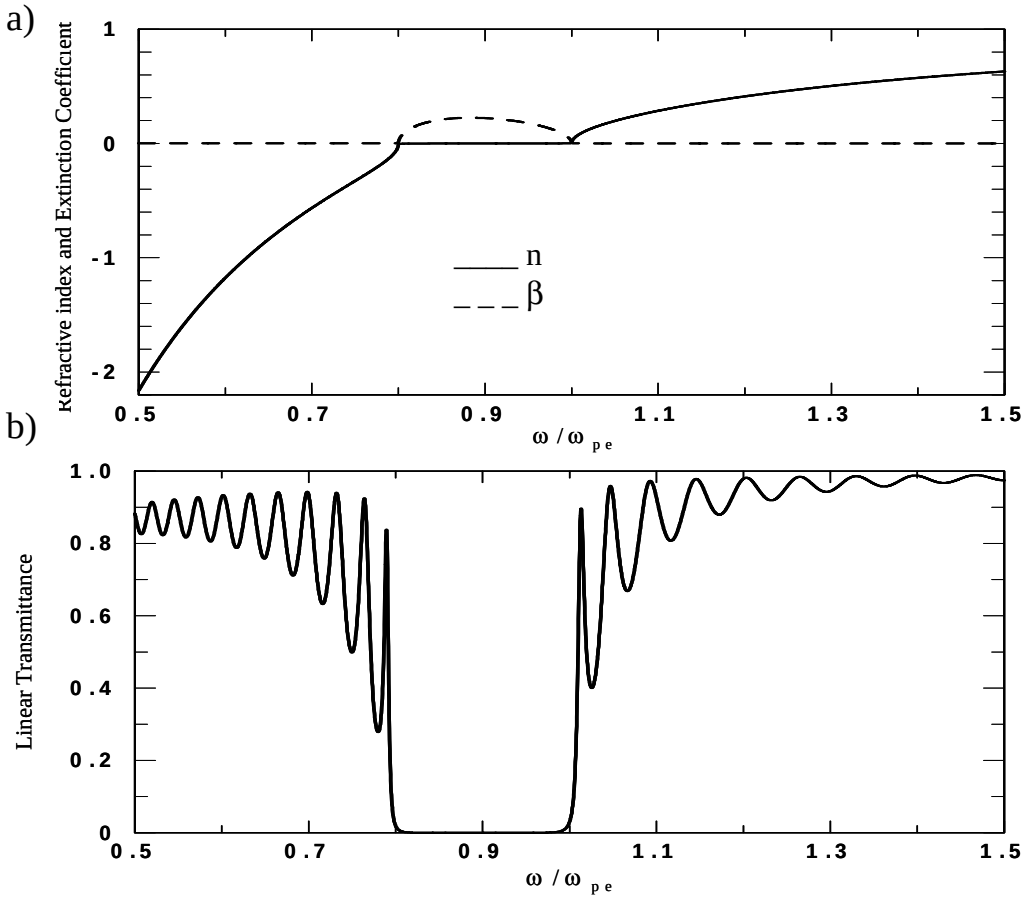

Fig. II-5. 1: a) Refractive index (solid line) and extinction coefficient (dashed line) vs. normalized frequency (ω/ω_{pe}) for a NIM with $\omega_{pm}/\omega_{pe} = 0.8$ and $\tilde{\gamma}_e \approx \tilde{\gamma}_m \approx 4.5*10^{-4}$. **b)** Linear transmittance vs. normalized frequency (ω/ω_{pe}) for a Fabry-Perot etalon of length $L=5\lambda_{pe}$ where $\lambda_{pe}=2\pi c/\omega_{pe}$ is the wavelength corresponding to the electric plasma frequency.

one of the two possible solutions of the square root satisfies this requirement. In Fig. (II-5. 1b) we show the linear transmission property of a Fabry-Perot (FP) etalon made by the same NIM.

Fig. (II-5. 1b) shows that the transmission spectrum of the FP etalon is similar to the transmission spectrum that occurs in structures that have a periodic variation of the refractive index. The center-gap frequency $\omega_{c,gap}$ and the spectral width of the gap $\Delta\omega_{gap}$ depend on the electric and magnetic plasma frequency as follows: $\omega_{c,gap} = (\omega_{pe} + \omega_{pm})/2$ and $\Delta\omega_{gap} = |\omega_{pe} - \omega_{pm}|$. The only gap that forms disappears when $\omega_{pe}=\omega_{pm}$. Moreover, the gap appears in the region where values of the refractive index *n* are near zero.

Let us now suppose the FP possesses a Kerr nonlinearity. The Helmholtz equation that governs the nonlinear dynamic at normal incidence is given by:

$$\frac{d^2E}{dz^2}+\frac{\omega^2}{c^2}\varepsilon\mu E=-\frac{\omega^2}{c^2}\mu\chi^{(3)}\left|E\right|^2E\,, \qquad \text{(II-5. 2)}$$

where ε and μ are the effective electric susceptibility and magnetic permeability given by Eq.(II-5. 1), $\chi^{(3)}$ is the coefficient of the cubic nonlinearity. The boundary conditions that apply to

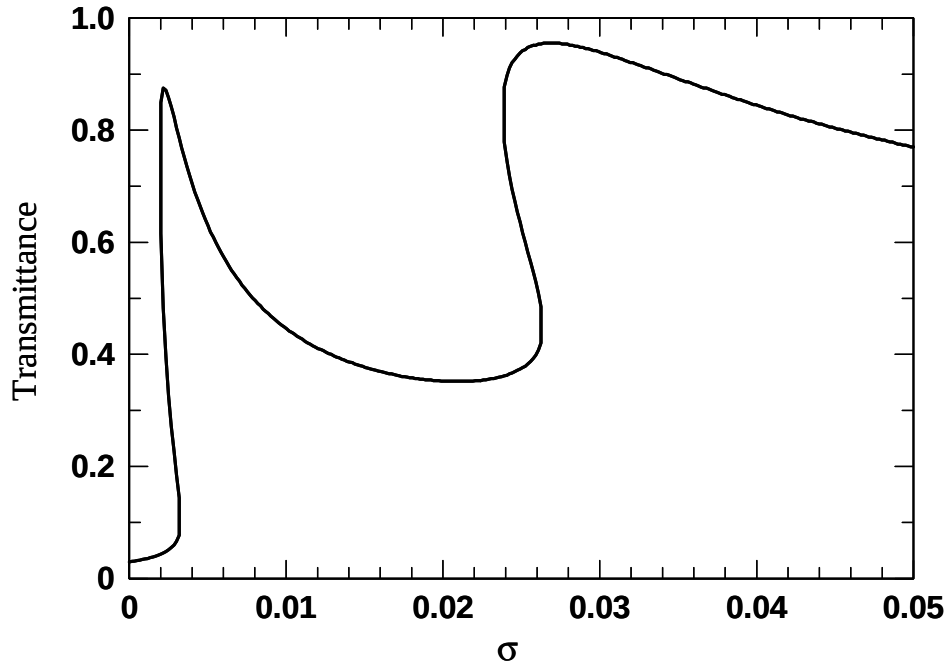

Fig. II-5. 2: Transmittance vs. control parameter $\sigma=\chi^{(3)}\left|E^{(input)}\right|^2$. The input field is tuned at $\omega_0=\omega_{pe}$ in the band gap near the high frequency band edge.

Eq.(II-5. 2) are those valid in the case of normal incidence in a magnetic material. Eq.(II-5. 2) has been numerical integrated using an explicit method in conjunction with a shooting procedure [14]. In Fig. (II-5. 2) we show the transmission of the FP etalon as function of the control parameter $\sigma=\chi^{(3)}\left|E^{(input)}\right|^2$, where $E^{(input)}$ is the input field. The input field is tuned at $\omega_0=\omega_{pe}$, i.e. inside the band-gap near the high frequency band edge. At $\omega_0=\omega_{pe}$ the refractive index, the extinction coefficient, and the magnetic permeability are: $n\cong 9.4*10^{-3}$; $\beta=9*10^{-3}$; $\mu=3.6*10^{-1}+i\,3*10^{-4}$, respectively. The figure shows bistable behavior that is typical of distributed feedback structures with a cubic nonlinearity [1, 15]. In Figs.(II-5. 3) we calculate the field localization

over the FP cavity for different values of the control parameter σ. In the linear case (σ=0, Fig.(II-5. 3a)), the field is evanescent, consistent with its tuning inside the bandgap. For σ=0.0039 the

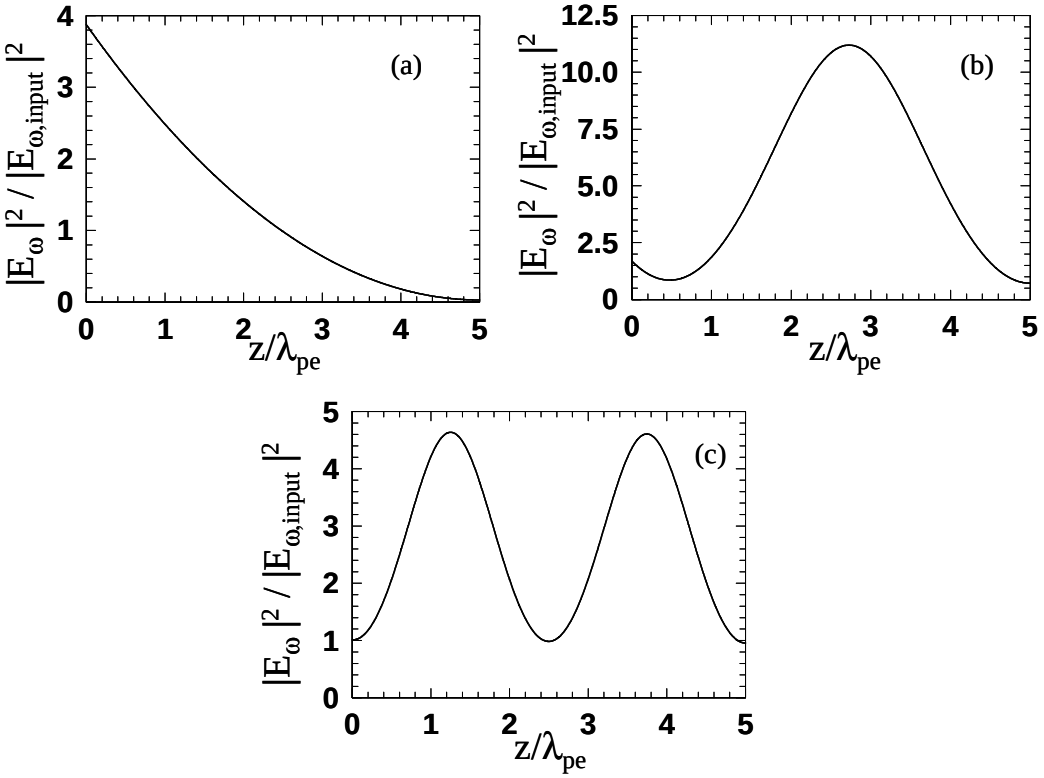

Fig. II-5. 3: Field localization in the cavity for different values of the control parameter: **(a)** σ=0 , **(b)** σ=0.0039, **(c)** σ=0.027.

field becomes localized in the form of a single bright soliton envelope, similar to that reported in reference [1]. For σ=0.027 a two-peaked, localized, bright-soliton state is excited.

The FP etalon also supports dark solitons. These states manifest themselves when the carrier frequency is tuned inside the gap, but now near the low frequency band edge. In Fig.(II-5. 4) we show the transmission as a function of the control parameter σ, for an input field tuned at $\omega_0=0.81\omega_{pe}$. In this case, the transmission shows multi-stable behavior. By increasing the value of the control parameter up to $\sigma=5$, three stable branches are found. The first branch is located in the range $0 \le \sigma \le 1.5$, and it corresponds to evanescent-type solutions as those shown in Fig. (II-5. 5a). The second branch is in the range $1.5 \le \sigma \le 2.61$, and the corresponding solutions are of the type shown in Fig. (II-5. 5b). Finally for $\sigma \ge 2.61$ dark soliton-type solutions are excited

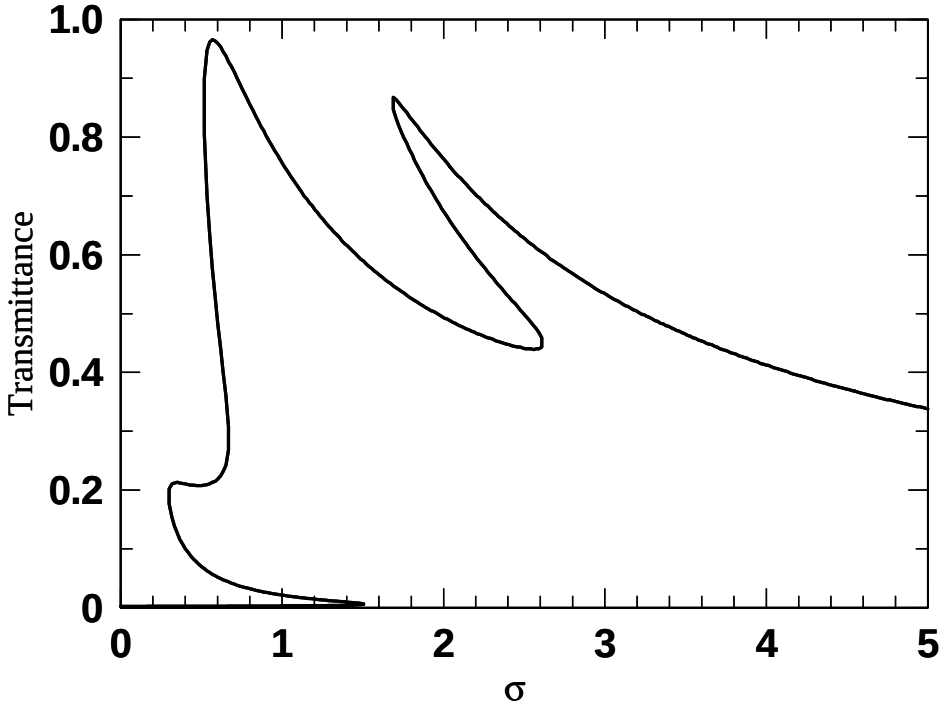

Fig. II-5. 4: Transmittance vs. control parameter $\sigma = \chi^{(3)}\left|E^{(input)}\right|^2$. The input field is tuned at $\omega_0=0.81\omega_{pe}$ in the band gap near the low frequency band edge.

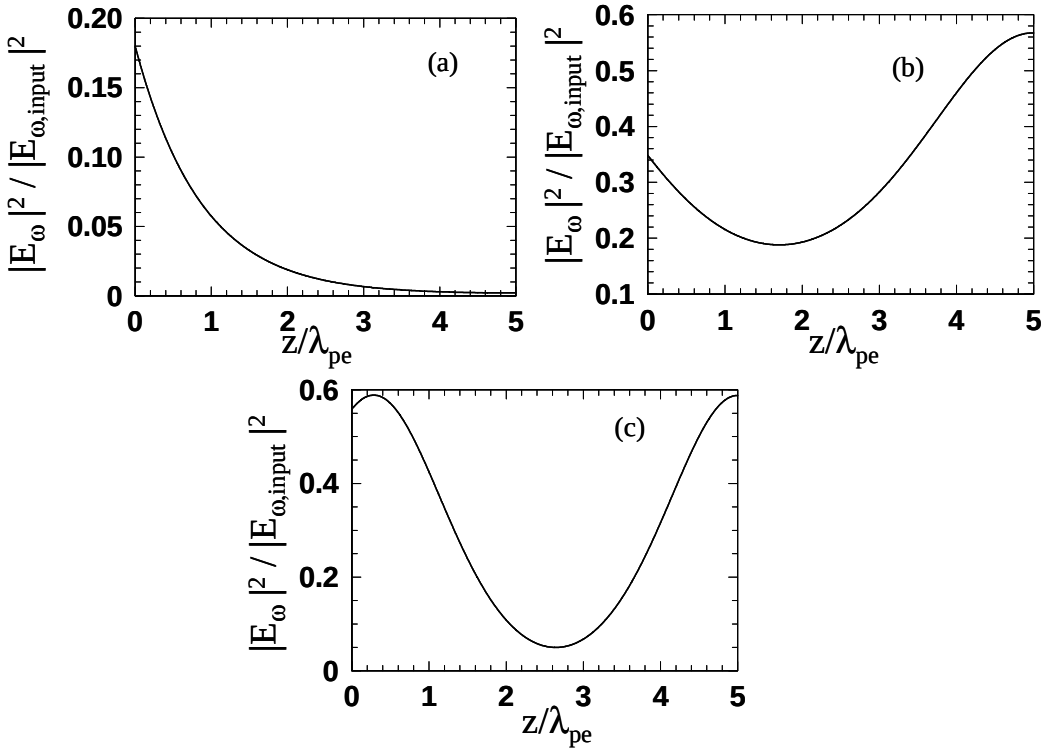

Fig. II-5. 5: Field localization in the cavity for different values of the control parameter: **(a)** σ=0 , **(b)** σ=1.6, **(c)** σ=2.7.

as shown in Fig. (II-5.5c). The excitation of dark solitons is somewhat surprising because, as discussed in the introduction, their appearance in the gap has to our knowledge never been predicted [16]. At $\omega_0=0.81\omega_{pe}$ the refractive index, the extinction coefficient, and the magnetic permeability are $n\cong-1.16*10^{-3}$; $\beta\cong1.13*10^{-1}$; $\mu\cong2.45*10^{-2}+i5.41*10^{-4}$, respectively.

Conclusions

Our calculations suggest that when $\omega_{pm}/\omega_{pe}<1$ and $\chi^{(3)}>0$, bright solitons are excited near the high frequency band edge, where n>0, and that dark solitons are excited near the low frequency band edge where n<0. On the contrary, in the case $\omega_{pm}/\omega_{pe}>1$ and $\chi^{(3)}<0$, bright solitons are excited near the low frequency band edge and dark solitons are excited near the high frequency band edge.

In conclusion, using a numerical approach we have predicted the existence of a new class of bright and dark gap solitons that are supported by NIMs. Our results suggest that NIMs could find further applications in all-optical switching devices and all-optical buffering, for example.

References and Notes

[1] W. Chen and D.L. Mills, *Phys. Rev. Lett.* **58,** 160 (1987).

[2] C.M. de Sterke and J.E. Sipe, in *Progress in Optics XXXIII,* edited by E. Wolf (Elsevier, Amsterdam,1994), Chap.3; D.N. Christodoulides and R.I. Joseph., *Phys. Rev. Lett.* **62,** 1746 (1989); D.L. Mills and S.E. Trulinger, *Phys. Rev. B*, **36,** 947 (1987); J.E. Sipe and H. Winful, *Opt. Lett.* **13,** 132 (1998).

[3] B.J. Eggleton, et al., *Phys. Rev. Lett.* **76,** 1627 (1996).

[4] C. Conti, S Trillo, G. Assanto, *Opt. Lett.* **22,** 445 (1997); T. Peschel et al. *Phys. Rev. E* **55,** 4730 (1997) ; C. Conti, S Trillo, G. Assanto, *Opt. Expr.***3,** 389 (1998).

[5] S. John and N. Akozbek, *Phys. Rev. Lett.* **71,** 1168 (1993); S.F. Mingalev and Y.S. Kivshar, *Phys. Rev. Lett.* **86,** 5474 (2001); Ping Xie and Zhao-Qing Zhang *Phys. Rev. Lett.* **91**, 213904 (2003).

[6] V.G. Veselago, *Sov. Phys. USPEKHI* **10**, 509 (1968).

[7] J.B. Pendry, *Phys. Rev. Lett*. **85,** 3966 (2000).

[8] R.A. Shelby, D.R. Smith, and S. Schultz, *Science 292*, 77 (2001).

[9] S. O'Brien, et al., *Phys. Rev. B* 69, 241101 (R) (2004).

[10] A.D. Kim, W.L. Kath, and C. G. Goedde, *Opt. Lett.* 21, 465 (1996).

[11] M. Scalora, S. Singh, and C.M. Bowden, *Phys. Rev. Lett.* 70, 1248 (1993).

[12] A.V. Yulin and D. Skryabin, *Phys. Rev. A* 67, 023611 (2003).

[13] R.W. Ziolkowski and E. Heyman, Phys. Rev E 64, 056625 (2001).

[14] W.H. Press, B.P. Flannery, S.A. Teukolsky, and W.T. Vetterling, *Numerical Recipes in C,* (Cambridge Univ. Press, Cambridge,1988)

[15] B. Acklin et al., *Appl. Phys. Lett.**63,*** 2177 (1993).

[16] Here we refer to a "true" in-gap dark soliton, i.e., a dark gap soliton excited by a single pump with no external feedback mechanism to re-inject the output field back into the structure. This external feedback scheme indeed can lead to delocalized modes excited by two counter-propagating pumps. In this regard, it is well known that in the linear regime a multilayer structure pumped on both sides can give rise to unusual delocalized states by simply choosing a proper phase link between the incident pumps [see: Centini et al. *Phys. Rev. E* , **67,** 036617 (2003)]. Therefore, in the nonlinear regime dark in-gap solitons or delocalized modes can be excited using either external feedback or two

counter-propagating pumps that may cause destructive interference and a local minimum inside the structure. A very good example of external feedback that can give rise to delocalized states in the gap of a multilayer structure is discussed in the following paper: Alatas et al, *Journ. of Nonlin. Opt. Phys. & Materials*, **13**, 259 (2004).

Conclusions

We have discussed linear and nonlinear properties of 1-D photonic crystals (part 1) and of negative index materials (part 2), underlining similarities and differences between them.

In Chapter I-2 we have presented a unified treatment of density of modes and tunneling times in finite, one-dimensional photonic crystals. We have exploited connections and differences between the various approaches used to calculate the density of modes, which include the Green function, the Wigner phase time, and the electromagnetic energy density, and we have concluded that the Green function is always the correct path to the true density of modes. We have also found that for an arbitrary structure the density of modes can always be found as the ratio between the power emitted by a source located inside the structure and the power emitted by the same source in free space, regardless of absorption or dispersion. In Chapter I-3 we have developed a three dimensional model in order to study the properties of THz emission from a one dimensional, $\chi^{(2)}$-doped photonic crystal. We have exploited difference frequency generation in a collinear configuration and we have found an enhancement factor of up to 20 with respect to difference frequency conversion from an equivalent bulk structure. In Chapter I-4 we have studied third order nonlinear processes in photonic band gap structures. We showed how two pumps can interact through a $\chi^{(3)}$ nonlinearity, i.e. cross phase modulation coupling. The transmission properties of an electromagnetic field can be strongly modified by the interaction with another electromagnetic field. The mutual interaction of two pumps can be applied in order to obtain a variety of all optical devices. In particular, with this configuration it is possible to obtain an optical transistor, a double switch and dynamical switch.

In Chapter II-2 we have studied the linear properties of a *single* slab of negative index material of finite thickness at normal and angular incidence. We have shown that the slab is characterized by a band gap in the transmission spectrum with superluminal group velocities and small group velocities at the band edges. The transmission spectrum is remarkably similar to the transmission spectrum of 1-D photonic crystals. The spectral width of the gap is proportional to the difference between the electric and magnetic plasma frequencies. The spectral position and the spectral width of the gap are independent on the length of the slab. With increasing angles of incidence, the reflecting band does not shift in frequency but it actually becomes wider. This behavior makes a single layer of a negative index material an omnidirectional reflector, in the range

between the electric plasma frequency and the magnetic plasma frequency. The operational bandwidth can be 100% or greater by increasing the separation between the electric and magnetic plasma frequencies. Moreover, we have shown that negative index materials have two points of zero group velocity dispersion that allow undistorted pulse propagation. In Chapter II-3 we have studied a symmetric hollow waveguide made with a NIM cladding. In the opacity region of the NIM, the waveguide admits both TE and TM guided modes with relatively low losses. While further material development is still needed, recent advancements in the design of meta-materials suggest that this waveguide could operate in the infrared regime with better performances compared to more traditional hollow waveguides. In Chapter II-4 we used a Green function approach to theoretically study second harmonic generation in single and coupled cavities made of a generic quadratic, positive index material sandwiched between two or more negative index materials that act as mirrors. These structures show nonlinear conversion efficiencies that may be at least four orders of magnitudes larger than perfectly phase matched bulk materials of similar length. In Chapter II-5 we have studied third order nonlinear process in NIM. We have found that a slab of NIM support the formation of both bright and dark gap solitons.

In conclusions, in this work we have discussed several basic properties related to photonic structures and negative index materials. If anything, what this work really shows is that much remains to be done in order to understand the real, underlying nature of many optical phenomena that at first sight seem simple or obvious. For this reason we wish to continue this work in our future efforts, confident that these structures have yet to reveal many more pleasant surprises.

Productivity of research during the PhD program

Peer-review publications in international journals

a) Published papers

[1] G. D'Aguanno, N. Mattiucci, M. Centini, M. Scalora, M. J. Bloemer "Electromagnetic density of modes for a finite-size three-dimensional structure", *Physical Review E* **69**, 057601 (2004)

[2] G. D'Aguanno, N. Mattiucci, M. Scalora, M. J. Bloemer, A. M. Zheltikov "Density of modes and tunneling times in finite one-dimensional photonic crystals: A comprehensive analysis", *Physical Review E* **70**, 016612 (2004)

[3] G. D'Aguanno, N. Mattiucci, M. Scalora, M.J. Bloemer "Bright and Dark Gap Solitons in a Negative Index Fabry-Perot Etalon", *Physical Review Letters* **93**, 213902 (2004)

[4] G. D'Aguanno, N. Mattiucci, M. Scalora, M.J. Bloemer "Transmission properties and field localization in a negative index Fabry-Perot etalon", *Laser Physics* **15**, 590 (2005)

[5] G. D'Aguanno, N. Mattiucci, M. Scalora, M.J. Bloemer "TE and TM guided modes in an air waveguide with negative-index-material cladding", *Physical Review E* **71**, 046603 (2005)

[6] N. Mattiucci, G. D'Aguanno, M. Scalora, M. J. Bloemer "Cross phase modulation in one-dimensional photonic crystals: Applications to all-optical devices", *Applied Physics B* **81**, 389-391 (2005)

[7] M. Scalora, G. D'Aguanno, N. Mattiucci, M. J. Bloemer, J. W. Haus, A. M. Zheltikov "Negative refraction of ultra-short electromagnetic pulses", *Applied Physics B* **81**, 393-402 (2005)

[8] M. Scalora, M.S. Syrchin, N. Akozbek, E.Y. Poliakov, G. D'Aguanno, N. Mattiucci, M.J. Bloemer, A.M. Zheltikov "Generalized Nonlinear Schrödinger Equation for Dispersive Susceptibility and Permeability: Application to Negative Index Materials", *Physical Review Letters* **95**, 013902 (2005)

[9] G. D'Aguanno,N. Akozbek, N. Mattiucci, M. Scalora, M.J. Bloemer, A. M. Zheltikov "Dispersion-Free Pulse Propagation in a Negative Index Material", *Optics Letters* **30**, 1998 (2005)

b) Papers accepted for publication

[1] N. Mattiucci, G. D'Aguanno, M. Scalora, M. J. Bloemer, N. Akozbek, J.W. Haus "Collinear THz Generation in Photonic Crystal Structures via Difference Frequency Generation" accepted for publication in the *Journal of The Optical Society of America B*

[2] M. Scalora, G. D'Aguanno, N. Mattiucci, N. Akozbek, M.J. Bloemer, M. Centini, C. Sibilia, M. Bertolotti "Pulse Propagation, Dispersion, and Energy in Magnetic Materials", accepted for publication in *Physical Review E*

c) Papers submitted for publication

[1] M.J. Bloemer, G. D'Aguanno, N. Mattiucci, M. Scalora "Broadband omnidirectional reflection from negative index materials", submitted for publication in *Applied Physics letters*

[2] N. Mattiucci, G. D'Aguanno, M. J. Bloemer, M. Scalora "Second harmonic generation from positive/negative index material hetero-structure", submitted for publication in *Physical Review E*

[3] G. D'Aguanno, N. Mattiucci, M. Scalora, M.J. Bloemer "Dramatic Enhancement of Interface Second Harmonic Generation at the zero-n Gap of a Bragg Grating", submitted for publication in *Physical Review Letters*

Conference Presentations

[1] G. D'Aguanno, N. Mattiucci, M. Scalora, M. J. Bloemer, A. M. Zheltikov "Electromagnetic Density of Modes for a Finite-Size Structure" CLEO/IQEC 2004, San Francisco-California, Poster session IThG32

[2] N. Mattiucci, G. D'Aguanno, M. Scalora, M. J. Bloemer, N. Akozbek, J.W. Haus "THz generation in one dimensional photonic crystal structures CLEO/IQEC 2004, San Francisco-California, Poster session IThG10

[3] G. D'Aguanno, N. Mattiucci, M. Centini, M. Scalora, M. J. Bloemer "Transmission properties, group velocity, and density of modes in a negative index Fabry-Perot etalon". LPHYS'04, Trieste-Italia, oral presentation, p.243 book of abstract

[4] N. Mattiucci, G. D'Aguanno, M. Scalora, M. J. Bloemer, N. Akozbek, J.W. Haus "3-D model for THz generation in one dimensional photonic crystal structures" LPHYS'04, Trieste-Italia, Oral presentation, p.244 book of abstract

[5] G. D'Aguanno, N. Mattiucci, M. Scalora, M.J. Bloemer "TE and TM Guided Modes in an Air-Waveguide with Negative Index Material Cladding", CLEO/QELS 2005, Baltimore-Maryland, Poster session

[6] G. D'Aguanno, N. Mattiucci, M. Scalora, M.J. Bloemer "Excitation of bright and dark gap solitons in a negative index material", CLEO/Europe-EQEC 2005, Monaco-Germany, Oral presentation

[7] G. D'Aguanno, N. Mattiucci, M. Scalora, M.J. Bloemer "TE and TM Guided Modes in Air through a Negative Index Material Waveguide." CLEO/Europe-EQEC 2005, Monaco-Germany, Oral presentation

[8] G. D'Aguanno, N. Mattiucci, N. Akozbek, M. Scalora, M.J. Bloemer, A. M. Zheltikov "Dispersion-free propagation of ultrashort pulses in a negative index material" CLEO/Europe-EQEC 2005, Monaco-Germany, Oral presentation

Thanks to all of you!

Many people have contributed to this work, directly and indirectly, with their suggestions, advice, encouragement, and support. My appreciation and thanks go to the following people:
my close collaborators and friends: Dr. Neshet Akozbek, Dr. Mark Bloemer, Dr. Michael Scalora; my collaborator and husband Dr. Giuseppe D'Aguanno; Professors Joseph Haus and Aleksei Zheltikov.

Many thanks to all the other members of the quantum optics group at Redstone Arsenal: Dr. Jonathan Blakely, Dr. Ned Corron, Dr. Michael Crenshaw, Dr. Scott Hayes, Mr. Krishna Myneni, Dr. Shawn Pethel.

My heartfelt gratitude goes to the whole Italian community in Huntsville, especially to the Scaloras: Fiorenza, Michele and the little Alessandro and Federica.

Finally, I would like to express my gratitude to Professor Massimo Santarsiero for his patience and support.